

Copyright
by
Mohammad Eghtedari
2008

The Dissertation Committee for Mohammad Eghtedari Certifies that this is the approved version of the following dissertation:

**ENGINEERING FUNCTIONALIZED GOLD NANOPARTICLES AS
A MOLECULAR-SPECIFIC CONTRAST AGENT TO ENHANCE
OPTOACOUSTIC DETECTION OF BREAST CANCER CELLS**

Committee:

Massoud Motamedi, Ph.D.

Malcolm Brodwick, Ph.D.

Gracie Vargas, Ph.D.

Vicente Resto, M.D., Ph.D.

Nicholas A. Kotov , Ph.D.

Dean, Graduate School

**ENGINEERING FUNCTIONALIZED GOLD NANOPARTICLES AS
A MOLECULAR-SPECIFIC CONTRAST AGENT TO ENHANCE
OPTOACOUSTIC DETECTION OF BREAST CANCER CELLS**

by

Mohammad Eghtedari, M.D.

Dissertation

Presented to the Faculty of the Graduate School of

The University of Texas Medical Branch

in Partial Fulfillment

of the Requirements

for the Degree of

Doctor of Philosophy

The University of Texas Medical Branch

December 2008

Dedication

To my mother and father, my lovely wife, and my two adorable children.

Acknowledgements

This dissertation is prepared based on my six years of exciting research experience at the Center for Biomedical Engineering under the mentorship of Professor Massoud Motamedi. He supported me along these years in my research project as well as in my personal life. It has been a dream for me since I was a high school student to become a scientist and Professor Motamedi turned my dream to reality. He is my hero and because of what he has done for me over these years, I will be indebted to him for the rest of my life.

Above all, I would like to thank my mother, Tayebah, and my father, Ali, who dedicated their lives to providing their children with an extraordinary environment in which to grow and get educated. My mother made many sacrifices to send me to medical and graduate school and encouraged me with all means to become a hardworking and educated person. My father, from whom I learned to use tools while watching him fix his car when I was a small boy, was, perhaps, the main reason why I became interested in engineering. In addition, my father has always been the symbol of trust and honesty in my mind.

Next, I would like to thank my beautiful wife who married me when I had nothing to offer her but love and hope. She is now the dedicated mother of my two adorable children, Hannah & Ryan. And together with her parents, Shahnaz & Hafez, they have

kindly supported our family over these years, in action and spirit, and allowed me the opportunity to focus on my research career. Thank you all.

Many thanks go to Dr. Alexander Oraevsky, who is currently at Fairway Medical Technologies. I have been working with him closely both at UTMB and when he moved to his company in Houston. We have performed all of the optoacoustic experiments that are presented in this dissertation together. This dissertation could not have been initiated nor finalized without his sincere collaboration.

John Al Copland, who is currently a faculty member at Mayo Clinic, was a key person in my project. He was a faculty member at UTMB and I met him first when I joined his laboratory for a research rotation. During that rotation, I learned essential laboratory techniques on cell culturing, animal models, various staining methods including silver staining, and many others. Dr. Copland is the main person to whom I turn to discuss the biology of cancers and tumor biomarkers. He kindly collaborated with our team at UTMB even when he moved to Mayo Clinic. Also, his extraordinary support was a key factor for my acceptance at my radiology residency program and so I gratefully thank him.

Brent Bell, our lab manager had a significant contribution to this project. He has always been available for me to learn how to use lasers, setup experiments, or to solve any technical problems that I encountered during my several years at this lab. He has always quickly responded to my requests and shared his technical experience with me without any hesitation.

Dr. Gracie Vargas, who is also a member of my committee, kindly dedicated tremendous amounts of time and effort on editing my dissertation to enrich it both from a scientific aspect as well as to improve its readability. Her suggestions and guidance from the initial steps when I proposed the title of my dissertation up to the present time that I

am preparing the final version of my dissertation have been a great help to me. I also had the opportunity to work with her on another project that involved using confocal and two-photon microscopy to study cell-cell and cell-scaffold interactions. In that project, I learned a great deal from her on the subject of optics, fluorescence imaging, and image processing.

Dr. Nicholas A Kotov, another member of my committee, is the main person from whom I learned the basics of working with nanoparticles. I had also the blessing to work with him on my other project studying the cell-cell and cell-scaffold interactions.

Anton Liopo, a kind colleague at the Center for Biomedical Engineering, was the key person for nanoparticles preparation and functionalization, *in vitro* experiments, as well as animal studies. Without his generous support, the project could not have been completed.

A significant portion of my knowledge in optics comes from my scientific discussions with Alexander Kholodnykh. He is a great scientist at the Center for Biomedical Engineering. It has been a pleasure for me to work with him.

I express my apologies for not being able to mention the name of all persons who contributed to this project one by one. I had a wonderful life as a graduate student and am proud of being a UTMB graduate. Thank you all.

This dissertation was supported by NIH grant # R44CA110137, NSF grant # 427590, and NASA grant # 59249.

ENGINEERING FUNCTIONALIZED GOLD NANOPARTICLES AS A MOLECULAR-SPECIFIC CONTRAST AGENT TO ENHANCE OPTOACOUSTIC DETECTION OF BREAST CANCER CELLS

Publication No. _____

Mohammad Eghtedari, Ph.D.

The University of Texas Medical Branch, 2008

Supervisor: Massoud Motamedi, Ph.D.

Molecular targeting of malignant tumors is a promising field of research that could potentially revolutionize the diagnosis and treatment of many types of cancer including breast. Delivering molecular specific contrast agents to breast cancer cells would enhance the sensitivity and specificity of imaging methods to detect cancer foci at earlier stages, when complete cure is possible. Optoacoustic tomography (OAT) is a non-invasive imaging modality that can be used to produce an image of the distribution of light absorbing components deep within a turbid medium such as human breast. OAT could potentially be used to image breast tumors based on their enhanced angiogenesis; however, its sensitivity and specificity would be limited due to the lack of abnormal angiogenesis at the early stages of tumor growth.

Gold nanoparticles generate strong acoustic signal upon pulse laser irradiation and thus are detectable at low concentrations using optoacoustic technique. The goal of this

dissertation is to engineer functionalized gold nanoparticles and employ them as a contrast agent for optoacoustic detection of cancer cells.

To achieve this goal: 1) gold nanoparticles were fabricated in different shape and sizes and their physicochemical properties were optimized for both tumor targeting and optoacoustic detection; 2) the biological properties of fabricated gold nanoparticles were evaluated *in vitro* and *in vivo* by determining their stability, toxicity, biodistribution, and molecular targeting properties; 3) the performance of gold nanoparticles to target cancer cells and function as a contrast agent for OAT were assessed *in vitro* using breast phantoms and then *in vivo* using animal models.

Table of Contents

List of Figures	xiii
Chapter 1: Introduction	1
1.1 Breast cancer facts and figures	1
1.2 Histological types of breast cancer	2
1.3 Early detection will reduce the mortality and morbidity of breast cancer	3
1.4 Medical imaging and breast cancer.....	4
1.5 Molecular targeting of breast cancer.....	8
1.6 The role of nanotechnology in cancer imaging.....	13
Chapter 2: Introducing Optoacoustic Tomography	16
2.1 Background.....	16
2.2 How does OAT work?	16
2.3 OAT for biological imaging.....	22
2.4 OAT for breast imaging	25
2.5 Angiogenesis as an endogenous contrast agent for OAT	27
2.6 The need for an exogenous contrast agent to enhance the sensitivity and specificity of OAT	30
Chapter 3: The Application of Nanotechnology for Molecular-Specific Targeting of Breast Cancer	33
3.1 Introducing gold nanoparticles	33
3.2 Optical properties of spherical gold nanoparticles.....	33
3.3 Fabricating functionalized spherical gold nanoparticles for <i>in vitro</i> experiments	36
3.4 Determining the optoacoustic profile of spherical gold nanoparticles ...	43
3.5 Optoacoustic imaging of spherical gold nanoparticles within phantom gel	45
Chapter 4: Employing non-spherical gold nanoparticles for OAT.....	48
4.1 Non-spherical gold nanoparticles are superior to spherical gold nanoparticles for <i>in vivo</i> experiments	48
4.2 Gold nanorods as contrast agents for OAT	49

4.3 Crystal structure of GNRs and the role of Hexadecyltrimethylammonium Bromide on bioconjugation.....	58
4.4 Rationale to functionalize gold nanorods	60
4.5 Fabricating Functionalized GNRs.....	69
4.6 Why is a covalent conjugation of antibody to gold nanorods required for <i>in vivo</i> experiments?.....	72
4.7 Determining the profile of optoacoustic signal generated by GNRs upon near-infrared laser irradiation	76
4.8 Near-infrared OAT of targeted cancer cells <i>in vitro</i>	78
4.9 Near-infrared optoacoustic detection of subcutaneously injected GNRs	79
4.10 Summary	87
Chapter 5: Determine the Biocompatibility, Stability, Biodistribution, and Selective Tumor Targeting of Fabricated Gold Nanoparticles.....	88
5.1 Functionalizing gold nanoparticles to enhance their biocompatibility ...	88
5.2 Selective targeting of functionalized GNRs to cancer cells <i>in vitro</i>	90
5.3 Determining the stability of functionalized GNRs within the blood microenvironment	93
5.4 Determine the functionality of GNRs within the blood microenvironment	95
5.5 Determining the biodistribution of functionalized GNRs upon intravenous injection into mice.....	96
5.6 Laser safety in the presence of gold nanoparticles	100
5.7 Potential limitations of gold nanoparticles as a contrast agent	103
5.8 Summary	104
Chapter 6: Comparing the Results of OAT against Those of Conventional Imaging Techniques	105
6.1 Comparing OAT with other available non-invasive, non-ionizing imaging methods	105
6.2 OAT versus Diffuse Optical Tomography.....	105
6.3 OAT versus conventional ultrasonography	106
6.4 OAT versus MRI.....	107

Chapter 7: Summary and Conclusion	109
Appendix A.....	111
GNRs Protocol.....	111
Appendix B.....	113
Producing fluorescently labeled and Herceptin-conjugated GNRs using PAA113	
Bibliography	114
VITA.....	126

List of Figures

Figure 1:	The mortality of breast cancer in the US by time for different races.	2
Figure 2:	The sensitivity of currently available medical imaging methods.	8
Figure 3:	The schematics of a typical optoacoustic experiment.....	17
Figure 4:	An array of acoustic transducers may be used to locate a light-absorbing object within a scattering phantom..	21
Figure 5:	Absorption coefficient of reduced hemoglobin (Hb) and Oxyhemoglobin (HbO ₂) and water at different wavelengths.....	24
Figure 6:	Positioning of human breast during conventional mammography..	26
Figure 7:	Macroscopic cross section of breast adenocarcinoma in human..	28
Figure 8:	Immunostaining of the skin of tumor-bearing mouse using vWF as a marker of blood vessels..	29
Figure 9:	Basics of enhancing the efficiency of optoacoustic imaging using a contrast agent.	31
Figure 10:	The absorption pattern of spherical gold particles with different sizes.	35
Figure 11:	Different techniques that have been utilized to conjugate spherical gold nanoparticles	39
Figure 12:	IgG molecule contains several disulfide binds in its structure.	40
Figure 13:	Schematics of bioconjugation of Herceptin to spherical gold nanoparticles using Streptavidin-biotin system.	41
Figure 14:	Mab binds specifically to HER2-positive cells.....	42
Figure 15:	Electron microphotographs of SK-BR3 cells incubated with Herceptin-conjugated gold nanoparticles.....	43
Figure 16:	The amplitude of optoacoustic signal as a function of spherical nanoparticles' concentration.	44
Figure 17:	Photograph of a disk-shaped gel phantom placed on the arc-shaped optoacoustic transducer array	46
Figure 18:	Optoacoustic image of gelatin phantom with four embedded objects made of SK-BR3 cells that were treated with conjugated NPs..	47
Figure 19:	Plasmon resonance frequency of gold nanoshells depends on the core/shell ratio.. ..	50
Figure 20:	TEM (left) and absorption spectrum (right) of gold nanocages..	51
Figure 21:	The relation between aspect ratio of gold nanorods and their peak absorption wavelength..	51
Figure 22:	Size-normalized absorption cross-section of different types of gold nanoparticles.. ..	52
Figure 23:	Absorption spectra of spherical gold nanoparticle as compared to that of cylindrical.. ..	53
Figure 24:	Absorption spectra of GNRs with an aspect ratio of 3 as was prepared in our laboratory.	53
Figure 25:	Aspect ratio of gold nanorods determine their optical light absorption.	54
Figure 26:	Absorption spectrum of raw GNRs with an approximate size of 50x15 nm.	55

Figure 27:	Gold nanorod solution as seen under two-photon excitation microscopy using a 20X objective lens.	56
Figure 28:	Two-photon excitation microscopy of chicken muscle injected with gold nanorods.	57
Figure 29:	Crystal structure of GNRs as revealed by high-resolution transmission electron microscopy.	59
Figure 30:	Crystal structure of GNRs.	59
Figure 31:	CTAB assembles into a lipid belayed around gold nanoparticles and only allows the growth of gold nanoparticles in one dimension.	60
Figure 32:	End-to-end assembly due to the attachment of biotin to the ends of GNRs.	60
Figure 33:	Absorption spectra of CTAB-coated and PEG-coated GNRs as fabricated in our lab.	65
Figure 34:	Chemical structure of polyacrylic acid (PAA, left) and polystyrenesulfonate (PSS, right).	68
Figure 35:	Bright field and fluorescent images of BT-474 (A,B) and COS-7 (C,D) cells incubated with Alexa Fluor 568-labeled Herceptin-nanorod conjugates.	71
Figure 36:	Direct conjugation of antibodies to microspheres.	73
Figure 37:	Chemical structure of NanoThinks Acid16 and CTAB.	74
Figure 38:	The schematics of Her-PEG GNRs.	75
Figure 39:	Optoacoustic signal generated by GNRs detected through a 4 cm-thick scattering media.	77
Figure 40:	Optoacoustic imaging of targeted cancer cells embedded within a gelatin phantom.	79
Figure 41:	Schematics of <i>in vivo</i> optoacoustic detection of subcutaneously (SQ) injected GNRs (GNRs).	81
Figure 42:	<i>In vivo</i> detection of subcutaneously injected GNRs in nude mouse.	82
Figure 43:	Optoacoustic signal generated following subcutaneous injection of 50 μ L of GNRs at a concentration of 12.5 pM into the abdominal area of a nude mouse. ...	83
Figure 44:	Schematics of optoacoustic detection of GNRs following subcutaneous injection into nude mice.	84
Figure 45:	Setup of the experiment for optoacoustic imaging of nude mice injected with GNRs..	84
Figure 46:	Optoacoustic image of a nude mouse before (a) and after (b) injection of GNRs.	85
Figure 47:	Schematics of OAT rotational system	86
Figure 48:	Toxicity assessment of different types of GNRs on three cell lines.	89
Figure 49:	Silver-enhanced images of four cell lines incubated with Her-PEG GNRs <i>in vitro</i> ..	91
Figure 50:	Bright field microscopic images of SK-BR3 cells that were incubated with PEG GNRs (A) or Her-PEG GNRs (B) <i>in vitro</i> ..	92
Figure 51:	Absorption spectra of mouse serum after mouse blood has been incubated with three types of GNRs for three hours <i>ex-vivo</i>	94
Figure 52:	Bright field microscopy images of silver-stained BT-474 and fibroblast cells treated with Her-PEG GNRs.	96

Figure 53: Silver staining (top row) and H&E staining (bottom row) of mouse tissue slices following intravenous injection of GNRs..... 98

Figure 54: Bright field microscopic images of silver-enhanced staining of mouse tissue following intravenous injection of HER-PEG GNRs..... 99

Figure 55: Level of released LDH by damaged BT-474 cells upon laser irradiation. 101

Figure 56: H&E staining of mouse skin eight hours post laser irradiation in the presence of GNRs.. 103

Chapter 1: Introduction

In this chapter, different types of breast cancer will be presented and their impact on human will be discussed. The role of early detection in reducing the mortality of breast cancer is explained. After a brief description of currently available imaging techniques for the detection breast cancer, the limitations of each technique will be introduced. Finally, the role of nanotechnology as a toll to overcome current limitations on breast imaging will be presented.

1.1 BREAST CANCER FACTS AND FIGURES

The National Cancer Institute (NCI) predicted 184450 new cases and 40930 deaths due to breast cancer in the United States during 2008 (1). Figure 1 depicts the mortality of breast cancer in the US in recent years grouped by races. Breast cancer is the most common type of cancer after skin malignancies among women in this country. Based on the reported rate of breast cancer in 2003–2005, 12% of girls born today will be diagnosed with breast cancer in their lifetime. The female to male ratio for breast cancer is 12:1 (2). Tremendous amounts of time and effort are dedicated to research toward better understanding, earlier detection, or more efficient treatment of this disease.

Studies have shown that the evolution of breast tumor is a non-deterministic process that is affected by both genetic background and environment. It is believed that the development of a breast tumor involves the accumulation of several genetic alterations via a process called carcinogenesis. From a histological point of view, different stages of carcinogenesis can be identified by transformation of breast tissue from normal state toward hyperplasia, dysplasia, carcinoma in situ, and finally invasive carcinoma. It is difficult to precisely predict the timeline when precancerous lesions turn into invasive carcinoma.

1.2 HISTOLOGICAL TYPES OF BREAST CANCER

The human breast is mainly composed of fatty tissue that accommodates glands and ducts. Glands produce milk during lactation, while ducts collect and drain milk from lobules to the nipple. Almost all types of cells in human breast may undergo neoplastic transformation to produce cancer. In other words, breast cancer does not represent a single type of tumor but is instead a general term that includes a variety of tumors with different origins and outcomes. For instance, breast tumor may originate from the fat in the breast (liposarcoma), from glands (adenocarcinoma), or from ducts (ex. ductal carcinoma).

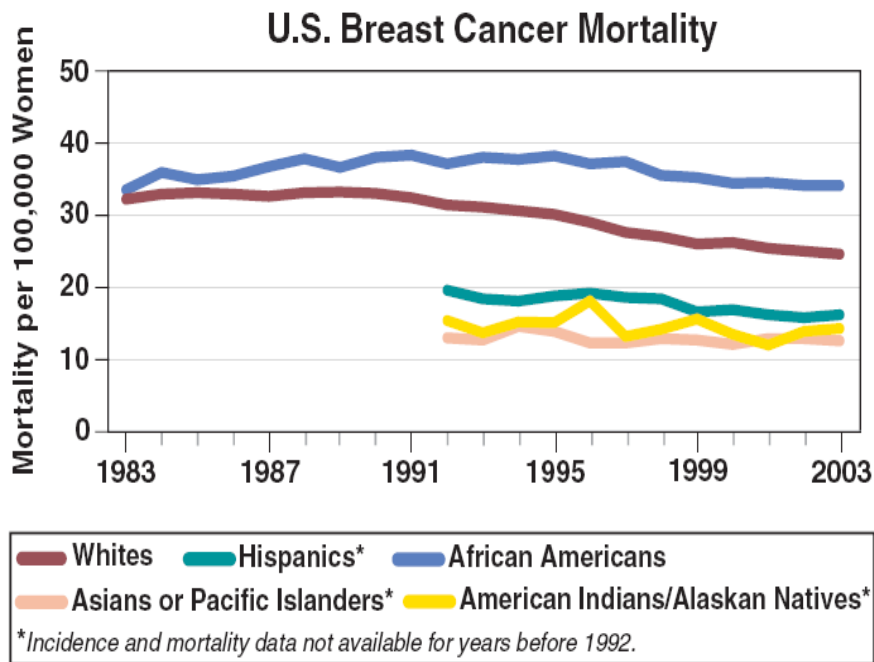


Figure 1: The mortality of breast cancer in the US by time for different races. (National Cancer Institute, www.cancer.gov)

Counting for more than 70% of breast cancers, the most common type of breast cancer is invasive ductal carcinoma; this particular cancer originates from breast ducts. Another term that is commonly used in the literature is ductal carcinoma in situ (DCIS). DCIS describes when the lesion is confined to the lactiferous ducts and the basement membrane of duct remains intact. Although DCIS *per se* is not lethal, early detection of DCIS is important because within 10 years, up to 50% of patients with DCIS will develop invasive ductal carcinoma.

The second most common histological type of breast cancer is invasive lobular carcinoma. The term lobular carcinoma in situ (LCIS) applies to a lesion that is confined to the lobule where the basement membrane of the lobule is intact. Unlike ductal carcinomas, invasive lobular carcinomas tend to grow diffusely rather than producing a mass. Due to their diffuse growth pattern, lobular carcinomas are more difficult to detect. Invasive lobular carcinoma may even extend to the contralateral breast. Mucinous, tubular, medullary, papillary, and other types of breast cancer are rare.

1.3 EARLY DETECTION WILL REDUCE THE MORTALITY AND MORBIDITY OF BREAST CANCER

Meta-analysis studies have confirmed the benefit of early detection of breast cancer in reducing mortality and morbidity of breast cancer (3). Early stage is usually defined at a stage that the tumor has not spread out of its original location and also the average diameter of the tumor is less than 2 mm³ (4). It is after this stage that abnormal angiogenesis appears within a tumor. Over the years, mammogram, ultrasound, and ultrasound-guided biopsies have served physicians to replace invasive procedures such as radical mastectomy and axillary's lymph node dissection with less invasive, better tolerated procedures such as breast conservation surgeries and sentinel node biopsies.

Currently, annual clinical breast exam and mammography is recommended for women aged 40–70 years old. The management of patients with a suspicious lesion includes confirming the diagnosis, identifying the stage of disease, and choosing an appropriate treatment for each individual patient. Also, it is necessary to follow patients that need a therapeutic procedure to assess their response to treatment. Identifying the stage of disease in any given patient is a crucial step because it will determine the type of treatment that is appropriate for that particular person. The TNM staging system is used for the staging of breast cancer, in which T determines the size of the tumor, N determines the involvement of lymph nodes, and M declares the presence of distant metastasis. Details of the TNM system are beyond the scope of this dissertation, but it is noteworthy to mention that determining the exact size and extent of a lesion is essential for appropriate treatment planning.

1.4 MEDICAL IMAGING AND BREAST CANCER

Medical imaging is an indispensable part of breast cancer management. Mammography is currently the first-line diagnostic option that is widely used for the detection of breast lesions. Several lines of evidence support the benefit of annual mammography for the screening of breast cancer for women over age 40. When describing a medical imaging modality, sensitivity is defined as the percentage of people in whom the lesion can be seen using that imaging modality among the people who actually have that lesion. The sensitivity mammography decreases dramatically in younger patients due to their dense breast tissue; this is the main reason why mammography is not routinely recommended for women under age 40.

Mammography has been proven to significantly lower the mortality and morbidity of breast cancer. In a randomized study in Sweden, long-term results demonstrated that

screening mammography decreased the mortality due to breast cancer by 21% (3). However, like many other diagnostic modalities, mammography is not without limitations. For instance, the false negative rate of mammography is found to be up to 30%. Surprisingly, up to 10% of breast tumors, even at the time that they are palpable in physical exam, cannot be detected via mammography due to the lack of x-ray contrast. False negative results are more common in younger women with dense breasts. False positive results are even more common: only 45% of lesions that are reported as malignant in mammography are indeed malignant as confirmed by biopsy. As a result, some patients with breast cancer are missed and some others without a malignant tumor undergo unnecessary biopsies due to incorrect mammography findings. Because of these limitations, other imaging modalities such as ultrasound (US), magnetic resonance imaging (MRI), position emission tomography (PET), single photon emission computed tomography (SPECT), lymphoscintigraphy, and scintimamography, are used in the clinic or are under development in research facilities to provide physicians with more accurate information regarding the status of a suspicious breast lesion. Recent concerns on the toxicity of commonly used contrast agents such as gadolinium for MRI (5;6) and iodine compounds for computed tomography (CT) scans (7) justify the need for safer imaging techniques and less toxic contrast agents.

Ultrasound-guided biopsy is a very powerful technique that has almost replaced open surgical biopsies. Ultrasound, and not mammography, is the first diagnostic option for the evaluation of a suspicious breast lesion in women under age 30, mainly because the breast tissue is very dense at that age and thus mammography would not be reliable. Ultrasound is also recommended for pregnant or lactating women when ionizing radiation may not be recommended. It has been found that ultrasound, when combined with mammography, can prevent up to 22% of unnecessary biopsies (8). False negative

results of ultrasound-guided biopsies are reported to be as low as 0.4% and thus are negligible (9;10).

Although ultrasonography can reliably differentiate a cystic lesion from a solid lesion, ultrasound per se does not provide a high specificity to distinguish benign from malignant lesions. Specificity of an imaging method is defined as the percentage of people that actually have a lesion among those in whom a lesion can be seen using that imaging method. Ideally, one would look for test with 100% specificity and 100% sensitivity; however, such imaging methods do not exist. Recently, contrast-enhanced ultrasonography has been reported as a potential solution to reveal abnormal angiogenesis within a tumor to overcome the current limitations of ultrasound for breast tumor imaging (11-13); however, the large size of gas-filled microbubbles that are used as ultrasound contrast agents significantly limits the extravasation of these agents out of blood vessels toward interstitial space. Because the fenestrations of blood vessels are found to be less than a micrometer (14) and the fact that ultrasound contrast agents are usually a few micrometer in diameter (15) ultrasound contrast agents remain intravascular. Thus, ultrasound contrast agents cannot be used for molecular targeting of breast cancer cells because breast cancer cells are mainly located within extravascular space.

MRI is usually used when a suspicious lesion cannot be evaluated by mammography or ultrasound. In addition, MRI is very useful when recurrence or a residual tumor is suspected following a surgical procedure. However, the cost and limited specificity of MRI to detect breast cancer, which is reported in different studies to be from 37% to 97%, are the main reasons why MRI cannot be used widely in detecting breast cancers. As a result, the use of MRI is limited to situations where a known cancer is present or is highly suspected (16).

Diffuse optical tomography (DOT) is one of the most important non-invasive and non-ionizing imaging modalities available for breast. DOT can be used to measure optical properties such as light absorption and light scattering within tissue (17;18). Modern DOT devices use fiber optics to deliver near-infrared light to tissue and sensitive detectors to collect scattered and transmitted photons. Reconstruction software then generates an image of the distribution of components such as hemoglobin, water, and lipid within tissue. Because it has been shown that the composition of these components are altered within malignant lesions of breast as compared to that of normal tissue, DOT can be used to locate lesions within breast. DOT may work in transmitted or remission mode; the former needs access to tissue from both sides while the latter only needs to access tissue from one side. Despite promising results, there are several factors that limit the wide application of DOT for the imaging of breast tissue in clinic. First, the maximum depth of imaging in breast-like phantoms is less than 15 mm. This is mainly due to the strong scattering of light within tissue. Scattering will attenuate light as it propagates through tissue and thus will limit the maximum depth of imaging using optical methods. Secondly, the spatial resolution of DOT is several millimeters; this is not as good as that of mammography, ultrasound, or MRI. Because of its limitation in depth of imaging and poor spatial resolution, DOT is not a widely-accepted imaging modality for breast tissue.

Figure 2 lists the sensitivity of medical imaging methods such as US, CT, MRI, SPECT, PET, and diffuse optical tomography that are currently available in clinics (19). Other imaging methods such as acousto-optics are under investigation (20). However, one should note that none of the aforementioned imaging modalities provide high specificity for cancer detection unless a molecular specific contrast agent is used. Unfortunately, molecular specific contrast agents are under investigation and thus are not

yet available in clinic. In the next section, the role of molecular targets for breast cancer imaging will be discussed.

Sensitivity and Resolution of Cancer Imaging Modalities as a Function of Cell Number and Contrast Agent/Radiotracer Concentration							
Modality	Typical Voxel/Pixel Dimensions (Resolution)	Maximum No. of Cells per Voxel/Pixel	Clinically Available Exogenous Contrast Agent(s)	Radiotracer/ Contrast Agent Hydrodynamic Diameter*	Contrast Agent Concentration per Voxel/Pixel Required for Detection†	No. of Molecules of Contrast per Voxel/Pixel Required for Detection†	Notes
US	1 μ L (1 \times 1 \times 1 mm)	10 ⁶	Microbubbles	1 μ m	NA	NA	Microbubbles remain intravascular in most tissues
CT	1 μ L (1 \times 1 \times 1 mm)	10 ⁶	Iodine	\approx 1 nm	0.5 M	3 \times 10 ¹⁷	Requirement for molar concentrations precludes targeted imaging
MRI	1 μ L (1 \times 1 \times 1 mm)	10 ⁶	Chelated Gd ³⁺	\approx 1 nm	50 μ mol/L	3 \times 10 ¹³	Would require > 10 ⁷ Gd ³⁺ atoms per cell for detectability
SPECT	1.7 cm ³ (12 \times 12 \times 12 mm)	1.7 \times 10 ⁹	^{99m} Tc ¹¹¹ In ⁶⁷ Ga	\approx 1 nm	0.3 pM†‡ (\approx 8 \times 10 ³ Bq/voxel)	3 \times 10 ⁸	On average approximately 0.2 radioatoms per cell†‡
PET	0.5 cm ³ (8 \times 8 \times 8 mm)	5 \times 10 ⁸	¹⁸ F	\approx 1 nm	0.02 pM†‡ (\approx 7 \times 10 ² Bq/voxel)	6 \times 10 ⁶	On average approximately 0.01 radioatoms per cell†‡
Optical (2-D)	0.01 mm ² (0.1 \times 0.1 mm)	10 ³	ICG	\approx 1 nm	\approx 10-100 nmol/L	6 \times 10 ⁷ §	Surface only NIR fluorescence, requires approximately 10 ⁴ –10 ⁵ fluorophores per cell for detectability
Optical (3-D)	1 cm ³ (1 \times 1 \times 1 cm)	10 ⁹	ICG	\approx 1 nm	\approx 10-100 nmol/L	6 \times 10 ¹³	NIR tomography-based, requires approximately 10 ⁴ –10 ⁵ fluorophores per cell for detectability

Abbreviations: US, ultrasound; NA, not applicable; CT, computed tomography; MRI, magnetic resonance imaging; Gd³⁺, gadolinium; SPECT, single photon emission computed tomography; ^{99m}Tc, technetium 99m; ¹¹¹In, indium 111; ⁶⁷Ga, gallium 67; PET, positron emission tomography; ICG, indocyanine green; NIR, near-infrared.
*After conjugation of a targeting molecule to a contrast agent or radiotracer, final hydrodynamic diameter increases proportionally.
†Does not take into account the significant effect of background and tissue attenuation on detectability. Values shown are theoretical only.
‡Assumes 100 counts, 5 minutes scan, SPECT/PET attenuation of 0.2/0.1, sensitivity of 0.02%/0.5%, half-life of 6/1.8 hours, and maximum specific activity.
§Assuming a tumor thickness of 0.1 mm (10 cells thick).
||Approximate resolution at a depth of 10 cm in soft tissue such as breast.

Figure 2: The sensitivity of currently available medical imaging methods. Table is taken from reference (19)

1.5 MOLECULAR TARGETING OF BREAST CANCER

The subject of molecular targeting of breast cancer includes mechanisms by which one can distinguish cancer cells from normal cells based on their differential molecular expressions. This difference may occur at the gene level, the level of mRNA, or at the level of final products of genes that are proteins. In practice, most *in vivo*

molecular recognition techniques depend on the changes of a specific protein on the surface of cancer cells. Alternately, changes in the interstitial components or on the endothelium of blood vessels within a tumor, which are all induced by cancer cells through secreting angiogenic factors, can be used to identify a tumor. Examples of these alternate targets include VEGF (21), RGD (22), lymphatic homing peptides (23), and GRP-R (24). It goes without saying that for *in vivo* studies, the cell membrane functions as a barrier that hides intracellular components of a cell such as DNA or mRNA; in contrast, proteins that are expressed on the surface of cells are more accessible for molecular recognition.

The goal of tumor targeting is to identify cancer cells based on their molecular expressions and deliver a diagnostic or therapeutic agent such as drugs or radioactive materials specifically to cancer cells without affecting normal tissue. Systemic toxicity that is observed during conventional chemotherapy or radiotherapy usually limits the maximum allowed dose of therapy and thus may limit the overall efficiency of a treatment regime. However, tumor targeting can be used to deliver a higher concentration of drugs to cancer cells with less systemic toxicity. This may potentially allow physicians to use a higher concentration of drugs to better destroy cancer cells. Most tumor targeting applications are based on the differential expression of surface proteins. Thus, the first step in tumor targeting would be to identify those molecular changes that occur on the surface of cancer cells. To identify these changes, we need to know more about the pathology of cancer. Despite promising data on tumor targeting, the field has been limited by the vehicle that can be used to deliver diagnostic/therapeutic agents to cancer cells. In the following chapter, it will be explained how nanotechnology can be used as a tool to overcome some of these limitations.

Several lines of evidence suggest that the transformation of normal breast tissue to cancer is a result of multiple genetic alterations that finally disable the controlling mechanisms of cell proliferation by altering the expression of certain signaling proteins. These genetic alterations may lead to under-expression of a series of proteins that normally prevent cellular proliferation or to over-expression of those that stimulate cell division. As mentioned previously, genetic alterations may be detected in DNA level, mRNA, or by direct measurement of the concentration of a protein that controls the rate of proliferation/division inside cells. In some cancers, the genetic alteration leads to the presence of a new protein or over-expression of an existing protein on the surface of cells. Characterizing the expression pattern of surface proteins or markers in different types of cancer is a fast-growing field of research; several markers have been already identified for non small cell lung cancer (NSCLC) and for breast, ovarian, gastric, colorectal, head and neck, and prostate cancer.

As for breast cancer, the list of tumor markers that are in clinical trials or have been approved include CD152, EpCam, and Her2/neu (25). Among these markers, Her2/neu is the most successful example of a tumor marker on which tumor targeting has been performed. Monoclonal antibodies are classic tools to target tumor markers such as Her2/neu on the surface of cancer cells. Currently, there are at least three FDA-approved antibodies for tumor targeting of breast cancers (26):

- Trastuzumab (Herceptin) that binds to the extracellular domain of Her2/neu receptor
- Pertuzumab that binds to a different epitope of Her2/neu receptor
- Bevacizumab that binds to vascular endothelial growth factor receptors (VEGFRs)

Alteration of the expression of epidermal growth factor receptor (EGF) on the surface of cells has been found to be linked to cancer development. Her2/neu is an example of proto-oncogenes that have been found to be overactivated in more than 25% of overall breast tumors and 75% of malignant breast tumors (27). Her2/neu gene is located on chromosome 17. Its product is a receptor with the same name that is expressed in low level on the surface of cells in breast, prostate, endometrium, ovary, and heart. Herceptin is a humanized monoclonal antibody that binds to the extracellular domain of Her2/neu receptor. Herceptin is currently in clinical use to treat metastatic breast cancers that over-express Her2/neu, and is one of the most successful examples of tumor targeting in cancer research (28). Her2/neu has been successfully used by several groups to target diagnostic and therapeutic materials to breast cancers (29). Some of the factors that make Her2/neu receptor a near ideal target for breast tumor targeting include:

- Her2/neu is a 185 kD transmembrane protein that has an extra cellular domain for which monoclonal antibodies are available in the market. This receptor is found to be overexpressed remarkably in breast and ovarian cancers (30). Low levels of this receptor are found in human normal tissues such as brain and heart (31); however, the expression level in normal tissue is much lower than that of breast or ovarian cancer. This low level of expression in normal tissue reduces the chance of interference of normal tissue with tumor targeting.
- Her2/neu is a tyrosine kinase receptor that plays an important role in stimulating cell growth rate. Targeting Her2/neu can potentially deactivate its tyrosine kinase activity and thus may result in both diagnostic and therapeutic applications.

- Commercially available breast cancer cell lines highly (AU-565, SK-BR3 and BT474); moderately (MCF7); or weakly (MDA-MB-231) express Her2/neu (32). SK-BR3 cells are reported to express up to 926000 copies of Her2/neu receptor per cell (33).
- Her2/neu is over-expressed in up to 25% of breast cancers, and in 50% of metastatic breast cancers. Its presence, which is usually reported after immunohistochemistry as 1+ , 2+, or 3+, is a poor prognostic factor (26). Retrospective studies have shown the clinical benefits of breast tumor targeting using Herceptin in patient with 3+ staining.
- Randomized studies have shown that the overexpression of Her2/neu occurs at early stages of breast cancer and is correlated with a poor response to treatment (34;35).
- Interestingly, the expression of Her2/neu is minimal in normal tissues except for trace expression in heart, prostate, endometrium, and ovary. This is important because a low expression in background tissue is needed for tumor targeting in order to avoid systemic toxicity during therapy. A low background expression is also important for obtaining a high signal to noise ratio during diagnostic applications.
- Herceptin, which is a humanized antibody that binds the extracellular domain of Her2/neu, has been FDA-approved since 1998 for the treatment of metastatic breast cancers (26).
- Her2/neu-conjugated iron oxide nanoparticles have been used as a contrast agent to image Her2/neu over-expressing breast cancer cell lines *in vitro* (32).

- Her2/neu has been successfully used in the past to deliver liposomes to breast cancer cells *in vivo* (30).

1.6 THE ROLE OF NANOTECHNOLOGY IN CANCER IMAGING

NCI has recognized nanotechnology as a tool that provides an extraordinary opportunity to improve the detection and treatment of cancers (36) mainly because it can be used to overcome current limitations of tumor targeting. According to the National Nanotechnology Initiative (NNI), nanotechnology is defined as the study of materials with a diameter ranging between 1 and 500 nm. It has been found that some materials exhibit novel physicochemical properties when they are made in this range of sizes. The goal of nanotechnology is to characterize these new properties and use them to manufacture new devices that can be used to overcome the limitations of currently available devices in scientific fields. Nanobiotechnology is a branch of nanotechnology that involves the study of the biological applications of nanotechnology. Nanobiotechnology is a rapidly growing field with applications in many subdivisions of medicine including cancer management (37).

Current clinical applications of nanotechnology in cancer mainly include targeted drug delivery, biomolecular profiling of cancer markers, and imaging. Examples of targeted drug delivery applications in cancer therapy include drug-loaded nanoparticles that are made of micelles (38), ceramic (39), gelatin (40), and liposomes (30); such nanoparticles have been successfully used many times over the past twenty years for the treatment of cancers. Examples of nanoparticles that have been used for cancer imaging include quantum dots (41); gold nanoparticles; and paramagnetic particles that were proposed for the detection of cancer cells using fluorescent, two-photon microscopy, and magnetic resonance imaging, respectively. Usually, a functionalized nanoparticle is

manufactured and injected intravenously. Nanoparticles circulate in the body and accumulate within tumor, where they act on the target cells. There are at least two known mechanisms for the accumulation of injected nanoparticles within tumors: passive accumulation and active accumulation.

Passive accumulation occurs based on the fact that the fenestrations in the endothelium of vessels within a tumor are much larger than those in normal tissue (42;42;43). For instance, the diameter of endothelial fenestrations within tumor is reported to be in the range of 200 nm to 1.2 μm (14) much larger than fenestrations of a normal endothelium. The size and surface characteristics of nanoparticles determine the extent of passive accumulation. While there is not a single ideal size for particles that accumulate within a tumor, it has been suggested that particles that are in the range of 100 nm to 200 nm have the best chance to accumulate in the tumor (44); larger particles will be trapped by spleen while the smaller nanoparticles will be trapped in the liver quickly. Modifying the surface of particles with polyethylene glycol has been found to elongate the circulation time of nanoparticles by hiding particles from the reticuloendothelial system in liver and lungs. It is suggested that polyethylene glycol helps nanoparticles to escape from the reticuloendothelial system by steric repelling of the opsonin proteins that are essential for the clearance of nanoparticles from blood stream (45;46). As a result, polyethylene glycol-coated particles have a longer circulation time in the body and thus have a better chance to accumulate within a tumor. The FDA approved albumin-bound paclitaxel nanoparticles (nabP) to be used for the treatment of metastatic breast cancer in 2004. The rationale for using drug-loaded nanoparticles in the treatment of cancer is the observation that nanoparticles accumulate passively in the tumor and thus can serve as a vehicle to deliver a high concentration of anticancer drugs

to tumors. This results in a high concentration of drug within tumor while minimizing systemic toxicity.

Active accumulation is dependent on the specific affinity of nanoparticles for cancer cells. Such affinity can be induced by several approaches including modification of the surface of nanoparticle with molecular-specific ligands such as folic acid (47), peptides (48), aptamers (49), and antibodies (26). Molecular targets that are available for breast cancer targeting were presented earlier in this chapter. Among different options for targeting, using monoclonal antibodies that bind tumor-associated antigens on the surface of cancer cells is the most commonly used approach.

This dissertation is dedicated to the development of a molecular-specific contrast agent for the detection of breast cancer cells in animal models using a novel laser optoacoustic imaging (OAT) system. Chapter three describes the fabrication of a molecular-specific contrast agent using gold nanoparticles and the monoclonal antibody Herceptin. Chapter four includes methods and experiments that were designed for the verification of biologic and binding profile of fabricated contrast agent. The performance of fabricated contrast agent to improve the sensitivity and specificity of optoacoustic method to detect cancer cells will be discussed in chapter five. Finally, in chapter six we summarize the results and discuss the future directions of this dissertation.

Chapter 2: Introducing Optoacoustic Tomography

In this chapter, after presenting a brief description of optoacoustic tomography (OAT), factors that affect the performance of this imaging technique *in vivo* are discussed. The role of angiogenesis for OAT of tumors will be discussed. Finally, the need for an exogenous contrast agent to enhance the sensitivity and specificity of OAT is discussed to justify this study.

2.1 BACKGROUND

OAT is a novel imaging technique in which an image is reconstructed by detecting acoustic waves that are generated within a sample upon laser pulse irradiation. Laser pulse irradiation generates acoustic waves as a result of thermoelastic expansion. The idea of generating sound by interrupted light belongs to Alexander Graham Bell. He reported that thin disks generate sound when exposed to interrupted sun light. This important observation is the basis of photoacoustic spectroscopy and OAT. Photoacoustic spectroscopy is a powerful technique that can be used to study the concentration of chemicals and gasses (50) and OAT is the subject of this study.

2.2 HOW DOES OAT WORK?

OAT is a novel non-ionizing imaging modality that allows for deep imaging of biological tissue up to a depth of several centimeters based on the differential light absorption of tissue components such as fat, melanin, and hemoglobin (51). Figure 3A shows the schematic of a typical optoacoustic experiment. In this figure, light-absorbing object A is embedded within a phantom that scatters light. The phantom is irradiated with a laser pulse from above, while an acoustic transducer located on the other side of the phantom detects acoustic waves generated within the phantom.

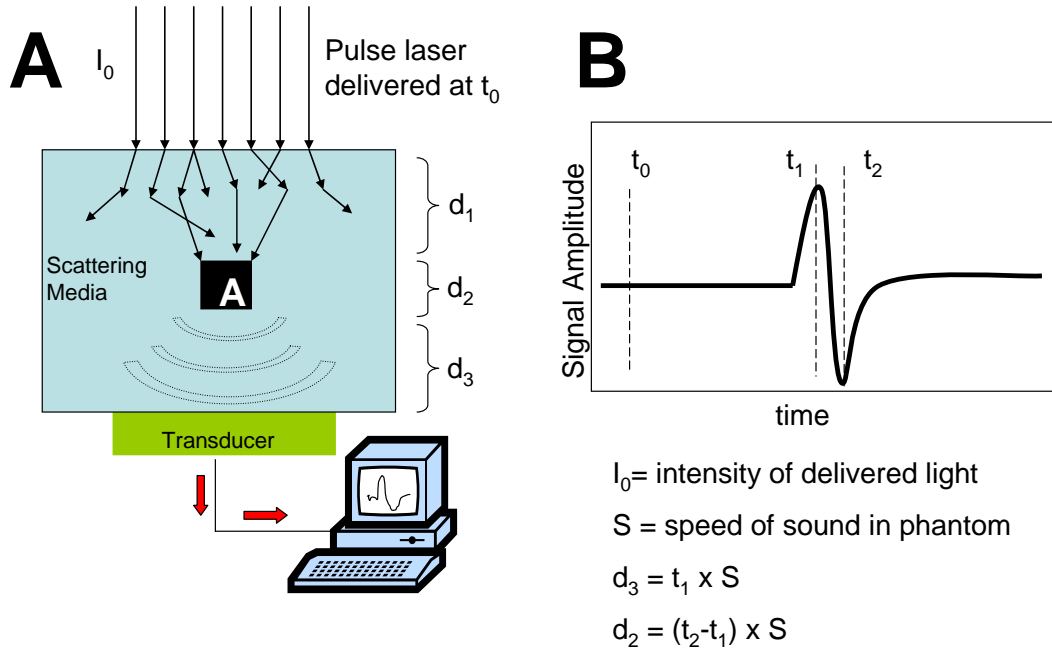


Figure 3: The schematics of a typical optoacoustic experiment (A) and resulting waveform (B). d_1 is the depth in which object A is located, d_2 is the diameter of light-absorbing object A, and d_3 is the distance between the object and transducer. t_0 is the time of arrival of laser pulse, t_1 is the time of arrival of signal from the front surface of object A that is closer to transducer, and t_2 is the time of arrival of signal from the counterpart surface. Formulas show the relation between time of arrival and the location of object.

When the phantom is irradiated with a laser pulse, photons propagate within the phantom while undergoing multiple scattering. Usually, a laser with a pulse width of a few nanoseconds is used for optoacoustic experiments. Note that the speed of light is 3×10^8 m/s, which means that the whole phantom and its embedded objects are irradiated almost at once. When photons hit object A, they will be absorbed. The energy of absorbed photons will be converted to heat, and this heat induces thermoelastic expansion of object A. Note that the thermoelastic expansion happens in a few nanoseconds during a short laser pulse. Rapid thermoelastic expansion generates transient acoustic waves by

light absorbing objects. The frequency of generated acoustic wave would depend on the dimensions and acoustic properties of the embedded objects.

Typically, generated optoacoustic waves possess a frequency from a few tens of kilohertz (kHz) to several megahertz (MHz). Thus, a wide-band acoustic transducer is required to convert optoacoustic waves (pressure waves) to electric signals. Acoustic transducers can be made of a variety of piezoelectric materials such as quartz crystal, ceramic, and Polyvinylidene Difluoride (PVDF). Due to the relatively high speed of light, all light-absorbing objects within the phantom will generate acoustic waves at once. Let t_0 be the time when laser pulse is triggered and the acoustic waves are generated. Generated acoustic waves propagate at the speed of sound in all directions within the phantom. The speed of sound varies by the density of tissue, but in a soft tissue it is roughly $1.5 \text{ mm}/\mu\text{s}$.

Figure 3B depict a typical optoacoustic signal in which the x-axis represents time, with zero being the time of triggering laser pulse (i.e. $t_0 = 0$). For a signal that arrives at t_1 , the distance between the object that generated that wave and the transducer, d_3 , could be determined by multiplying t_1 by the speed of sound in that media. Based on distance d_3 , acoustic waves will arrive at the transducer and appear on the monitor at a time that can be calculated by dividing d_3 by the speed of sound as depicted in figure 3B. Thus, the time interval between t_0 and t_1 is dictated by the distance between object and transducer (d_3) and inverse of the speed of sound within the phantom. The amplitude of the signal will depend on the extent of thermoelastic expansion, which depends on the light fluence at the target object and the absorption coefficient of the target object. To be more precise, the distance between object and transducer will affect the amplitude of the detected signal because the acoustic waves undergo gradual attenuation when they travel within the phantom. Based on the information provided in figure 3B and the speed of sound within the phantom, several parameters can be calculated:

- The distance between object and transducer is the product of the time of arrival of signal (t_1) multiplied by the speed of sound within phantom (S).
- The absorption coefficient of object A will be proportional to the amplitude of signal multiplied by the distance between object and transducer.
- The diameter of the object is the product of the time interval between two peaks of the signal (t_2-t_1). These peaks in the signal represent the signal originated from the front and back boundaries of the object. Thus, we can calculate their position by multiplying their time of arrival by the speed of sound in the phantom (S).

In summary, higher laser fluence will result in a stronger signal; a higher absorption coefficient of object will also result in a stronger signal. In contrast, a longer distance between object and transducer will result in a weaker signal, as the acoustic signal will attenuate as it travels within phantom; however, most tissues conduct acoustic waves efficiently and thus the attenuation of acoustic waves within tissue would be minimal. Based on the above discussion, one can expect to increase the amplitude of optoacoustic signal by increasing the fluence of light that is delivered to the target object and also by increasing the light absorption of target object. The laser fluence at the target object is dependent on the light intensity at the surface of the phantom (I_0), the attenuation coefficient of the phantom, and the depth of object within the phantom (d_1). Note that I_0 is limited by the specification of the laser device and by the maximum safe fluence of light that can be used for *in vivo* experiments without damaging skin. Thus, the amplitude of the generated acoustic signal will mainly depend on the light-absorption properties of the targets. This is the rationale for using a contrast agent to enhance the

light absorption of a specific target to subsequently generate a stronger optoacoustic signal.

In a more complex situation, one may use multiple transducers to record the generated acoustic signal at different angles. This would allow one to apply mathematical algorithms to calculate the exact location of objects within a phantom. Successful OAT of targets in turbid media is dependent on two parameters: the quality of recorded signal, and the efficiency of reconstruction algorithms. The theoretical bases of reconstructing image from optoacoustic signal detected by an array of transducers was first reported by Kruger et al. in 1995 (52). In this model, the ideal situation would be to arrange multiple transducers in a full circle around the object. Several other algorithms have been presented in the literature for image reconstruction of optoacoustic signal (53-55). Arranging transducers in a full circle around the phantom is technically challenging; instead, one could use a linear array of transducers or a semicircle array as depicted in figure 4.

There are many issues that have to be addressed before a useful OAT is reconstructed:

- The amplitude of signal that is generated by the light absorbing component within a phantom is dependent on the local fluence of laser light. Ideally, we should use a homogenous illumination within the phantom so that all objects are equally illuminated during laser pulse. In practice, laser devices do not provide a homogenous laser beam. Thus, additional optical components are required to illuminate the sample with a relatively homogenous beam. Also, we should be aware of the fact that local light absorption within a tissue will affect the pattern of laser

illumination behind light-absorbing components. Together, this means that the homogenous illumination of the sample is very important during OAT.

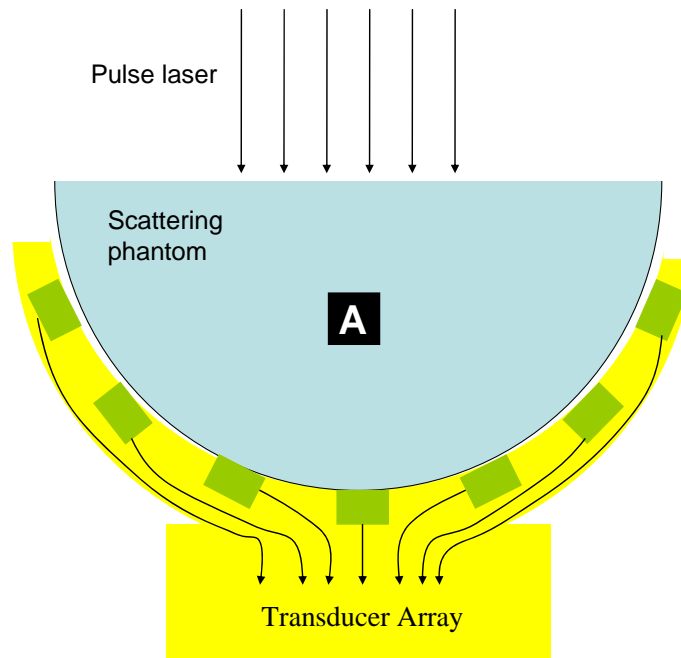


Figure 4: An array of acoustic transducers may be used to locate a light-absorbing object (a) within a scattering phantom. Several mathematical algorithms are available to locate the position of object A based on the phase and amplitude of the signal that arrives into individual elements within an array of transducers.

- The amplitude of generated acoustic signal is inversely proportional with the pulse width of laser to a point that the maximum acoustic pressure is generated (56). Typically, one would need a laser pulse with a pulse duration of 10 ns.
- The optical properties of phantom (scattering and absorption) will significantly affect the quality of the generated acoustic signal. A high scattering coefficient will help deliver a homogenous laser light to objects

and thus is favorable to OAT. In contrast, a high light absorption in the background will diminish the fluence of light at the target object and at the same time will increase the background signal. In other words, light absorption within the phantom will inversely affect the signal to noise ratio that will eventually determine the sensitivity of OAT. To increase the maximum depth of imaging, one would need to maximize signal to noise ratio. The signal originates from light-absorbing targets; to enhance signal to noise ratio, one would need to increase the light-absorption property of the target object. The background noise originates from the absorption of photons within the phantom; to minimize the noise, one would choose a wavelength for the laser pulse in which the background light absorption within the phantom is minimized.

- Any acoustic barrier that is located between the target object and the transducer may also affect the quality of recorded signal. This means that it is important to make sure that impedance matching is present between transducer and phantom. For instance, conventional ultrasound gel should be used to fill any gaps between transducer and phantom to facilitate the passage of ultrasound waves toward transducer.

2.3 OAT FOR BIOLOGICAL IMAGING

OAT can be used to image biological tissues. For instance, optoacoustic technique has been used by other groups to monitor hemoglobin concentration in the radial artery of healthy volunteers (57), to monitor retinal temperature during retinal laser irradiation (58), for three-dimensional tomography of mouse head (59), and for high-contrast vascular imaging in human finger and legs (60). When biological tissue such as skin is

irradiated with laser pulse, light-absorbing components within the tissue will generate acoustic waves as a result of thermoelastic expansion. Based on the wavelength of the light, elements such as melanin, hemoglobin, lipids, carotenes, and water will absorb light to generate acoustic waves. Tissues such as skin also strongly scatter light.

Within most tissue, hemoglobin is the most potent light-absorbing component in the visible range of spectrum. Figure 5 depicts the absorption coefficient of two types of hemoglobin (reduced and oxidized) and water at different wavelengths. As a result of strong absorption and scattering, the depth of penetration of photons within the body in the visible range of spectrum is limited to a few millimeters. As it can be seen in figure 5, hemoglobin will strongly absorb light at wavelengths shorter than 650 nm. Water will strongly absorb light in wavelengths longer than 900 nm. Overall, the light absorption of tissue is minimal within the range from 650 to 900 nm. The interval between 650 nm to 900 nm, which is also called the near-infrared region of the spectrum, is known as “the window to the body.” Photons at the near-infrared region of the spectrum penetrate better within most tissue. Note that although the absorption of photons is minimal at these wavelengths, the scattering of light within tissue is still quite prominent.

Another important parameter that needs to be considered when tissue imaging is desired is the scattering property of tissue. As light propagates within a tissue, photons get reflected or deviated from straight pathway when they hit tissue components. This is referred to as scattering property and is usually expressed as scattering coefficient. The scattering property of human breast varies by age and is different among people; however, it has been reported to be in the range of 0.7 to 1.0 mm^{-1} within the 700-900 nm wavelength in 28 healthy premenopausal women (61). The scattering will attenuate light as it propagates through tissue. This means that when one illuminates the surface of a phantom with a laser beam, the superficial layers will be exposed to a higher fluence of

light as compared to the deeper area. Now imagine that there are two identical light absorbing object located inn the superficial and deep layers of a phantom. Although these two objects have similar light absorption properties, the object that is located in the superficial layer will generate a stronger signal simply because it received more photons. This factor, which is considered as the light attenuation due to the scattering, should be taken into account when reconstructing an image during optoacoustic imaging. The reconstruction software that is used in this dissertation automatically estimates the light propagation pattern within an object and normalize the recorded signal.

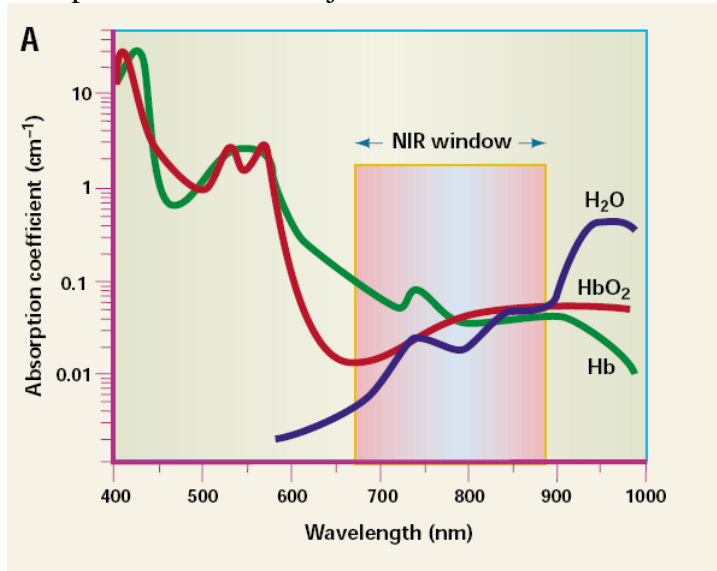


Figure 5: Absorption coefficient of reduced hemoglobin (Hb) and Oxyhemoglobin (HbO₂) and water at different wavelengths. The cumulative absorption coefficient is minimal in the range of 650 nm to 900nm that is known as the near-infrared region of the spectrum, NIR. Image is taken from reference (62).

The spatial resolution of optoacoustic method is limited by the spatial resolution that can be achieved by an ultrasound wave. Based on the experimental data presented in

the literature as well as theoretical calculations, OAT is expected to provide a spatial resolution of a few millimeters at a depth of 5 cm within tissue mimicking phantoms (63).

OAT requires laser pulse to be delivered deep within the sample. Based on the data presented in figure 5, only near-infrared photons can potentially penetrate deep within tissue. Thus, although OAT has been successfully used *in vitro* using a visible laser source to image targets at a depth of 5 cm within a turbid media (63), a near-infrared pulse laser is required to perform OAT *in vivo*. Note also that hemoglobin is the main light-absorbing component even in the near infrared region of the spectrum. In other words, hemoglobin is the main endogenous contrast agent for *in vivo* OAT at the near-infrared region of the spectrum.

2.4 OAT FOR BREAST IMAGING

OAT has been used in clinical studies for the imaging of breast cancer without using additional contrast agent(64;65); however, the application of this imaging method for the detection of breast cancer would depend on the presence and extent of abnormal angiogenesis that is essential to generate endogenous contrast. However, the application of OAT for the early detection of breast cancer may be extended by using an exogenous contrast agent as will be explained in the rest of this chapter. Breast is a near-ideal organ for optoacoustic imaging for the following reasons:

- Breast is an accessible organ. One could technically position most of human breast tissue between an array of an acoustic transducer and a light source. This would be similar to the set up that is currently used during conventional mammography as depicted in figure 6.

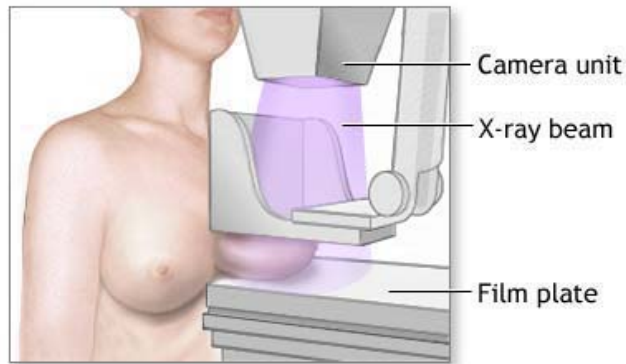


Figure 6: Positioning of human breast during conventional mammography. Similar setup could be used to position human breast between a laser light source and acoustic transducer during OAT. Image is taken from The New York Times published on 01-08-2008.

- Breast is a relatively homogenous tissue with no bone or air bubbles inside. This is important because both bone and air bubbles strongly attenuate ultrasound. For instance, organs such as brain that is enclosed with bones and lung that contain air bubbles are not good candidates for OAT.
- The background light absorption of breast tissue is minimal. The major component of breast tissue is fat, which has a relatively low absorption coefficient at the near-infrared when compared to other tissues such as muscle or liver. This is important because it means that fat will generate a weak background optoacoustic signal. This is important because a low absorption within breast means that deep illumination of breast tissue is possible using near-infrared laser illumination. Deep illumination , (i.e. ~5 cm for breast imaging) along with the lack of bone and air in the breast means that OAT can be used to image targets that are located deep within breast tissue.

- Because the peak absorption pattern of gold nanoparticles is tunable over a relatively wide band, more than one type of gold nanoparticles could be imaged using optoacoustic method. For instance, by using two laser lines at NIR region and employing two types of gold nanorods that possess distinct peak absorption (each conjugated to a separate targeting vehicle), one would be able to image two different targets within tissue.

2.5 ANGIOGENESIS AS AN ENDOGENOUS CONTRAST AGENT FOR OAT

The presence of a tumor with abnormal angiogenesis alters the light-absorption pattern within the affected area of the breast. OAT reconstructs images based on the pattern of light absorption, and thus breast tumors could potentially be detected using optoacoustic technique based on their abnormal angiogenesis. In other words, abnormal angiogenesis increases the blood content of a tumor and an increase in the blood content will enhance the light absorption within a tumor that will eventually lead to a stronger optoacoustic signal from the tumor; because of this, abnormal angiogenesis is considered as an inherent contrast agent for OAT. Figure 7 depicts gross appearance of a breast tumor. In this figure, the tumor can easily be identified by its darker color as compared to the normal surrounding tissue. Dark appearance of the tumor is a result of enhanced angiogenesis that increases the blood content of tissue as well as bleeding and necrosis within the tumor.

To investigate the extent of angiogenesis in the mouse model that we have used in this dissertation, BT-474 breast cancer cells were injected subcutaneously into nude mice to produce tumors (the details of the procedure will be addressed in the following chapter). After 6 weeks, the approximate diameter of tumor was 10 mm. The animals were sacrificed and samples of skin, subcutaneous tissue, and tumor were extracted and

fixed in 4% formalin. The samples were stained using a Blood Vessel Staining Kit (Millipore, Billerica, MA) to reveal vWF antigen, a widely used indicator for blood vessels.

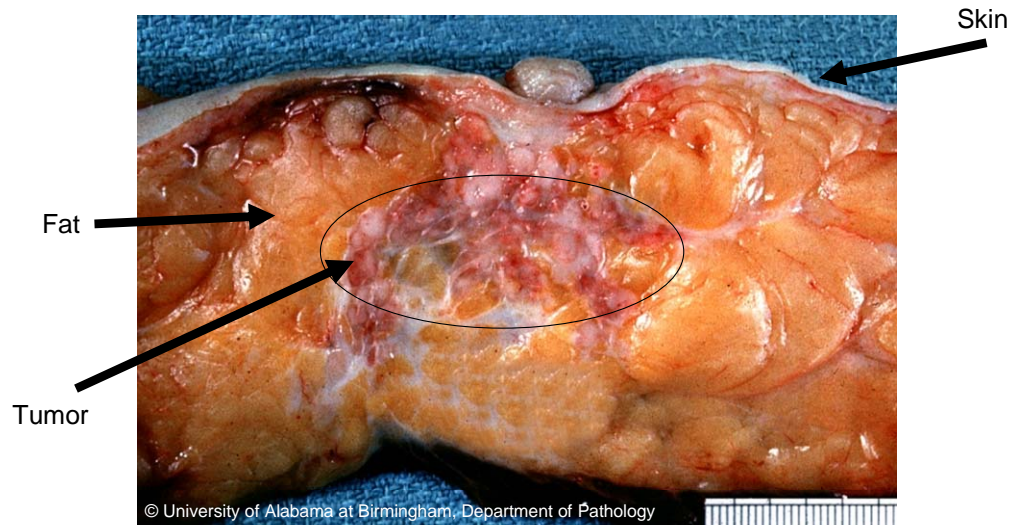


Figure 7: Macroscopic cross section of breast adenocarcinoma in human. Tumor looks darker as compared to its surrounding tissue due to enhanced angiogenesis, which increases its blood content. Image is taken from the website of the University of Alabama at Birmingham.

An example of the images that were acquired in this experiment is presented in figure 8. The results confirm enhanced angiogenesis, especially in the periphery of the tumor, as compared to normal skin.

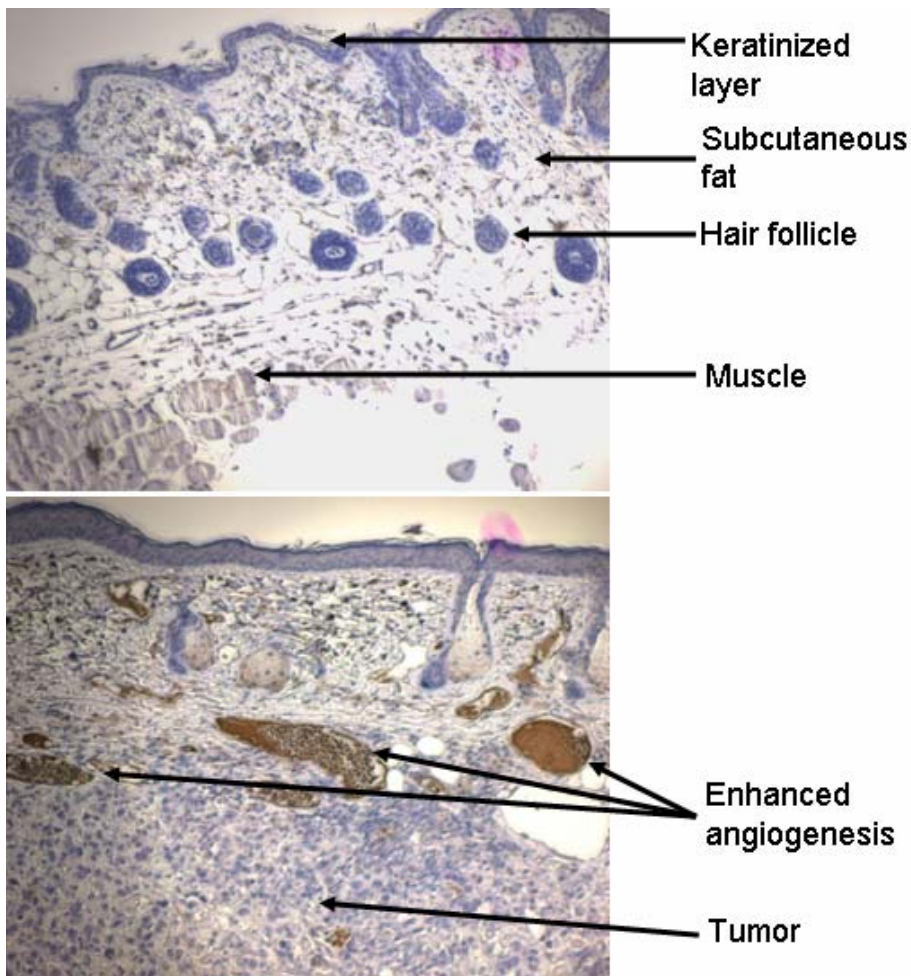


Figure 8: Immunostaining of the skin of tumor-bearing mouse using vWF as a marker of blood vessels. vWF appears brown. Normal mouse skin (top) shows minimal angiogenesis. Areas of enhanced angiogenesis are present around the tumor (bottom).

Figure 8 also shows that the enhanced angiogenesis mostly occur within the periphery of the tumor; this has been well described in the literature (66). The fact that the central areas of tumor do not have a rich blood supply further indicates that angiogenesis alone would not be a suitable contrast for OAT as the central area of tumors will not generate a strong optoacoustic signal. An example of the images that were

acquired in this experiment is presented in figure 8. The results confirm enhanced angiogenesis, especially in the periphery of the tumor, as compared to normal skin.

2.6 THE NEED FOR AN EXOGENOUS CONTRAST AGENT TO ENHANCE THE SENSITIVITY AND SPECIFICITY OF OAT

OAT has successfully been used on human subjects to image breast cancer (64;65), port-wine stains (67), quantify epidermal melanin (68), determine hemoglobin and its oxygen saturation (69), and angiography (70). In the previous section, we explained why OAT using near-infrared laser pulse is a potential imaging technique for the evaluation of human breast as well.

Although OAT promises non-invasive imaging of breast tumors in the presence of abnormal angiogenesis, the extent of angiogenesis may not be sufficient at early stages of tumor development to produce a detectable optoacoustic signal; which is defined as a signal to noise ratio of two or more. Currently, the sensitivity and specificity of the optoacoustic method is not sufficient to detect a tumor at early stages, mainly due to the low signal-to-noise ratio at early stages of tumor development (unpublished data of the author). To resolve this issue, the signal to noise ratio of OAT needs to be improved. Potential solutions for this problem include:

- 1) Use a stronger laser source to generate a stronger signal. Unfortunately, safety issues limit the maximum intensity of laser irradiation that can be used *in vivo* to avoid tissue damage.
- 2) Use a more sensitive acoustic transducer and related electronics to achieve a low background noise. Significant advances have been made in making high quality acoustic transducers; however, some internal

noise is unavoidable within the transducer and electronic circuits, and this will limit the sensitivity and specificity of OAT.

- 3) Use an exogenous contrast agent that specifically enhances the signal generated in the target tissue by enhancing the light absorption of cancer cells.

This third approach is the subject of this dissertation. In other words, increasing light absorption within diseased tissue will improve the sensitivity, while the specific accumulation of contrast agent within a tumor will improve the specificity of the optoacoustic method to detect tumors (63;71). An increase in the sensitivity and specificity of OAT will facilitate the detection of those small lesions that are otherwise undetectable. The enhancement of sensitivity and specificity of OAT for the detection of breast tumors is depicted in figure 9.

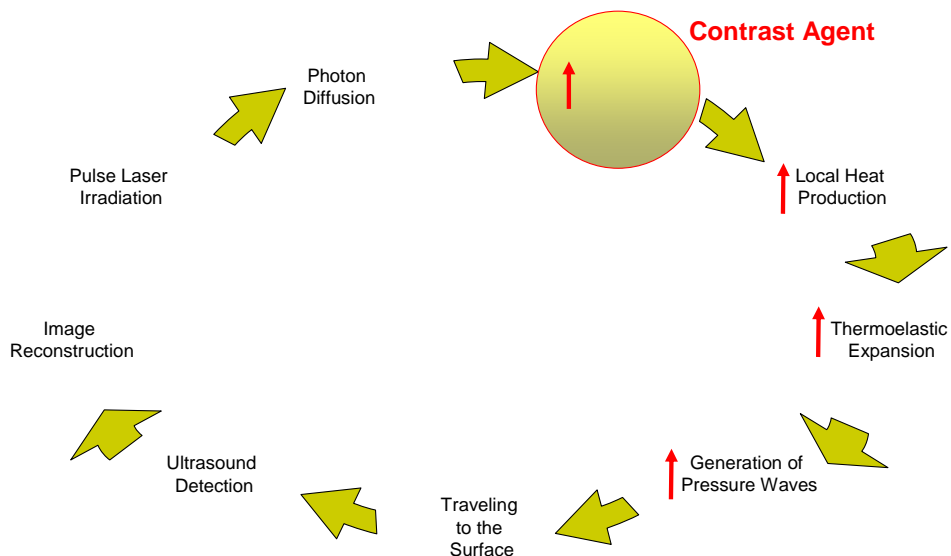


Figure 9: Basics of enhancing the efficiency of optoacoustic imaging using a contrast agent. Contrast agent could enhance the sensitivity of optoacoustic imaging by increasing the amplitude of generated signal. The specificity could also be enhanced by targeting contrast agent specifically to cancer cells.

Light absorbing materials such as Indocyanine Green (ICG) has successfully been used as a contrast agent for OAT (72); however, high concentrations of this dye is required to generate detectable optoacoustic signal. New materials are required to provide us with a higher light absorption at low concentration to enhance OAT detection of small tumors.

Chapter 3: The Application of Nanotechnology for Molecular-Specific Targeting of Breast Cancer

Nanotechnology can be used at this stage to provide us with materials that are superior to organic dyes in terms of light absorption. While several types of nanoparticles are available or are under investigation in biomedical sciences, we will focus of gold nanoparticles that strongly absorb light and thus are potential candidate as contrast agents for OAT.

In this chapter, spherical gold nanoparticles are presented as an efficient contrast agent for OAT. Protocols to make spherical gold nanoparticles in different sizes are explained and methods are presented to functionalize these nanoparticles by conjugating them to monoclonal antibodies. Several *in vitro* experiments are presented to demonstrate the feasibility of using spherical gold nanoparticles as a contrast agent for OAT. The results presented in this chapter have already been published in a peer-reviewed journal (63) and have been presented at several scientific conferences.

3.1 INTRODUCING GOLD NANOPARTICLES

For the purposes of this dissertation, gold nanoparticles were chosen for the development of a contrast agent for OAT because of their unique optical, chemical, and biological properties(73;74). We will review these unique properties here.

3.2 OPTICAL PROPERTIES OF SPHERICAL GOLD NANOPARTICLES

The extent and quality of motion of electrons greatly affect the physicochemical properties of a material. Certain types of electron motions are allowed within orbits of atoms or molecules. In a metal, some electrons are shared and can freely move between atoms within a lattice. These freely moving electrons are responsible for the electric conduction of metals (73). By decreasing the size of a metal particle, a new confinement

is induced for the conducting electrons that limit the motion of electrons in the lattice. When the size of metal particle is reduced to nanometer scale, this extra confinement may allow electrons to vibrate along the dimensions of nanoparticle. This kind of electron vibration is called plasmon resonance and may be stimulated by absorbing photons that have similar resonance frequencies, leading to enhanced light absorption. In other words, the interaction between photons and the conducting electrons in a nanoparticle causes enhanced light absorption by metal nanoparticles.

When a solution of spherical nanoparticles is examined using a spectrophotometer, a peak absorption can be determined in which the plasmon resonance frequency of conducting electrons equals the wavelength of the light. For instance, spherical gold nanoparticles with an average diameter of 40 nm show a peak absorption that is located near 520 nm (i.e., green). Blood strongly absorbs light at this wavelength and this is why both blood and spherical gold nanoparticles appear red in to eyes. The fact that the light absorption of spherical gold nanoparticles overlaps with that of blood is a disadvantage for using these types of nanoparticles in vivo; however, this will not affect in vitro experiments that are performed in the absence of blood. The surface plasmon resonance frequency of metal nanoparticles can be calculated by solving Maxwell's equation (75); however, such a calculation is beyond the scope of this dissertation. The plasmon resonance frequency of a given gold spherical nanoparticle depends on many factors including the diameter of those nanoparticles. The correlation between the peak absorption wavelength and the size of gold nanoparticles has been investigated by many groups (75). In this dissertation, light-absorption spectra of nanoparticles will be used to determine the peak absorption. This will determine the plasmon resonance frequency of manufactured nanoparticles.

Spherical gold nanoparticles are usually made by Turkevitch's method. In this method, gold salts are reduced in a solution to make gold nanoparticles:



By controlling the ratio of concentration of AuCl_4^- to $\text{C}_6\text{H}_8\text{O}_7$, one could make gold nanoparticles in different sizes. The diameter of a nanoparticle determines the plasmon resonance frequency, which will in turn determine the light-absorption properties of the nanoparticle. The relationship between the size of spherical gold nanoparticle and its light-absorption pattern is depicted in figure 10.

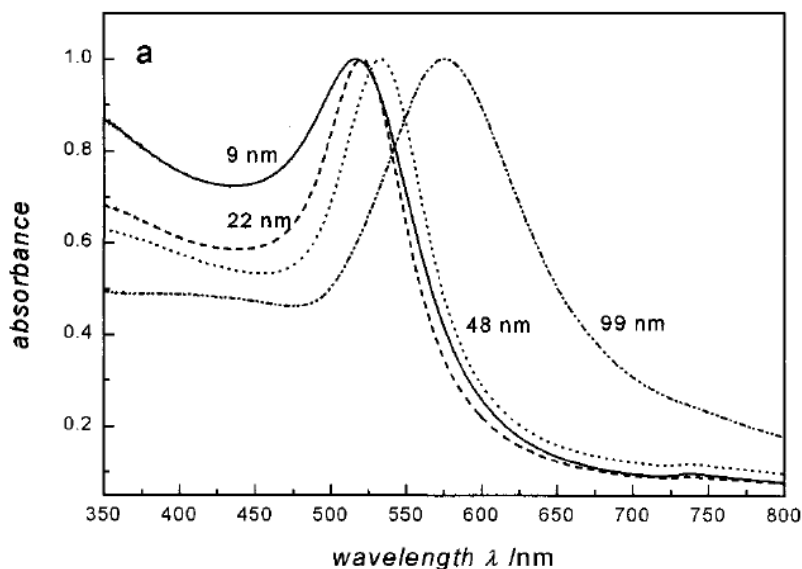


Figure 10: The absorption pattern of spherical gold particles with different sizes. Larger particles show a shift of their peak absorption to the right. Figure is taken from reference (75)

Due to their exceptionally strong light absorption, gold nanoparticles are capable of producing a strong optoacoustic signal. A strong optoacoustic signal generated by gold

nanoparticles upon laser irradiation would allow one to detect a small concentration of these nanoparticles within tissue. This is particularly important when molecular imaging of a specific marker is desired. In the past, we have used spherical gold nanoparticles with a plasmon resonance frequency at the visible range of spectrum as contrast agent for *in vitro* detection of cancer cells. The results of our initial experiments demonstrated a promising sensitivity of optoacoustic method to detect Her2/neu over-expressing cancer cells *in vitro* (63).

The plasmon resonance frequency of spherical gold nanoparticles is located at the visible range of spectrum, which means that a visible laser pulse illumination is required for the particles to generate optoacoustic signal. Unfortunately, biological tissues strongly attenuate visible light and thus do not allow visible light to penetrate deep within tissue.

3.3 FABRICATING FUNCTIONALIZED SPHERICAL GOLD NANOPARTICLES FOR *IN VITRO* EXPERIMENTS

Gold nanoparticles are made in the form of colloidal gold, a uniform and stable suspension of gold nanoparticles in a media that contains a chemical stabilizer. For the purposes of this dissertation, citrate-stabilized spherical gold nanoparticles were synthesized using a standard protocol known as the Turkevitch method (75). In this method, H₂AuCl₄ is reduced by adding sodium citrate to produce Au⁰ that aggregates to form nanoparticles. The diameter of produced gold nanoparticles was adjusted in the range of 20 to 40 nm by controlling the ratio of the concentration of H₂AuCl₄ to that of the reducing agent. The average diameter of produced nanoparticles was determined by measuring peak absorption using a conventional spectrophotometer and comparing this to a standard graph that shows the relationship between the size of spherical gold nanoparticles and their average diameter (76). Figure 10 shows the relationship between

the size of spherical gold particles and their light-absorption pattern. In this figure, an increase in the size of spherical particles shifts the peak absorption of spherical gold nanoparticles to longer wavelengths.

Bioconjugation of spherical gold nanoparticles to antibodies, which was first invented by Faulk and Taylor in 1971(77), revolutionized molecular visualization of cellular components by electron microscopy. Due to their high density, individual gold nanoparticles were easily identified in electron microscopy. Immunogold staining enabled scientists to visualize single molecule proteins or receptors in tissue sections using electron microscopy. Unfortunately, these gold nanoparticles were too small to be seen using light microscopy. Another important invention was the development of the silver enhancement technique(78), in which silver salts are deposited over gold nanoparticles to make them visible under light microscopy. This further broadened the applications of gold nanoparticles in biology.

Preparing a uniform and stable suspension of immuogold nanoparticles, which are gold nanoparticles attached to antibodies, is a challenge. Although it is not well understood, the adsorption of antibodies to spherical gold nanoparticles is thought to be the result of three major interactions (see figure 11):

- The electrostatic attraction between negatively charged nanoparticles and positive side chains of the protein. For instance, lysine side chains that contain amine functional group carry positive charge at neutral pH.
- The hydrophobic interactions between the surface of gold nanoparticles and the hydrophobic domains of the protein.
- Dative bonds between gold surface and free sulfhydryl side chains of a protein.

Most antibodies have both hydrophobic domains and many lysine functional groups on their surface. This means that the electrostatic and hydrophobic interactions occur easily between gold nanoparticles and most antibodies. These interactions seem to be sufficient to produce stable conjugates that are suitable for immunogold staining of samples for electron microscopy. However, the situation is different for *in vivo* applications: there are many other proteins and ions in the blood that may compete with original antibody to bind to gold nanoparticle; this may lead to the detachment of original antibody from gold surface and attachment of serum proteins to gold nanoparticles. This means that immunogold particles that are made based on non-covalent attachment of antibodies to gold surface cannot be used for *in vivo* applications. To solve this problem, we proposed attaching antibodies to gold nanoparticles using a dative bond rather than using electrostatic or hydrophobic forces. Because dative bonds are as strong as covalent bonds, they will not break in the serum and thus the conjugated particles can still remain functional *in vivo*.

Cysteine carries a sulfhydryl side chain and several cysteines exist in an antibody molecule; however, native antibodies carry their cysteines in the form of disulfide bond rather than free sulfhydryl groups. For instance, most immunoglobins (IgGs) have four interchain and four intrachain disulfide bonds (79). This means that antibodies *per se* do not carry a free sulfhydryl, and thus a free sulfhydryl group should be added to antibodies before they can be attached to gold nanoparticles using a dative bond (see figure 12).

There are at least two ways to induce a free sulfhydryl group on antibodies:

- Reducing some of the disulfide bonds that exist within antibody to form free sulfhydryls. This can be done using reducing agents such as 2-mercaptoethylamine (MEA).

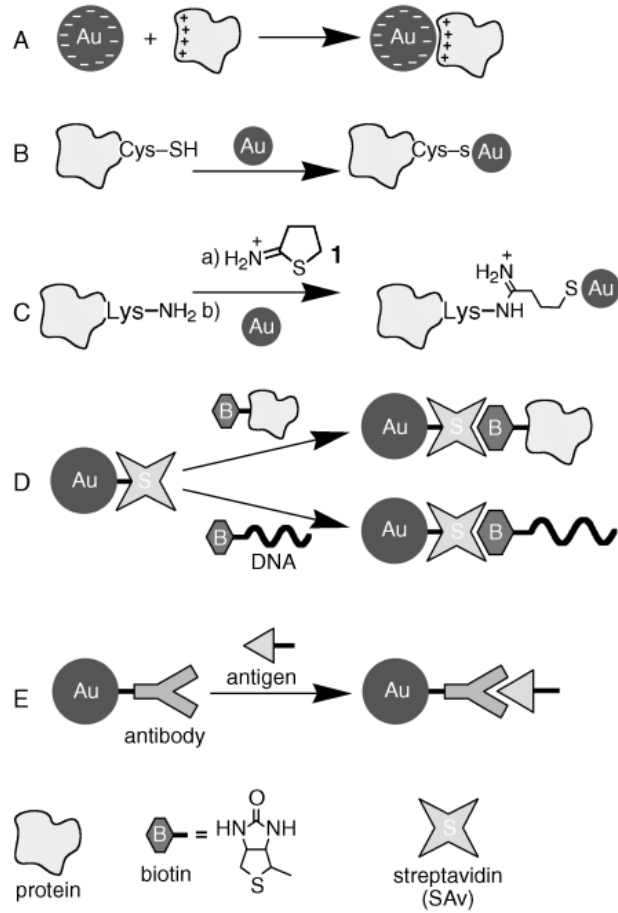


Figure 11: Different techniques that have been utilized to conjugate spherical gold nanoparticles: A) electrostatic adsorption of positively charged proteins to negatively charged nanoparticles, B) inherent thiol group of proteins that has affinity for gold, C) converting amine side group of proteins to thiol, D) Biotin-streptavidin linker system, E) secondary antibody (80)

- Modifying free amine side chains of proteins to sulfhydryls by using reagents such as SATA(N-Succinimidyl-S-acetylthioacetate)(81).

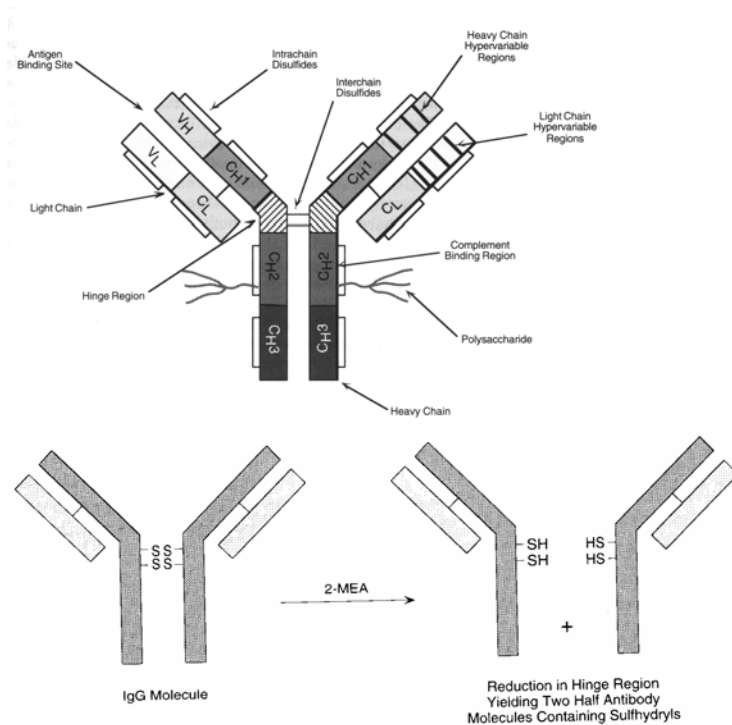


Figure 12: IgG molecule contains several disulfide binds in its structure (top). Controlled reduction of disulfide binds results in the production of two half antibodies with intact antigen binding sites and free thiol group (bottom). Free thiol groups can be used to conjugate these proteins to gold nanoparticles.

Due to their wide applications in electron microscopy, a variety of gold nanoparticles that are already attached to streptavidin are available in the market. Streptavidin is a tetrameric protein with a molecular weight of 4x16 kDa that has an exceptionally high affinity for biotin, which is a small molecule also known as Vitamin H(82). With a dissociation constant of 1.3×10^{-15} M, the interaction between biotin and Streptavidin is one of the strongest non-covalent interactions in biochemistry. The affinity of biotin for Streptavidin is at least 10^4 times stronger than that of antibodies for antigen, as the latter has a dissociation constant in the range of 10^{-7} to 10^{-11} M. Because

of their high affinity and their ease of use, we used Streptavidin-biotin system to functionalize spherical gold nanoparticles in this dissertation. Monoclonal antibody was Biotinylated using commercial kits and incubated with Streptavidin-conjugated 40 nm gold nanoparticles to produce a functional gold nanoparticle.

Citrate-stabilized nanoparticles were further functionalized by attaching them to monoclonal antibody Herceptin that specifically binds to the Her2/neu receptors that are known to over-express on the surface of many breast cancer cells. Her2/neu receptor was selected for this experiment because it is one of the most studied tumor markers for breast cancer and also because Herceptin, a monoclonal antibody that binds to this receptor, is in clinical use with promising results for the treatment of metastatic breast cancer. A schematic of the conjugated particles is presented in figure 13.

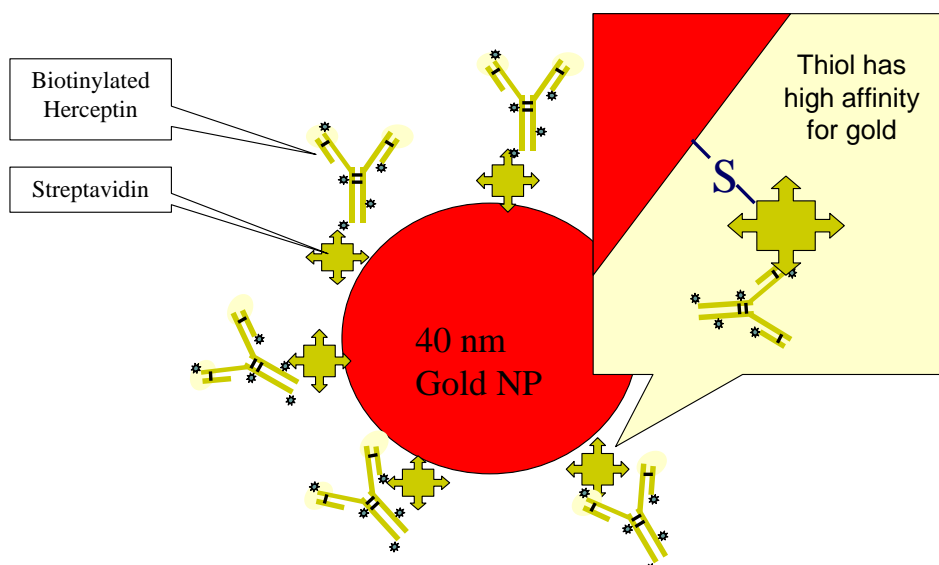


Figure 13: Schematics of bioconjugation of Herceptin to spherical gold nanoparticles using Streptavidin-biotin system. Herceptin was biotinylated and then incubated with Streptavidin-conjugated gold nanoparticles to produce a functionalized nanoparticle.

Streptavidin-conjugated 40 nm spherical gold nanoparticles were obtained from Ted Pella, Inc. (Redding, CA). Herceptin was Biotinylated using a kit provided by Pierce Biotechnology (Rockford, IL). Biotinylated Herceptin was incubated with Streptavidin-conjugated nanoparticles to fabricate Herceptin-conjugated spherical gold nanoparticles. Unattached Herceptin was removed using centrifugation. A secondary antibody (Cy3-conjugated goat anti-human antibody) was used as recommended by the manufacturer (Jackson ImmunoResearch, West Grove, PA) to visualize conjugated particles under fluorescent microscopy. The binding of conjugated nanoparticles was confirmed on the breast cancer cell line SK-BR3 that is known to over-express Her2/neu receptor. To do this, SK-BR3 cells were incubated with conjugated gold nanoparticles, and the presence of gold nanoparticles on cancer cells was then shown both by using a fluorescent technique as well as electron microscopy (Figures 14, 15).

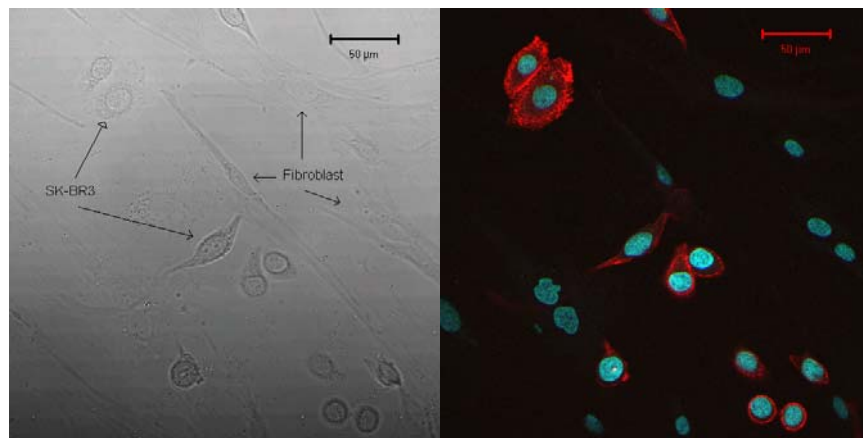


Figure 14: Mab binds specifically to HER2-positive cells. A. Bright field microscopy distinguishes elongated cells human fibroblasts from rounded SK-BR-3 cells. Cells were incubated with MAb-conjugated spherical gold nanoparticles and Cy3-conjugated secondary antibody as described in Materials and Methods. The nuclei were stained with DAPI. Red color is indicative of Mab-conjugated nanoparticles bound to HER2 receptor on the surface of cancer cells.

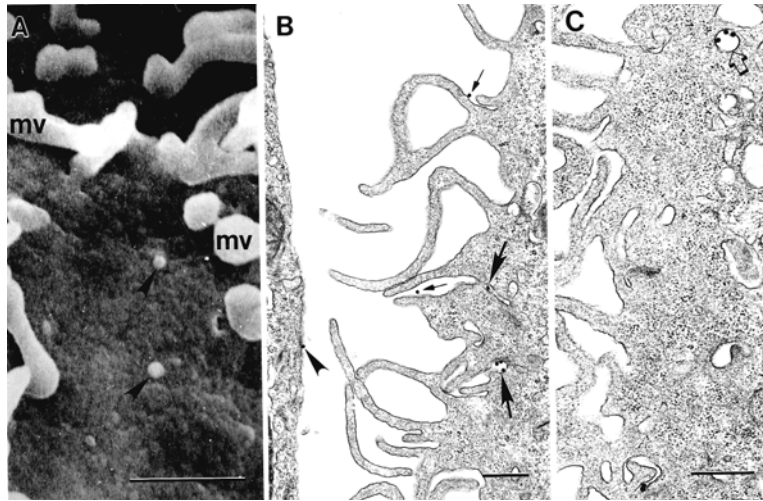


Figure 15: Electron microphotographs of SK-BR3 cells incubated with Herceptin-conjugated gold nanoparticles (NP). A. SEM showing two gold nanoparticles (arrowheads) directly on the cell surface. mv - microvilli. B. TEM of an ultrathin section. NP adherent to the cell surface (arrowhead) and to the surface of microvilli (thin arrows) or in the process of internalization (thick arrows) into vesicles where the channel connecting them to the cell surface can be seen; C. TEM of an ultrathin section. NP internalized in a cytoplasmic vesicle (open arrow). Bars = 0.5 micrometers.

3.4 DETERMINING THE OPTOACOUSTIC PROFILE OF SPHERICAL GOLD NANOPARTICLES

Several in vitro experiments were conducted to determine the sensitivity of the optoacoustic method to detect low concentrations of gold nanoparticles. Figure 16 depicts the schematic and results of a typical experiment in this series, in which a cylinder was made of a mixture of gelatin and whole milk to resemble optical scattering of tissue and was placed on top of a single-element optoacoustic transducer (WAT-20, LaserSonix Technologies, Houston, TX). A small well with an approximate volume of 100 μ L was

made on the top surface of the phantom to hold the nanoparticle solutions. Proper optical elements were used to illuminate the sample from top surface using a Q-switched Nd-YAG laser (Big Sky Lasers, Inc. Bozeman, MT) emitting at the wavelength of 532 nm, pulse repetition rate 20 Hz, and pulse length of 14ns. The optical fluence at the sample site was measured as 4.8 mJ/cm². The amplitude of optoacoustic signal was recorded using a digital oscilloscope. The sample with a concentration of 10⁹ nanoparticles per mL produced a detectable optoacoustic signal (i.e. a signal-to-noise ratio > 2). This corresponds to a nanoparticle concentration close to 10⁻⁵ μM. This experiment demonstrates the high sensitivity of OAT to detect gold nanoparticles within a turbid medium. Each data point in figure 16 represents three measurements. It is noteworthy to mention that the minimum detectable concentration of gold nanoparticles *in vivo* would be affected by the background level of signal that is generated within tissue in the absence of gold nanoparticles. We will address this issue in the following chapter where we describe the similar experiments using gold nanorods.

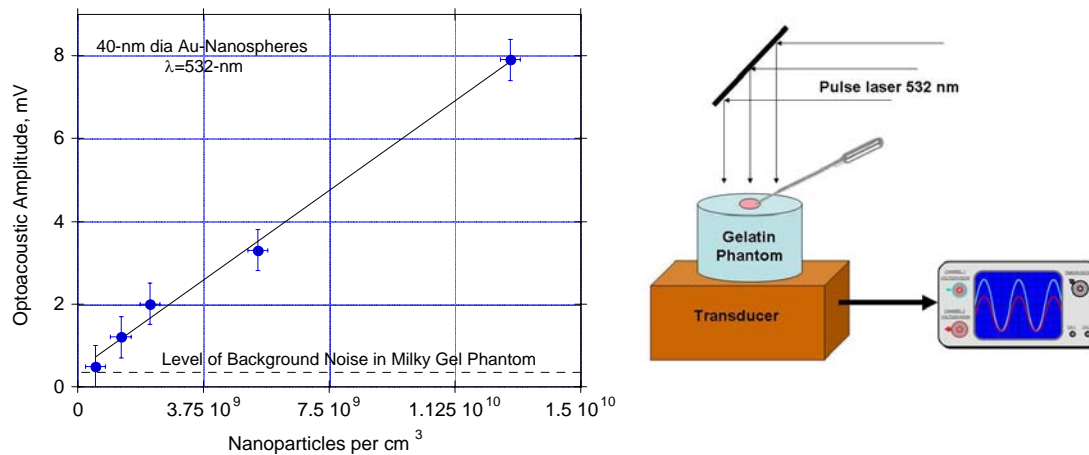


Figure 16: The amplitude of optoacoustic signal as a function of spherical nanoparticles' concentration (left). Gold nanoparticles with an average diameter of 40 nm are detectable at a minimum concentration of 10⁹ nanoparticles per mL. Schematic of the experiment setup (right).

3.5 OPTOACOUSTIC IMAGING OF SPHERICAL GOLD NANOPARTICLES WITHIN PHANTOM GEL

A series of experiments were designed and conducted to assess if OAT can be used to image targeted cancer cells *in vitro*. To do this, SK-BR3 cells were used as a cancer cell line that over-expresses Her2/neu receptor. SK-BR3 cells were incubated with Herceptin-conjugated gold nanoparticles at a concentration of 10^9 NPs/mL at 4°C to inhibit internalization of the receptor upon antibody binding; treated cells were then harvested and embedded within a gelatin phantom that optically resembled human breast at near infrared region of the spectrum (i.e. absorption coefficient = 0.01 mm^{-1} , scattering coefficient = 1 mm^{-1}). Untreated cancer cells were also used as a control, but they didn't produce a detectable optoacoustic signal due to their negligible light absorption (data not shown).

Figure 17 depicts one of these experiments: The phantom was illuminated from the top with laser pulses at the wavelength of 532 nm. The laser beam had a Gaussian profile with incident energy fluence of 10 mJ/cm^2 and a diameter of 30 mm (visible as a light smeared line in the upper part of the optoacoustic image). The phantom was made using 90 g of gelatin powder (Sigma, St.Luis, MO) and 10 mL of whole milk (Oak Farms, Dallas, TX); water was added to make a total volume of 1L. Three tubes with an internal diameter of 4 mm and length of 11 mm were embedded in the center of the phantom at the depth of 5 cm from the illuminated surface and 4 cm from the array of transducers. The tubes were filled with three media: the same gel as used in the phantom as a negative control, gold 40 nm spherical nanoparticles in concentration of 10^9 NP/cm^3 as a positive control, and breast cancer SK-BR3 cells targeted with gold nanoparticles.

As can be seen in figure 17 right, while the negative control is invisible in optoacoustic image (object a), the positive control (object b) and targeted SK-BR3 cells (object c) were brightly visible in optoacoustic image.

Figure 18 demonstrates another example of these series of experiments in which four objects each with an approximate volume of 30 to 50 μL were embedded within the phantom: a solution of 10^9 NPs/mL as a positive control and three objects made of 10, 25, and 100 million SK-BR3 cells treated with conjugated nanoparticles. In this figure, an increase of the optoacoustic signal as a function of the number of treated cells can be seen. According to figure 18, the minimum detectable number of cancer cells using OAT is 25 million at a volume of 50 μL , which is very promising as compared to the minimum detectable size of tumors using conventional mammography ($\sim 125\mu\text{L}$).

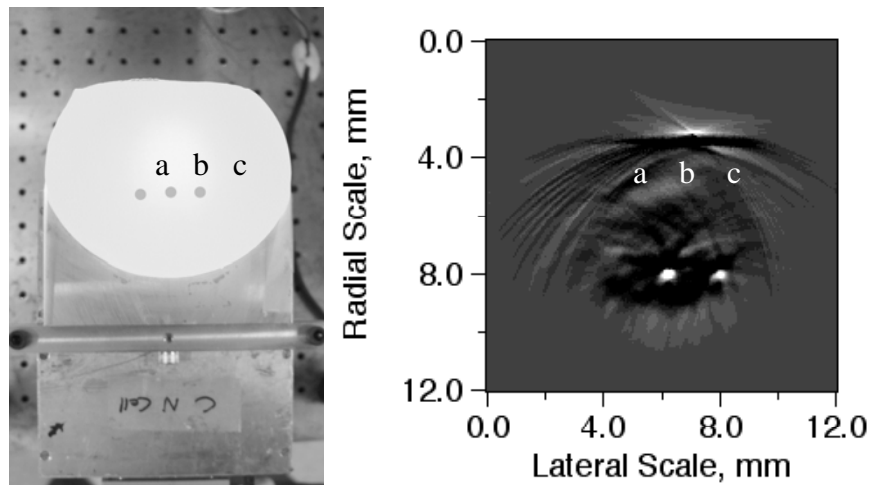


Figure 17: Photograph of a disk-shaped gel phantom placed on the arc-shaped optoacoustic transducer array (left) and an optoacoustic image of the same phantom (right). The tubes were filled with the same gel as used in the phantom (a), spherical gold nanoparticles at a concentration of 10^9 NP/cm³ (b), and targeted breast cancer cell SK-BR3(c). Gold nanoparticles and targeted cancer cells are brightly visible under optoacoustic imaging (right)

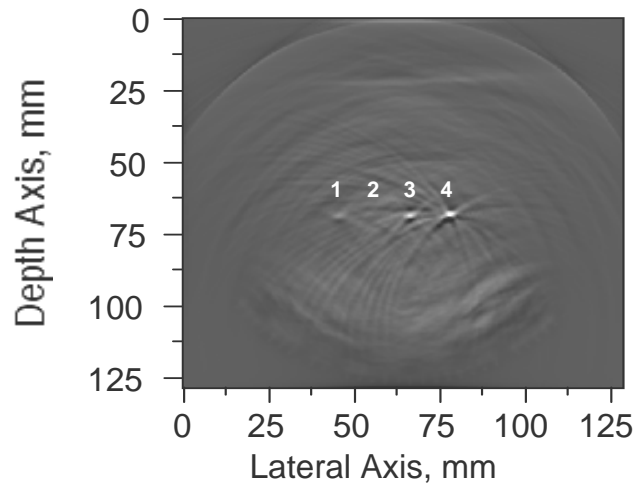


Figure 18: Optoacoustic image of gelatin phantom with four embedded objects made of SK-BR3 cells that were treated with conjugated NPs. Object 1 is NP with a concentration of 2×10^9 NP per mL (Visible), object 2 is 10 million SKBR3, object 3 is 25 million SKBR3 (Visible), and object 4 is 100 million SKBR3 cells loaded with Mab/NPs (Brightly visible).

Chapter 4: Employing non-spherical gold nanoparticles for OAT

In this chapter, non-spherical gold nanoparticles will be presented. A series of theoretical analysis along with the results of experiments are discussed to justify the use of functionalized gold nanorods as a contrast agent to enhance the sensitivity and specificity of OAT *in vivo*. The results presented in this chapter has already been published in peer-reviewed journals (83;84).

4.1 NON-SPHERICAL GOLD NANOPARTICLES ARE SUPERIOR TO SPHERICAL GOLD NANOPARTICLES FOR *IN VIVO* EXPERIMENTS

In the previous chapter, we discussed how gold nanospheres strongly absorb light at their plasmon resonance frequency, which is located at 520 nm for a nanosphere with a diameter of 40 nm. Unfortunately, photons at this wavelength hardly penetrate human tissue mainly due to the strong light absorption of components such as hemoglobin and myoglobin. This limits the *in vivo* application of spherical gold nanoparticles for OAT. On the other hand, light absorption of most tissue is minimal at the near-infrared region of the spectrum. In addition, the scattering of light, which will attenuate the incident of light as light propagates within tissue, is minimal at near infrared region as compared to the visible light; this will also help NIR to penetrate deeper tissue.

In vivo detection of cancer cells using gold nanoparticles and optoacoustic imaging method requires engineering of gold nanoparticles that strongly absorb light in the near-infrared region of the spectrum where the light absorption of tissue is minimal. This will provide high signal to noise ratio for deep *in vivo* optoacoustic detection (85). Fortunately, plasmon resonance frequency of gold nanoparticles could be tuned over a wide range from visible to the near-infrared region of the spectrum by adjusting the shape

and dimensions of these nanoparticles (86). To tune the plasmon resonance frequency at near-infrared, it is required to change the shape and size of gold nanoparticles. When gold particles are made in the form of nanoshells, the ratio of the thickness of the gold layer to the diameter of the particle dictates the plasmon resonance frequency (see figure 19). As for the elongated particles, the aspect ratio would be the main factor that determines the plasmon resonance frequency. The plasmon resonance frequency of gold nanoparticles can be calculated by solving Maxwell's equation (86); however, this topic is beyond the scope of this dissertation. Other groups have calculated the plasmon resonance frequency of gold nanoparticles at different shape and sizes, and the results are available in the literature.

Near-infrared light in the range of 600 nm to 1300 nm wavelength penetrates deep within tissue (85;87). Thus, nanoparticles with strong near-infrared absorption should be used for *in vivo* OAT. As mentioned before, the peak absorption of gold nanoparticles can be tuned to the near-infrared region of the spectrum by changing the size and shape of these particles. At this time, at least three forms of gold nanoparticles with strong near-infrared absorption have been identified: gold nanoshells, gold nanorods (GNRs), and nanocubes (86). Figure 19 right demonstrates the relation between shell thickness and the peak absorption of gold nanoshells. Figure 20 shows electron microscopy image and the light-absorption pattern of gold nanocages with an approximate dimension of 30 nm (88).

4.2 GOLD NANORODS AS CONTRAST AGENTS FOR OAT

To be used as a contrast agent for OAT, the agent should strongly absorb light in the near-infrared region of the spectrum. Figure 21 shows how changing the aspect ratio of gold nanorods can be used to tune their plasmon resonance frequency from red to the

near-infrared light. Ideally, one would choose the particle that provides the highest light absorption for the volume of the particle. Other specifications such as biocompatibility and the availability of chemical methods to functionalize the particle using targeting agents, as will be described in chapter five, are also important. The fact that gold nanoparticles strongly absorb light due to their plasmon resonance was discussed earlier in this chapter. Now the question to be answered is thus: What types of gold nanoparticles are the best to be used as contrast agents for OAT?

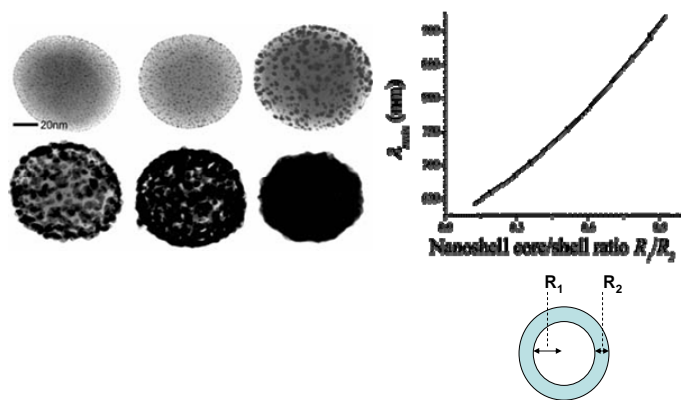


Figure 19: Plasmon resonance frequency of gold nanoshells depends on the core/shell ratio. By increasing the core/shell ratio, for example by making the shell thinner, the peak absorption of the nanoparticle could be shifted to longer wavelengths. Figure is taken from reference (89).

Among the different types of gold nanoparticles that absorb light in the near-infrared region of the spectrum, GNRs are the best for OAT because they provide maximum absorption for their size. In addition, their peak absorption can be tuned in the near-infrared by adjusting the aspect ratio of these nanoparticles. Light-absorption cross-section of different types of gold nanoparticles has been calculated by other groups (86) by solving Maxwell's equation. El-Sayed calculated the expected absorption and scattering properties of different types of gold nanoparticles (86). The relation between

the aspect ratio of gold nanorods and their peak absorption is presented in figure 21. A table of the results of his calculation is presented in figure 22. In this figure, GNRs have been shown to provide the highest light absorption per volume of gold nanoparticles.

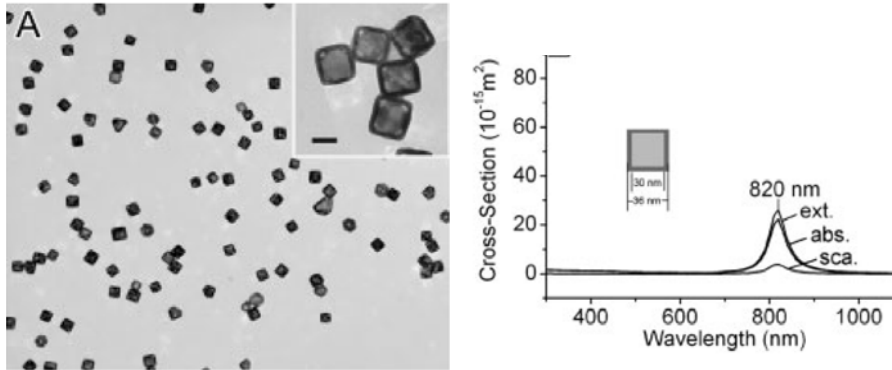


Figure 20: TEM (left) and absorption spectrum (right) of gold nanocages. Plasmon resonance frequency of gold nanocages is located in the near infrared region of the spectrum. Ext. = extinction, abs. = absorption, sca. = scattering. Figure is taken from reference (88).

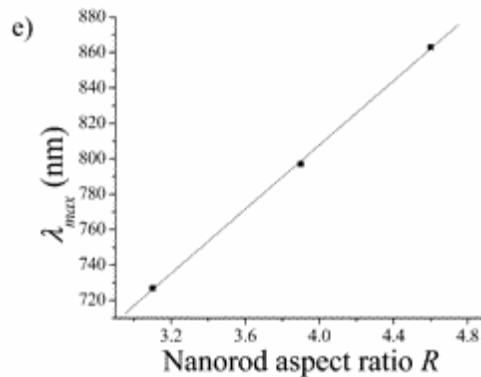


Figure 21: The relation between aspect ratio of gold nanorods and their peak absorption wavelength. By increasing aspect ratio, gold nanorods absorb light at longer wavelengths. Graph is taken from reference (86).

nanoparticle type	dimensions	λ_{max} nm	$\mu_a(\lambda_0)$ / μm^{-1} (nm)
silica-gold nanoshells	$R_1 = 40$ nm $R_2 = 70$ nm	843	50.61 (843)
silica-gold nanoshells	$R_1 = 50$ nm $R_2 = 70$ nm	704	20.57 (704)
silica-gold nanoshells	$R_1 = 60$ nm $R_2 = 70$ nm	892	35.66 (892)
silica-gold nanoshells	$R_1 = 90$ nm $R_2 = 105$ nm	984	11.07 (984)
silica-gold nanoshells	$R_1 = 120$ nm $R_2 = 140$ nm	1120	7.61 (730)
silica-gold nanoshells	$R_1 = 120$ nm $R_2 = 155$ nm	1160	7.26 (582)
gold nanospheres	$D = 20$ nm	521	73.72 (521)
gold nanospheres	$D = 40$ nm	528	87.36 (528)
gold nanospheres	$D = 80$ nm	549	67.88 (549)
gold nanorods	$R = 3.1$	727	741.86 (727)
gold nanorods	$r_{NR} = 11.43$ nm $R = 3.9$	797	907.09 (797)
gold nanorods	$r_{NR} = 11.43$ nm $R = 4.6$	863	1003.87 (863)
gold nanorods	$r_{NR} = 11.43$ nm $R = 3.9$	788	986.56 (792)
gold nanorods	$r_{NR} = 8.74$ nm $R = 3.9$	815	601.47 (817)
gold nanorods	$r_{NR} = 17.90$ nm $R = 3.9$	842	449.34 (842)
gold nanorods	$r_{NR} = 21.86$ nm		

J. Phys. Chem. B, Vol. 110, No. 14, 2006, 7238

Figure 22: Size-normalized absorption cross-section of different types of gold nanoparticles. Note that GNRs possess the strongest absorption for their size. Table is taken from reference (86).

Figure 22 also demonstrates that gold nanoshells can be made to absorb infrared light however, the absorption cross section of these nanoshells would be smaller than that of gold nanorods when they are made at similar sizes (see figure 22, right column). In this dissertation, a seed-mediated method was used to produce GNRs with an aspect ratio in the range of 3 to 4 to tune their peak absorption at the near-infrared region of the spectrum(90-92). The detail of the protocol used to make these gold nanoparticles is available in Appendix A. A calculated comparison between the light absorption of spherical gold nanoparticles with a diameter of 40 nm and GNRs with an aspect ratio of four (dimensions 12 x 50 nm) is presented in figure 23 (74). Figure 24 demonstrates the absorption spectra of GNRs with an aspect ratio of 3. In this figure, there is a peak absorption around 520 nm, which corresponds to the transverse plasmon resonance, and

another stronger peak at 700 nm, which is due to the axial plasmon resonance frequency of GNRs. The change in the shape of gold nanoparticles from spherical to nanorods shifts the peak absorption to a longer wavelength and also enhances the amplitude of light absorption of nanoparticles (93). Figure 25 demonstrates how changing the aspect ratio of GNRs modulate their light-absorption pattern.

Concentration = 10^7 NPs per mL = 100 femto Molar

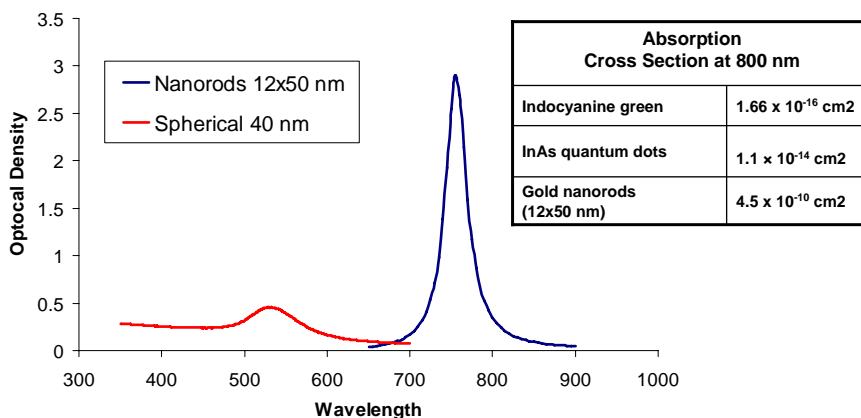


Figure 23: Absorption spectra of spherical gold nanoparticle as compared to that of cylindrical. Note that by changing the shape of the nanoparticle to a cylinder, the peak absorption shifts toward longer wavelengths and its amplitude becomes stronger.

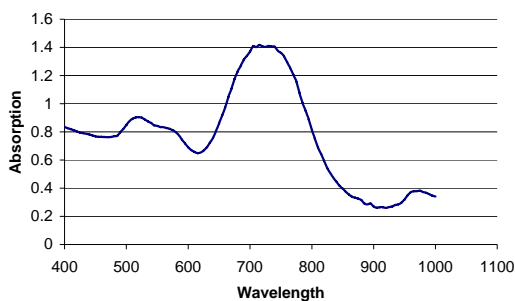


Figure 24: Absorption spectra of GNRs with an aspect ratio of 3 as was prepared in our laboratory.

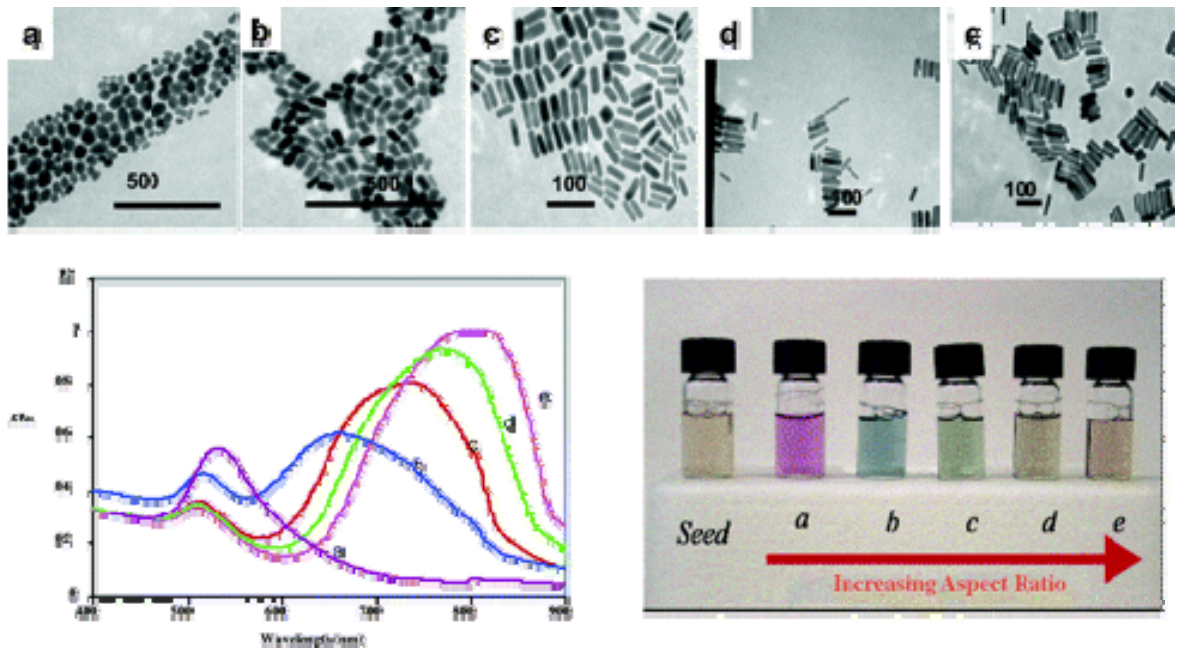


Figure 25: Aspect ratio of gold nanorods determine their optical light absorption. Transmission electron microscopy images (top), light absorption pattern (low left), and visual appearance of (low right) gold nanospheres (seed), and nanorods with aspect ratio of 1.35 (a), 1.95 (b), 3.06 (c), 3.50 (d), 4.42 (e). (94)

After reviewing the optical properties of different shapes and sizes of gold nanoparticles, we selected GNRs for OAT because they provide the strongest light absorption for their size and commercial lasers are available to irradiate them at their peak wavelength(73;75). While several types of gold nanorods with different aspect ratios were made in our lab, figure 26 shows a typical absorption spectrum for GNRs with an estimated aspect ratio of 3.3 that were produced for OAT in our laboratory. This particular aspect ratio was chosen because the peak absorption spectra of these nanorods is close to the emission wavelength of the Alexandrite laser and thus can be efficiently excited using the Alexandrite laser.

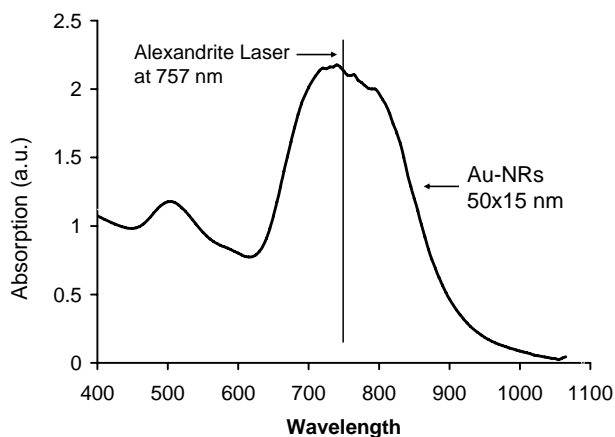


Figure 26: Absorption spectrum of raw GNRs with an approximate size of 50x15 nm. The peak absorption is close to the emission wavelength of the Alexandrite laser at 757 nm.

Another interesting property of GNRs is their ability to be detected using a variety of techniques such as transmission electron microscopy (95), dark field microscopy (93), multi-photon excitation laser scanning microscopy (96), optical coherence tomography (97), Raman spectroscopy (98), conventional X-ray (99), and CT scan imaging (100).

One of the most exciting properties of GNRs is their ability to emit light under two-photon excitation. It has been suggested that a single GNRs could be detected using two-photon excitation microscopy (101). To investigate if our GNRs emit light under two-photon excitation, 10 μ l of gold nanorod solution was spotted on a glass slide and examined under two-photon microscopy using an excitation wavelength at 800 nm, a power of 5 mW at objective lens level, and a Zeiss 20X objective lens with a numerical aperture of 0.75. GNRs were found to be exceptionally bright (see figure 27). Due to technical issues, we were not able to adjust the laser energy at lower energy levels for this experiment; however, gold nanoparticles have been imaged using much lower excitation power levels in the literature (102).

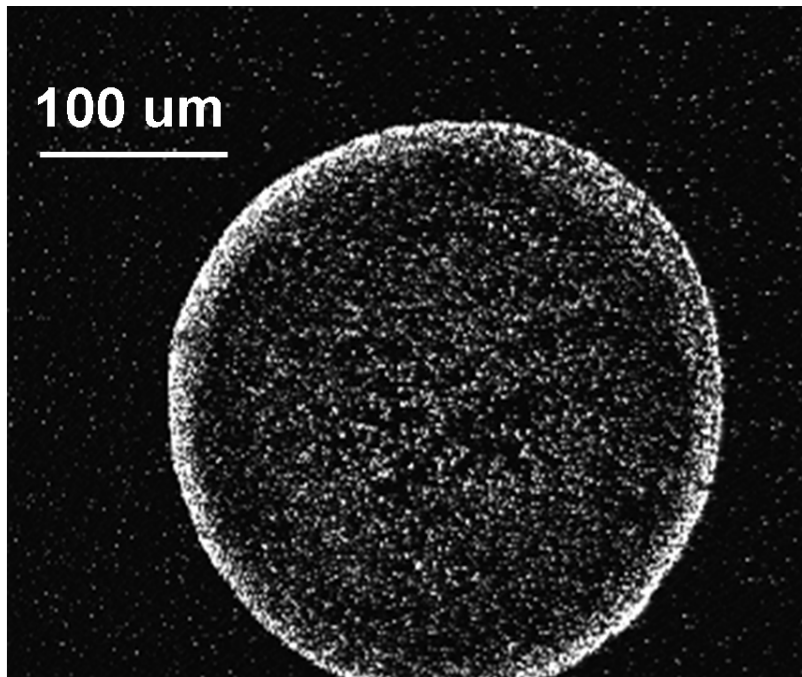


Figure 27: Gold nanorod solution as seen under two-photon excitation microscopy using a 20X objective lens. Gold particles were found to be exceptionally bright even when using an excitation power as low as 5 mW at sample site.

In this experiment, a relatively low power was used for two-photon detection of GNRs. In this low power, most of conventional fluorescent dyes do not fluoresce, allowing one to detect bright GNRs easily against a dark background.

Increasing excitation power to 50 mW caused disappearance of GNRs emission under two-photon excitation. The mechanism for losing two-photon emission when a higher excitation power is used is not well-understood, but it has been suggested that a high excitation power probably melts these nanoparticles and turns them into nanospheres (73).

In another experiment, a few microliters of gold nanorods solution were injected directly into chicken muscle, and the sample was then examined under two-photon

excitation at 800 nm. Fifty slices were captured from the surface to a 100 μm depth using a 20X objective lens and then all images were collapsed together to generate figure 28. The control image, which was taken before the injection of gold nanorods was uniformly black (image not shown). As one can see in this figure, gold nanorods that diffused within the sample enabled us to visualize the fine structure of the sample tissue under two-photon microscopy. This demonstrates the feasibility of tracking gold nanorods by using multiple modalities such as OAT as well as two-photon excitation microscopy.

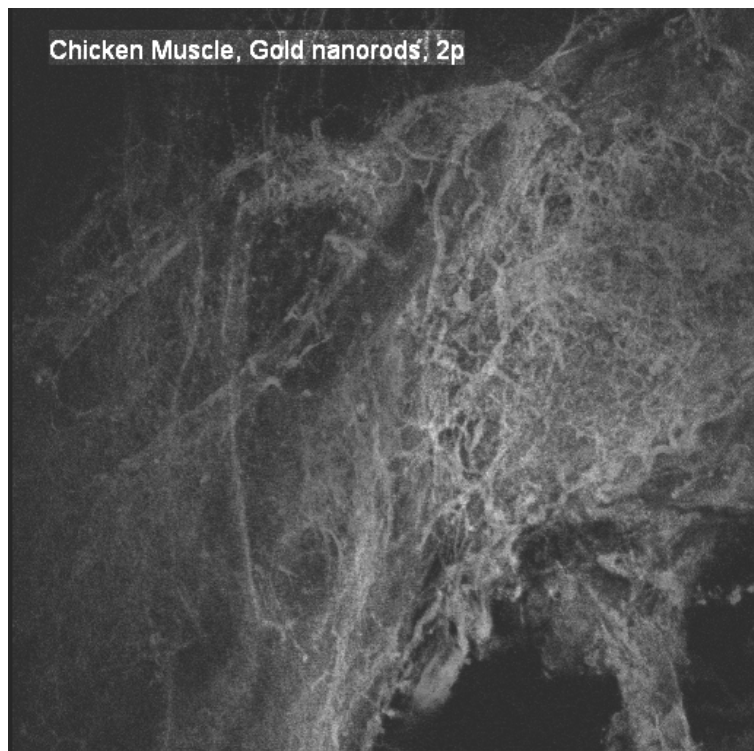


Figure 28: Two-photon excitation microscopy of chicken muscle injected with gold nanorods. Gold nanorods appear bright under two-photon excitation. Actual size of imaged area is 640x640 micrometers.

GNRs also possess desirable chemical properties: they are chemically stable and thus do not interact with other components that exist in a tissue microenvironment. At the same time, special chemical techniques are available to functionalize gold nanoparticles

as necessary (46;103-105). Gold nanoparticles have been widely used in the past with minimal complications to treat a variety of diseases including rheumatoid arthritis and cancers, and thus it appears that they are well tolerated by the human body even after several years (106;107).

4.3 CRYSTAL STRUCTURE OF GNRS AND THE ROLE OF HEXADECYLTRIMETHYLAMMONIUM BROMIDE ON BIOCONJUGATION

In chemical literature, a three-digit number is used to describe the crystal structure on the surface of gold nanoparticles. Figures 29 and 30 depict crystal structure of GNRs as revealed by high-resolution transmission electron microscopy and x-ray crystallography. For instance, 111 and 100 are low energy crystal structures and thus are relatively stable (108;109). The details of the crystal classification are beyond the scope of this dissertation; however, it is worth mentioning that while the crystal structure of gold nanospheres is mainly composed of the stable 111 configuration, the crystal structure of the side walls of gold nanorods is 110 that is the unstable form. The unstable form of 110 facets is only found in GNRs. The thiol group has affinity for the ends of GNRs (105). Hexadecyltrimethylammonium bromide (CTAB), the surfactant, has more affinity for 110 surfaces and so it will engulf gold nanorods from sides while the ends remain exposed. CTAB is required for the generation of gold nanorods using seed-method technique that will be described in the following section. This special arrangement of CTAB molecules around gold nanorods is being used for making GNRs with a high aspect ratio. This has been illustrated in figure 31, as reported by Murphy's group (94). Like CTAB, thiol group has different affinities for different crystal structures, and this property has been used to assemble controlled two- or three-dimensional lattices of GNRs as depicted in figure 32 (110) (111).

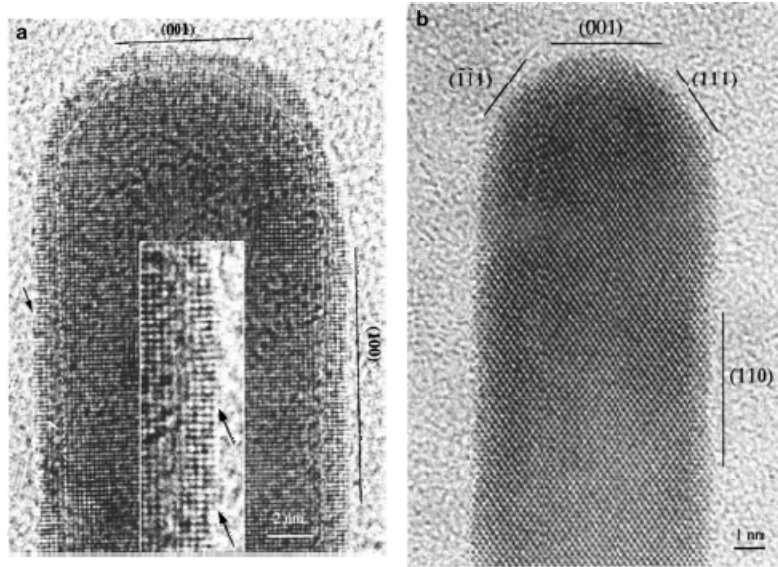


Figure 29: Crystal structure of GNRs as revealed by high-resolution transmission electron microscopy. Images are taken from reference (109).

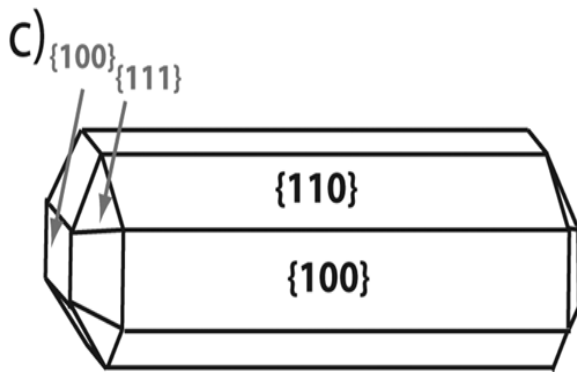


Figure 30: Crystal structure of GNRs. Image taken from reference(112).

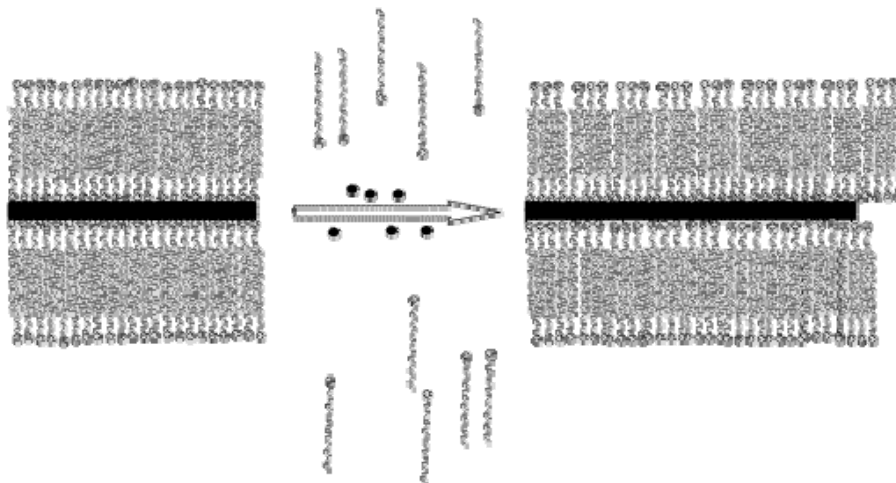


Figure 31: CTAB assembles into a lipid bilayer around gold nanoparticles and only allows the growth of gold nanoparticles in one dimension. Growth of gold nanoparticles in one dimension produces GNRs that are protected by the CTAB bilayer. Cartoon is taken from reference (90)

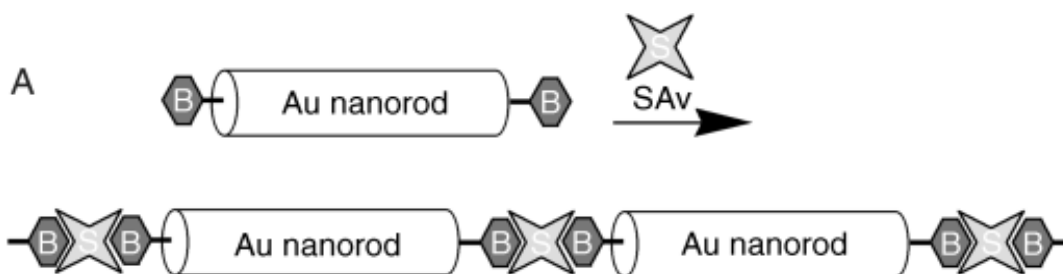


Figure 32: End-to-end assembly due to the attachment of biotin to the ends of GNRs. Figure is taken from reference (80).

4.4 RATIONALE TO FUNCTIONALIZE GOLD NANORODS

The main goal of this dissertation is to increase the sensitivity and specificity of OAT to detect breast tumors *in vivo*. The background light absorption of cells in the near infrared region of the spectrum is so minimal that it will not generate detectable

optoacoustic signal while illuminated with pulse laser light at conventional intensities. This means that cells *per se* cannot be seen using OAT. To improve sensitivity, one would need to maximize the generated optoacoustic signal by increasing the light absorption of cancer cells as much as possible. A higher light absorption will lead to a stronger optoacoustic signal at a fixed illumination power and thus will enhance the signal-to-noise ratio of optoacoustic signal. Contrast agents may be used to selectively enhance the light absorption of a tumor. The objective of tumor targeting is to selectively accumulate an intravenously injected material within tumors. Tumor targeting has both diagnostic and therapeutic applications; however, only diagnostic applications will be discussed here.

Gold nanoparticles are proven to possess a much stronger light absorption cross-section than conventional dyes. To tune light absorption around 750 to 800 nm, one would need to fabricate elongated gold nanoparticles with an aspect ratio of 3 to 4. The absorption cross-section of GNRs with a dimension of 12x50 nm is reported to be $4.5 \times 10^{10} \text{ cm}^2$ at 800 nm, while that of indocyanine green is $1.66 \times 10^{-16} \text{ cm}^2$ at similar wavelengths (113). This means that the light absorption of a single gold nanoparticle is up to a million times stronger than that of a single indocyanine green molecule. Due to their strong light absorption in near-infrared, gold nanoparticles produce a strong optoacoustic signal upon laser pulse irradiation; this enables them to be detectable even at very low concentrations. We have reported previously that the amplitude of light absorption of spherical gold nanoparticles increases linearly by increasing the volume of individual nanoparticles, and that the amplitude of generated optoacoustic signal is proportional to the volume of gold nanoparticles (63). This means that larger particles generate stronger optoacoustic signal simply because they absorb more light and thus are better choices for optoacoustic detection. Thus, from the optoacoustic point of view,

larger particles are superior due to their stronger signal. However, other considerations must be addressed before choosing a specific size for gold nanoparticles for *in vivo* applications.

In tumor targeting, a diagnostic or therapeutic agent is injected into the venous system. This agent will circulate in the body through blood circulation and as it passes through capillaries, it may exit circulation and diffuse into the extracellular space where it can directly interact with cells of our organs such as breast, liver, spleen, and kidney. Based on the size and composition of injected materials, they will be cleared from blood circulation by organs of the reticuloendothelial system (RES) or by kidneys. When gold nanoparticles are injected intravenously, they circulate within blood vessels until they are cleared via one of the methods described above.

Kidneys are capable of excreting into urine small nanoparticles with an average diameter of a few nanometers; however, nanoparticles that are studied in this dissertation are too large to be excreted into urine. This means that kidneys do not play a major role in clearing our nanoparticles from blood stream. However, it is expected for gold nanoparticles to be trapped within kidneys due to the rich blood perfusion of kidneys. As kidneys do not play a major role in clearing gold nanoparticles from blood, it is the responsibility of the RES to clear gold nanoparticles from the blood stream.

To achieve a successful targeting for OAT using gold nanoparticles, the following issues should be considered:

- The stability of a nanoparticle solution is due to a balance between the aggregating and repelling forces that exists between nanoparticles. The heavy mass of nanoparticles favors precipitation. On the other hand, repulsive forces exist to prevent precipitation. Repelling force between nanoparticles can be expressed as zeta potential that is a function of the

surface charge of nanoparticles and the ionic strength of the surrounding environment. A higher surface charge leads to a stronger repelling force. Zeta potential of “as synthesized” CTAB-coated GNRs are reported to be around +30 mV (114). Zeta potential is not dependent on the size of nanoparticles and remains the same for small and large nanoparticles with similar surface characteristics; however, increasing the size of nanoparticles will increase the mass of nanoparticles by cubic radius of nanoparticles. This means that in larger particles, the zeta potential may not be sufficient to produce sufficient repelling force to prevent precipitation and thus nanoparticles will precipitate. Practically, gold nanoparticles larger than 250 nm in diameter precipitate quickly and thus are not suitable for *in vivo* applications.

- Nanoparticles need to diffuse out of blood vessels before they can interact with cancer cells that arise from solid organs such as breast and prostate. In other words, nanoparticles need to be small enough to pass through pores in the wall of capillaries. Several lines of evidences suggest that smaller particles have a better chance to diffuse out of blood vessels and penetrate into a tumor (115). While the size of fenestra in the wall of an intact capillary is less than 5 nm in diameter (116), it has been found that blood vessels that are formed within a tumor possess larger pores with a diameter in the range of 200 to 1200 nm (42). This large pore size is due to the abnormal angiogenesis that exists within tumor. When a tumor grows beyond 2 mm³, simple diffusion does not provide enough nutrients for cancer cells; thus, cancer cells secrete angiogenic factors that result in abnormal angiogenesis (4). Endothelial vessels that are produced within a

tumor are diseased and leaky because they are made as a result of tumor angiogenesis rather than as a result of a normal physiologic process. The differential leak between healthy and diseased tissue is advantageous because by tuning the size of nanoparticles, one could allow nanoparticles to diffuse out of blood vessels exclusively within diseased tissue but not within normal tissue. To achieve a selective tumor accumulation, one would need to design nanoparticles that are large enough to avoid extravasation within normal tissue while also being small enough to pass tumor blood vessels. This size-based accumulation of materials within a tumor is also called passive tumor accumulation.

- The rate of nanoparticle clearance from blood is highly dependent on nanoparticle size. This is especially important for the clearance of particles by spleen. Particles larger than 150 nm are quickly cleared from blood stream by spleen. In contrast, spleen uptake was found to be insignificant when particles smaller than 60 nm in diameter were injected intravenously (117). As a conclusion, injected nanoparticles should not be larger than 150 nm or they will be cleared from blood by spleen before they get a chance to accumulate in their targets tissue.
- Surface chemistry of nanoparticles also plays an important role in determining the rate of nanoparticle clearance from blood. For instance, hydrophobic particles are quickly cleared from the blood stream by liver. This means that one would need to coat nanoparticles with polar and hydrophilic materials to elongate their circulation time. Examples of these hydrophilic materials that have been used for this purpose include poloxamers, poly(ethylene oxide), and poly(ethylene glycol) or PEG

(118). Each molecule of PEG with a molecular weight of 5000 Da is expected to cover an area as large as 32 nm^2 on the surface of gold nanoparticles (115;119). Coating nanoparticles with PEG with a molecular weight of 1900 to 5000 Da is the most popular method for coating of nanoparticles to hide them from RES. It is important to ensure that coating the surface of gold nanoparticles with PEG or any other molecule does not interfere with the light-absorption pattern of particles. This has been examined for PEGylated GNRs in our lab; results are presented in figure 33. It is suggested that PEG coating induces steric stabilization and thus brings a mechanism to avoid opsonization, which is a method that our body uses to tag foreign materials such as bacteria and viruses so that they can be identified and cleared from the blood stream by RES. In summary, PEG interferes with opsonisation and thus elongates the circulation time of injected materials.

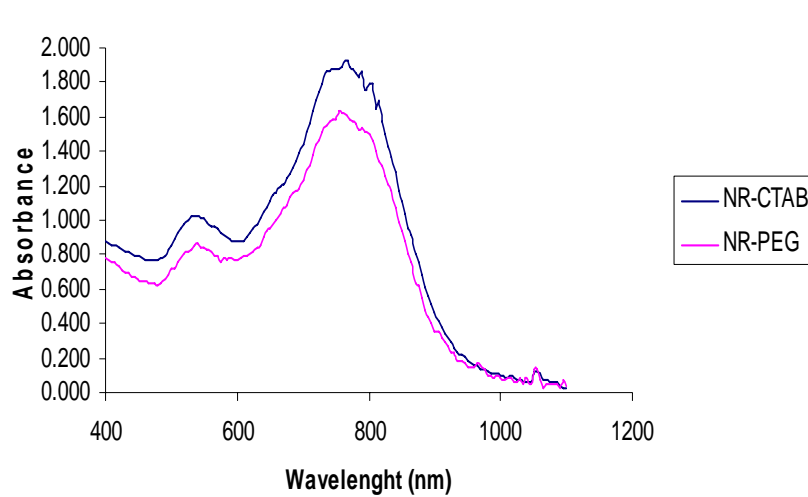


Figure 33: Absorption spectra of CTAB-coated and PEG-coated GNRs as fabricated in our lab.

- Intravenous injection of PEGylated GNRs with approximate dimensions of 11x65 nm yielded a half-life of 6 to 12 hours in mice (104). Blood circulates in the body approximately once per minute; thus a half-life of 6 to 12 hours seems sufficient for injected particles to circulate within the body more than 360 times before they are cleared from the blood stream (6 hours equals 360 minutes).
- To enhance the specificity, one would need to functionalize nanoparticles in a way that they selectively bind to cancer cells without affecting normal surrounding tissue. Her2/neu is a well-known tumor-associated biomarker that is over-expressed in many breast cancer cells, especially in metastatic tumors. This marker is abundant on the surface of breast cancer cells, is not expressed by normal cells, and is not released into the blood stream as free protein, and a monoclonal antibody is available in the market for it.

Based on the above parameters and also additional technical considerations regarding making gold nanoparticles, we proposed using gold nanoparticles with an approximate size of 15x50 nm in this dissertation. Then, these nanoparticles were functionalized using monoclonal antibody Herceptin to bind to the Her2/neu receptor on the surface of cancer cells to enhance the light absorption of targeted cells in the near-infrared region of the spectrum. Finally, targeted cancer cells were detected/imaged using the optoacoustic technique.

Hydrophobic interaction between nanoparticles will generate attraction force that will lead to particle aggregation, while their similar electric charges induce repulsion forces to prevent aggregation. Repulsion forces could be expressed as zeta potential,

which basically is an indicative of the electrostatic forces on the surface of particles. Zeta potential of a solution of particle is dependent on both the surface charge of particles and the ionic strength of the solution in which the particles are suspended. In a stable colloidal solution, there is a balance between attraction and repulsion forces; this balance does not allow particles to get too close to each other to aggregate. By increasing the concentration of salts in the solution, the zeta potential will be decreased and thus the hydrophobic interactions will dominate, resulting in nanoparticle aggregation.

One of the ways to prevent particles from aggregation in the presence of salts is to coat them with polyelectrolytes that provide a strong electrostatic repulsive force even in the presence of a high concentration of ionic strength in the solution. Examples of these types of polyelectrolytes are polyacrylic acid (PAA) and polystyrenesulfonate (PSS). Both PAA and PSS are negatively charged polymers (see figure 34). The approximate length of a molecule of PAA with a molecular weight of 20,000 Da is 15 nm (120). Note that these polyelectrolytes require a low concentration of salt, usually 1 mM of NaCl, to fold properly (121). Following PSS coating of GNRs, their zeta potential drops from +30 mV (due to the presence of positively charged CTAB on their surface) to -90 mV (114); this strong negative charge is capable of producing sufficient repulsion force to prevent particles from aggregation. As a result, PSS-coated GNRs remain stable even when they are mixed with plasma proteins and ions and thus they can be used for *in vivo* experiments.

PSS-coating is superior to PAA-coating because PSS maintains its negative charge even at a low pH, whereas PAA accepts H^+ and loses its negative charge at acidic pH and thus may not be able to provide sufficient repelling force to prevent aggregation at a low pH (105). For instance, Zeta potential of PSS-coated nanoparticles is reported to be around -50 mV, while that of PAA-coated is only -20 mV at a pH of 5.5. As

mentioned before in this dissertation, particle aggregation can be monitored by looking at the absorption pattern of gold solution, as aggregation will dramatically affect plasmon resonance and peak absorption of nanoparticles. This can be seen even by naked eyes: when 100 μL of PBS is added to 1 mL of a solution of unconjugated gold nanospheres in a tube, the red color of the solution, that represents strong green light absorption due to plasmon resonance, changes to blue almost instantly.

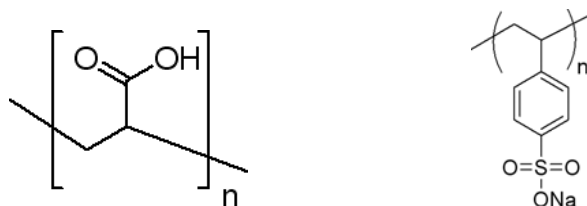


Figure 34: Chemical structure of polyacrylic acid (PAA, left) and polystyrenesulfonate (PSS, right). The negative charge of PAA is due to the presence of multiple carboxylic acid functional groups, while that of PSS is due to sulfonate groups. Structures are taken from www.sigmaaldrich.com.

Free sulfhydryl group reacts with gold surface to make a dative bond, also known as a coordinate covalent bond. In dative bond, two electrons are shared from a single atom; in our case, both electrons that are shared between gold and sulfhydryl group come from sulfhydryl side. This is in contrast to a conventional covalent bond in which each side of the bond should bring one electron to share. Dative bond is very strong and stable; thus the attachment of antibodies to gold nanoparticle through their sulfhydryl side chains is also very stable.

4.5 FABRICATING FUNCTIONALIZED GNRs

As described previously, a stable covalent bond between gold nanoparticles and antibodies is required to prevent the dissociation of antibodies from gold nanoparticles *in vivo*. The details of the conjugation of spherical gold nanoparticles to Herceptin were described before. Unfortunately, the same approach cannot be used for the covalent attachment of antibodies to GNRs because the chemical behavior of GNRs is different from that of spherical gold nanoparticles. To fabricate a stable bioconjugate of GNRs, at least two differences between GNRs and spherical gold nanoparticles need to be addressed:

- Crystal structure of GNRs is different from that of spherical gold nanoparticles.
- Spherical gold nanoparticles are stabilized using citrate that is a water-soluble molecule. In contrast, GNRs are stabilized using a high concentration of CTAB that is a surfactant. CTAB produces a protecting lipid bilayer around GNRs and prevents water-soluble molecules from reaching the surface of gold nanoparticles. Removing CTAB requires heating of nanoparticles to a temperature of 200°C or higher (109).

As mentioned previously, GNRs were stabilized with an excess amount of CTAB, which is toxic to cells. This means that these nanoparticles cannot be incubated with cells. To overcome the toxicity issue, CTAB needs to be covered or replaced by non-toxic materials while preserving the stability of nanoparticles.

One of the methods that can be used to overcome the toxicity problem is to coat gold nanoparticles with PEG (46;104). To do this, we incubated GNRs with thiol-

modified PEG with a molecular weight of 5000 Dalton at a pH of 9.5. This pH allowed thiol group to react with GNRs. After 24 hours, CTAB was removed by centrifugation and PEGylated nanorods were suspended in phosphate buffered saline (PBS).

Alternately, CTAB-stabilized GNRs were coated with PAA with a molecular weight of 15000. The details of the protocol used in this experiment is presented in Appendix B. PAA is a poly-electrolyte with a strong negative charge and thus is attracted to the surface of gold particles that are positively charged due to the presence of CTAB (120;121). PAA is suitable for nanoparticle coating due to two main reasons: it is negatively charged and thus will adhere to the positive charge of CTAB on the surface of GNRs, and it contains functional carboxylic group that can be used to bind it to other molecules of interest using standard chemistry protocols. In our lab, we first produced PAA-coated GNRs using a conventional protocol that has been published in the literature (114;121). We further improved the protocol by adding monoclonal antibody Herceptin into the structure of GNRs. After removing extra CTAB from solution, PAA-coated nanorods were conjugated to monoclonal antibody Herceptin using 1-ethyl-3-[3-(3-dimethylaminopropyl)carbodiimide hydrochloride (EDC), a bifunctional biolinker that binds the carboxylic group of PAA on one arm and the free amine groups of Herceptin using the other arm. The details of this protocol can be found in appendix B.

Fabricated gold nanoparticles were composed of GNRs with CTAB and PAA on the surface while fluorescently labeled Herceptin was conjugated to PAA. To check if these functional gold nanoparticles can target Her2/neu receptor on the surface of breast cancer cells, a series of *in vitro* experiments was performed. BT-474 cells, a breast cancer cell line that over-expresses Her2/neu receptor, and COS-7, a kidney cell line that does not over-express Her2/neu, were cultured on 24-well culture plates and were incubated with 100 μ L/ ml of a solution of fabricated gold nanoparticles at room temperature for

30 minutes. Cell plates were rinsed with PBS, and the samples were then examined under confocal microscopy using a 568 nm excitation wavelength and appropriate filter sets to detect Alexa Fluor 568. A typical image set acquired in this experiment is depicted in figure 35. In this figure, BT-474 cells are visualized brightly due to the attachment of fluorescently labeled GNRs, while COS-7 cells appear dark with a minimal non-specific fluorescent activity. This reveals the selective targeting of Her2/neu receptor on the surface of BT-474 cells by fabricated GNRs.

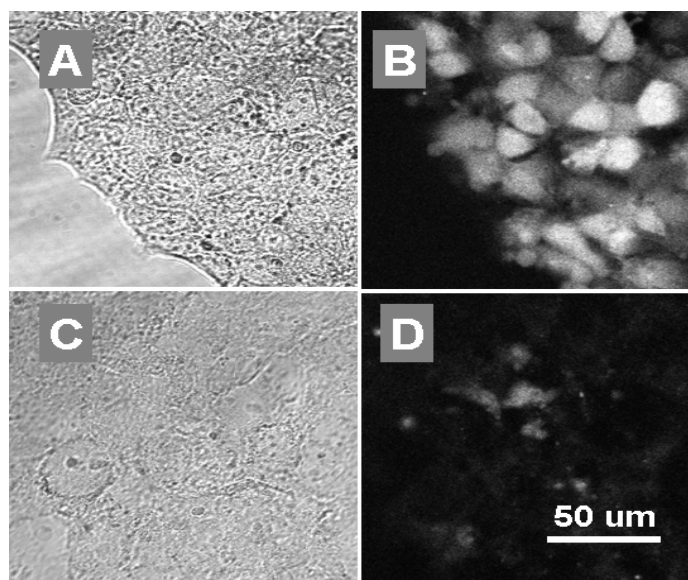


Figure 35: Bright field and fluorescent images of BT-474 (A,B) and COS-7 (C,D) cells incubated with Alexa Fluor 568-labeled Herceptin-nanorod conjugates. Images B and D were acquired with same excitation/emission parameters. These images show higher affinity of Herceptin-nanorod conjugates for BT-474 cells that over-express Her2/neu receptor.

4.6 WHY IS A COVALENT CONJUGATION OF ANTIBODY TO GOLD NANORODS REQUIRED FOR *IN VIVO* EXPERIMENTS?

While the non-covalent attachment of monoclonal antibodies to GNRs provides an excellent tool for molecular targeting of cancer cells *in vitro*, these constructs may not perform well within the *in vivo* microenvironment. For instance, it has been found that the *in vivo* microenvironment of the body interferes with the performance (i.e., stability and functionality) of gold nanoparticles (122;123). Blood is a very complex environment with materials such as hydrogen, Na, Cl, and Ca, as well as proteins, lipids, hydrocarbons, and multiple cellular components; each may affect nanoparticle stability and functionality. To minimize these effects, a covalent conjugation is required between the surface of GNRs and targeting vehicles such as monoclonal antibodies.

Successful targeting of GNRs to cancer cells *in vivo* is dependent on the ability to make them (a) stable within the *in vivo* microenvironment, (b) non-toxic and biocompatible, (c) last in the blood stream long enough to find their target, and (d) able to target cancer cells (37). To elongate their half-life in blood, GNRs should be protected against the RES (118;124). PEG has been used to improve the circulation time of nanoparticles within blood pool (118). Gold nanospheres have been successfully functionalized and used *in vivo* for tumor targeting (125); however, functionalizing GNRs for *in vivo* targeting has been a challenge mainly due to their physicochemical properties. As explained earlier in this chapter, GNRs are usually produced and stabilized using a toxic material such as CTAB (104). Furthermore, due to their unique crystal structure, their chemical behavior is also different from that of gold nanospheres (108;109;111). Together, limitations mean that novel chemical protocols are required for conjugating GNRs to biological molecules.

Covalent conjugation of antibodies to GNRs without utilizing PEG has been reported in the literature (126); however, the stability and functionality of these constructs within the *in vivo* microenvironment have not been studied. In this dissertation, a novel protocol was developed for the engineering of multi-functional GNRs to covalently conjugate GNRs with both monoclonal antibody (i.e., Herceptin) and PEG. Another interesting observation is that direct attachment of antibodies to nanoparticles may hinder the binding of antibodies. This problem has been solved by adding a theter arm between antibody and the surface of microspheres as depicted in figure 36.

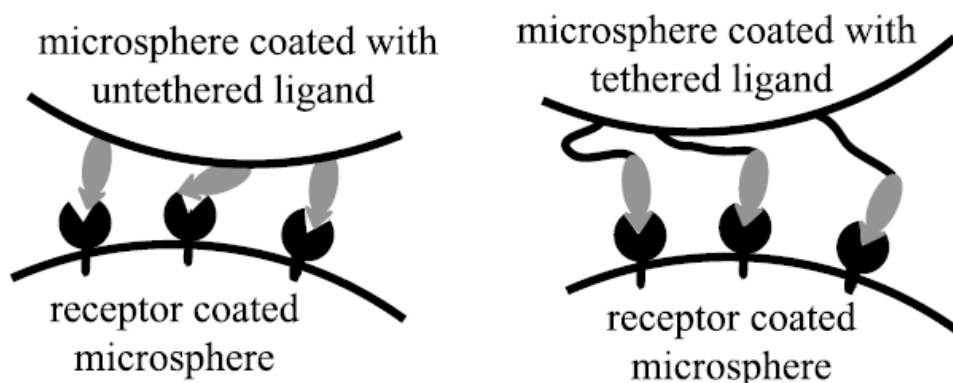


Figure 36: Direct conjugation of antibodies to microspheres (left) versus attaching antibodies to microspheres using a theter arm. It was found that the binding affinity of antibodies is preserved better when a theter molecule with a length of at least 20 angstrom has been used (127).

Thus, in this dissertation, the goal was to engineer stable GNRs that are covalently attached to monoclonal antibodies using a theter arm. As for the theter arm, we chose NanoThinks Acid 16 (#662216, 5mM in ethanol, Sigma-Aldrich, St. Louis, MO), a molecule with 16 carbons and a COOH group on one side and SH functional

group on the other side. This particular molecule was used because its length is comparable to the length of CTAB that is covering the surface of GNRs. Figure 37 shows the chemical structure of NanoThinks Acid 16 as compared to that of CTAB. The size of NanoThinks Acid 16 allows for the SH side group of the molecule to penetrate between CTAB molecules on the surface of nanoparticles to make a dative binding with gold nanoparticles, while the COOH side remains outside of the CTAB layer. This arm also functions as a theter when an antibody is conjugated to it.

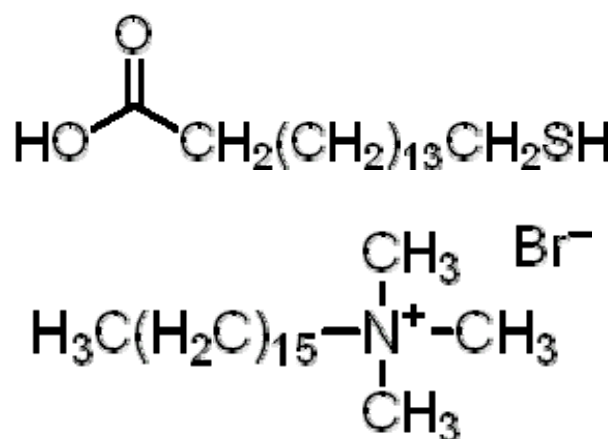


Figure 37: Chemical structure of NanoThinks Acid16 (top) and CTAB (bottom). NanoThinks Acid 16 possesses an SH group to bind to gold surface on one side and a COOH group on the other side. COOH can be used for bioconjugation. The length of NanoThinks Acid 16 is comparable to the length of CTAB that covers GNRs.

Figure 38 depict the schematics of the proposed construct. According to this protocol, GNRs with a peak absorption wavelength at 760 nm were prepared as described

earlier. Then, 1 mL of a solution of GNRs in CTAB was centrifuged twice in a 1.5 mL eppendorf tube at 10000 RPM and resuspended in 1 mL DI water. Then, 10 μ L of NanoThinks Acid 16 solution (#662216, 5mM in ethanol, Sigma-Aldrich, St. Louis, MO) was added to the gNR solution, and the solution was sonicated for 15 minutes at 50°C to prevent aggregation. The temperature was then adjusted to 30°C while sonication was continued for another 120 minutes. Next, the solution was centrifuged at 10,000 RPM for 10 minutes, supernatant removed, and pellet resuspended in PBS. EDC (1-ethyl-3-[3-imethylaminopropyl]carbodiimide hydrochloride (#77149, Pierce, Rockford, IL) and sulfo-NHS (#24520, Pierce) were added at a final concentration of 4 mM and 1 mM, respectively, and the mixture was sonicated for 25 minutes at 4°C to produce activated GNRs (i.e., GNRs that are capable of binding to the amine side chain of proteins).

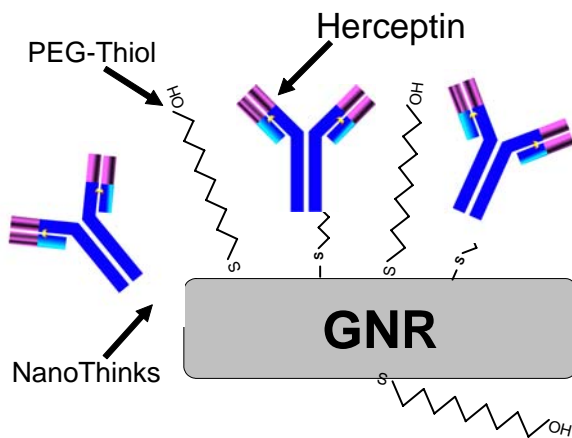


Figure 38: Schematics of Her-PEG GNRs. The particles are attached covalently to Herceptin through NanoThinks Acid 16. PEG-thiol molecules are also attached to GNRs through their thiol functional group.

Monoclonal antibody Herceptin was a kind donation from Genentech, San Francisco, CA. Purified Herceptin was then added to a final concentration of 100 $\mu\text{g/mL}$ to 1 mL of activated GNRs. The mixture was sonicated at room temperature for 2 hours. Following the removal of excess Herceptin, 10 μL of PEG-thiol (10 mM) with a molecular weight of 5000 Da (mPEG-Thiol-5000, Laysan Bio Inc., Arab, AL) was added to 1 mL of Herceptin-conjugated GNRs, and the mixture was incubated at room temperature for 2 hours. The final solution was diluted by adding PBS to achieve an optical density of 1.0 at 760 nm as measured by Cary50 spectrophotometer.

Alternatively, the initial steps involving monoclonal antibody coating were skipped in the protocol, and CTAB-coated GNRs were reacted with PEG-thiol directly to produce PEG GNRs. The optical density of the final solution was adjusted to 1.0 at 760 nm. In the next chapter, a series of experiment will be presented to investigate the stability and functionality of the manufactured nanoparticle.

4.7 DETERMINING THE PROFILE OF OPTOACOUSTIC SIGNAL GENERATED BY GNRs UPON NEAR-INFRARED LASER IRRADIATION

A disk-shaped gelatin phantom with a thickness of 40 mm was placed on a wide-band acoustic transducer (Fairway Medical Technologies, Houston, TX), and a well was produced on top of the gelatin phantom to hold 100 μL of samples. Samples of nanorod solution at different concentrations were added to the well on top of the phantom; the phantom was then irradiated with an Alexandrite laser running at 757 nm with a fluence of 6 mJ/cm^2 . Figure 39 depicts the results of this experiment for three solutions. Based on the amplitude of the signal and the noise level of the system, we calculated the minimum detectable concentration of GNRs as 7.5×10^8 NPs per mL. This is comparable to the

previously calculated minimum detectable concentration of spherical gold NPs *in vitro*, which was 10^9 NPs per mL (see figure 16).

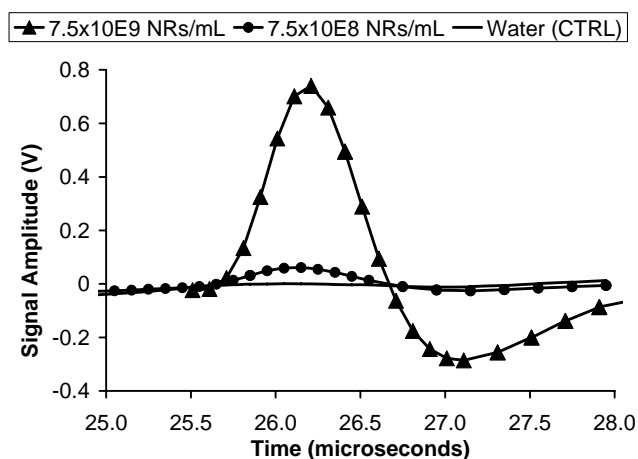


Figure 39: Optoacoustic signal generated by GNRs detected through a 4 cm-thick scattering media. GNRs were detectable at a minimum concentration of 7.5×10^8 NPs per mL (1.25 pM).

The y-axis in figure 39 is the amplitude of the optoacoustic signal in volts, and the x-axis is the time of arrival of the signal to the transducer following pulsed laser irradiation. The distance between the target and transducer was ~ 37 mm and the speed of sound was ~ 1.5 mm/ μ s. This is the reason why the signal appeared ~ 26 μ s after laser irradiation. We concluded that the following:

- 1) GNRs were detectable *in vitro* using an optoacoustic method at a minimum concentration of 7.5×10^8 NPs/mL (1.25 pM),
- 2) The amplitude of optoacoustic signal was proportional to the concentration of gold nanoparticles.

4.8 NEAR-INFRARED OAT OF TARGETED CANCER CELLS *IN VITRO*

The next experiment was aimed at enhancing optoacoustic signal from targeted cancer cells *in vitro*. To perform this experiment, 15 million BT-474 cancer cells were incubated with Herceptin-conjugated GNRs. Another 15 million cells were incubated with albumin-conjugated GNRs as a negative control. Cells were harvested and centrifuged to make two pellets that were embedded within a disk-shaped gelatin phantom as depicted in figure 40. Figure 40A shows the gelatin phantom with two embedded cell pellets: the left pellet is a pellet of BT-474 cells treated with Herceptin-conjugated GNRs and the right pellet is BT-474 cells treated with albumin-conjugated GNRs as a negative control. Figure 40B demonstrates the optoacoustic image of this phantom. As can be seen, both objects are visible in the optoacoustic images; however, the cells treated with Herceptin-conjugated nanoparticles produced a stronger signal.

There are two important observations in figure 40B. First, the targeted pellet (left pellet) is brighter than the control pellet (right pellet); the analysis of raw data showed a three times enhancement of optoacoustic signal in cells treated with Herceptin-conjugated GNRs as compared to that of albumin-conjugated GNRs. Secondly, the targeted cells on the optoacoustic image appeared larger than their actual size; this is perhaps due to the limited resolution of our optoacoustic transducer. The resolution of an optoacoustic imaging system is dependent on the time-response of its detectors, the speed of sound within the sample, and the spatial arrangement of detectors relative to the sample. The speed of sound cannot be modified in a sample; however, one may use detectors with a higher frequency response and arrange them in a circle with the object being imaged at the center to enhance the lateral and radial resolution of this imaging system.

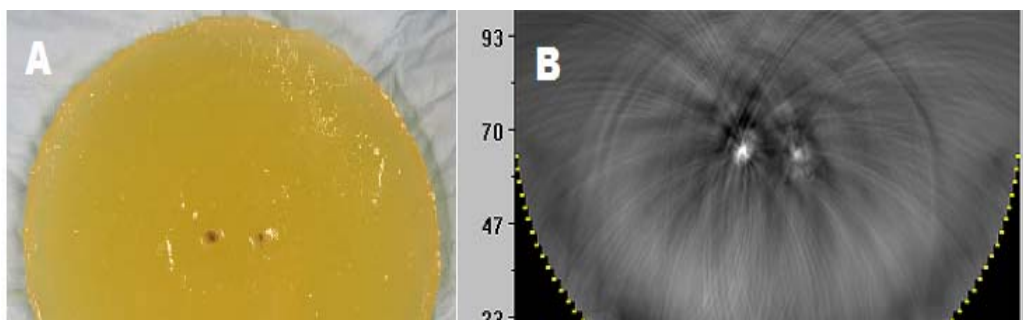


Figure 40: Optoacoustic imaging of targeted cancer cells embedded within a gelatin phantom. (A) Gelatin phantom with two embedded object made of cells treated with Herceptin-conjugated (left pellet) or albumin-conjugated (right pellet) GNRs. (B) Optoacoustic image of phantom showing both pellets. Left pellet that was treated with Herceptin-conjugated GNRs was brighter.

4.9 NEAR-INFRARED OPTOACOUSTIC DETECTION OF SUBCUTANEOUSLY INJECTED GNRs

The advantage of replacing spherical gold nanoparticles with nanorods is that it will allow one to use a near-infrared pulse laser to illuminate gold nanoparticles. Near-infrared illumination is important for *in vivo* imaging because the absorption coefficient of human breast tissue in visible light is much more than that of near-infrared light. For example, the absorption coefficient of breast tissue at 580 nm is reported to be 0.7 cm to 1, while that of 800 nm is 0.017 to 0.045 cm⁻¹ (87). This difference is important because tissues such as breast strongly attenuate light in the visible range of the spectrum, which limits the maximum illumination depth of a tissue for OAT to a few millimeters. In contrast to visible light, near-infrared penetrates several centimeters within tissue. An *in*

in vivo experiment was designed to determine if OAT could be used for single-point detection of subcutaneously injected PEGylated nanorods in nude mice.

Figure 41 depicts the schematics of an experiment in which a sedated nude mouse was placed in a supine position (face up) on top of a single-channel optoacoustic transducer. An Alexandrite laser was used to generate a laser beam to illuminate the abdomen of the mouse so that it was irradiated from the front while the optoacoustic signal was detected from the back. Initially, a control optoacoustic signal was recorded. Then, 50 μL of a solution of PEGylated GNRs at a concentration of 7.5×10^9 GNRs per mL (12.5 μM) was injected subcutaneously into the abdominal area of the mouse, with the generated optoacoustic signal then recorded from the back. The optoacoustic signal profiles are shown in Figure 42.

Figure 42 demonstrates that a concentration of 7.5×10^9 NP/mL generates detectable optoacoustic signal over the background *in vivo*. This concentration is equivalent to having one single nanoparticles in each 1.33×10^{-16} m^3 . Assuming an average size of $20 \times 20 \times 20$ μm for a cancer cell, the volume of each cancer cell would be 8×10^{-15} m^3 . This means that to achieve a detectable concentration of gold nanoparticles *in vivo* (i.e. 7.5×10^9 NP/mL), one would need to target an average of 60 NP to each cancer cell. This number seems to be promising considering the fact that the copy number of Her2/neu on the surface of cancer cells are reported to be as high as 926000 per cell (33).

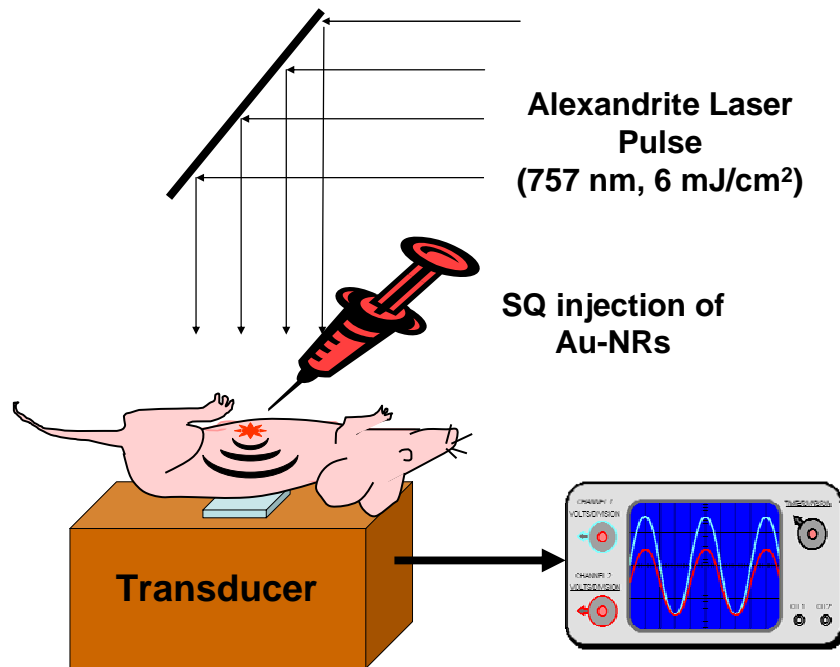


Figure 41: Schematics of *in vivo* optoacoustic detection of subcutaneously (SQ) injected GNRs (GNRs). A single-channel acoustic transducer was used in this experiment. GNRs were injected subcutaneously to ventral side of abdomen, and optoacoustic signal was detected from dorsal side. Sedation was used to minimize motion artifact.

The experiment was repeated using another mouse with similar setups as described before. In the second experiment, the signal enhancement was noted upon subcutaneous injection of GNRs at 18.5 μs post laser irradiation (Figure 43). This time delay is different from the previous experiment simply because the size of the mouse that was used in this experiment was different from the previous one. Considering the speed of sound in tissue ($\sim 1.5 \text{ mm}/\mu\text{s}$) and the fact that in the second experiment the generated signal had to travel through the mouse abdomen (approximate thickness of 2.5 cm) to reach the transducer, a time delay of 18.5 μs was expected. This experiment shows that

the optoacoustic method can be used for the single-point detection of GNRs through a tissue with a thickness of a few centimeters.

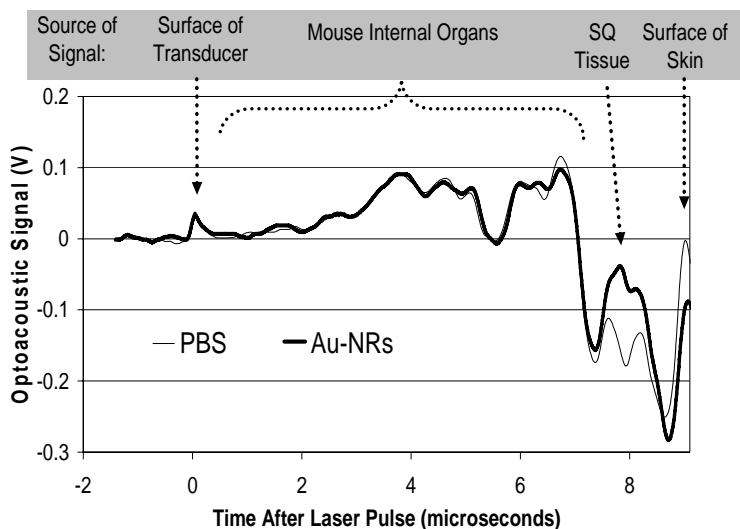


Figure 42: *In vivo* detection of subcutaneously injected GNRs in nude mouse. GNRs (25 μ L at a concentration of 1.25 pM) or PBS (25 μ L) was injected subcutaneously into the ventral abdominal area of the mouse, and the generated optoacoustic signal upon laser pulse irradiation was detected via a transducer placed on the back of the mouse. X-axis represents the time of arrival of signal in microseconds as compared to the surface of transducer. The signal originating from injected GNRs arrived at 8 μ s, which corresponds to a distance of 12 mm from the surface of transducer. GNRs enhanced the amplitude of optoacoustic signal by increasing local light absorption.

To further demonstrate the capability of OAT to generate an image of the distribution of PEGylated GNRs *in vivo*, another experiment was designed to image a nude mouse before and after subcutaneous injection of GNRs. To perform this experiment, a custom optoacoustic imaging system was designed and assembled at Fairway Medical Technologies, Houston, TX (see figures 44, 45). The imaging system used in this experiment was composed of two parallel linear arrays of 32 acoustic

transducers equipped with a real-time multichannel signal processing that provided a gain of over 30 dB and a noise level less than 2 mV for acoustic detection. A nude mouse was anesthetized as described previously and was placed between two linear probes (transducer arrays); the laser irradiation was then delivered orthogonally to the image plane. The Alexandrite laser was used to irradiate the whole body of the mouse with a fluence of 2 mJ/cm². After capturing a control image, 100 μ L of a solution of PEGylated GNRs at a concentration of 7.5×10^{10} NRs per mL was injected subcutaneously into the abdominal area of a nude mouse, and optoacoustic images were captured. Figure 46 depicts the result of this experiment.

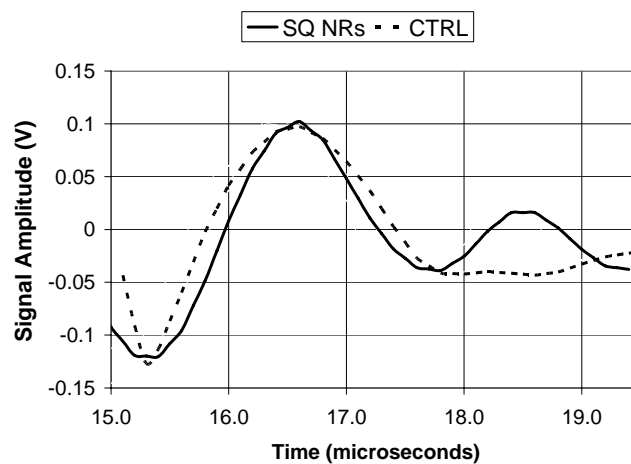


Figure 43: Optoacoustic signal generated following subcutaneous injection of 50 μ L of GNRs at a concentration of 12.5 pM into the abdominal area of a nude mouse. Time zero corresponds to the time of laser pulse irradiation. The difference between the amplitude of the signal at 18.5 μ s represents injected GNRs.

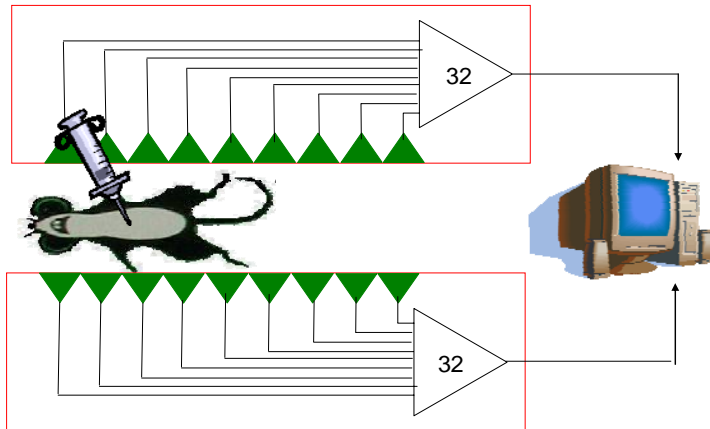


Figure 44: Schematics of optoacoustic detection of GNRs following subcutaneous injection into nude mice.

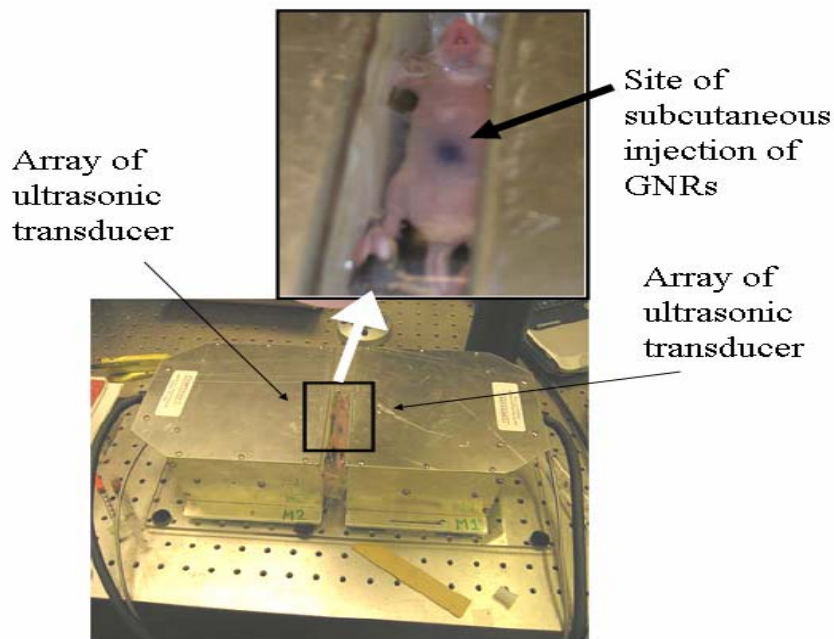


Figure 45: Setup of the experiment for optoacoustic imaging of nude mice injected with GNRs. Two parallel arrays of transducers were holding the mouse from sides. Laser irradiation was applied from top.

Figure 46a shows the OAT of the nude mouse before injection of GNRs. The body of the mouse was hardly visible in the optoacoustic image due to the low ultrasound frequency cut-off in our imaging system, and thus an overlay drawing is added to figure 46A to illustrate the approximate position of the animal during this experiment. The approximate site of injection of GNRs is also demonstrated in this figure. Figure 46B was acquired after subcutaneous injection of GNRs. This figure shows the appearance of a bright white object that represents the enhancement of optoacoustic signal in the area that GNRs were injected. The injected GNRs were brightly visible in the optoacoustic image, while the body of the mouse was almost invisible. This is due to the presence of the high contrast between normal tissue and GNRs under OAT. This experiment successfully demonstrated the feasibility of using optoacoustic method to image GNRs *in vivo*.

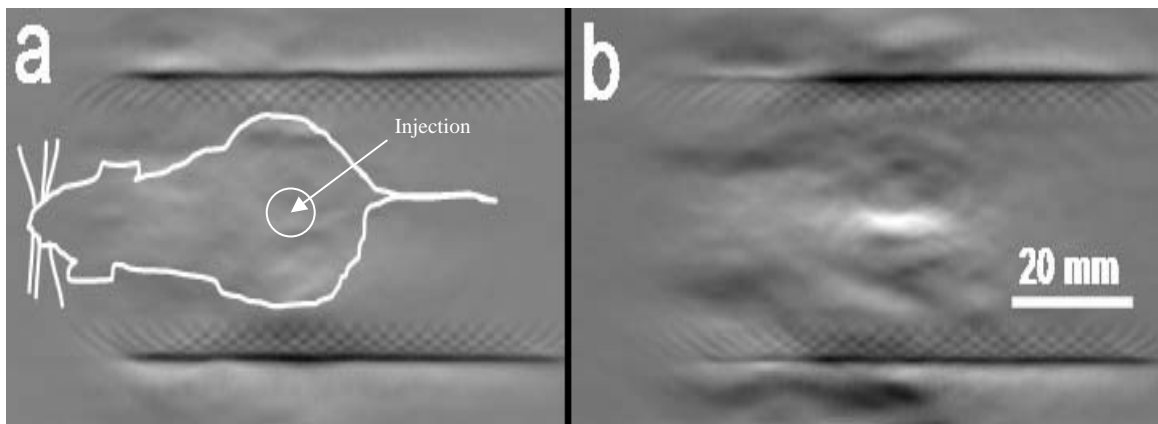


Figure 46: Optoacoustic image of a nude mouse before (a) and after (b) injection of GNRs. 100 μL of GNRs at a concentration of 7.5×10^{10} NRs per mL was injected into the subcutaneous area in the ventral abdominal. Injected gold nanoparticles are visible in the optoacoustic image (b) as a bright object. Drawing in (a) depicts the approximate layout of the nude mouse.

Recently, a special acoustic transducer has been designed and assembled at Fairway Medical technologies, Houston, Texas for three dimensional optoacoustic imaging of small animals. This transducer is an array of 64 of 2x2 mm piezocomposite transducers that are positioned on an arc of 154 degrees with a radius of 65 mm. The transducer bandwidth was determined to be 1.2 MHz with a center of 3.0 MHz. Figure 47a demonstrates the schematics of the experiment that was performed using this transducer along with two of the sample images that were acquired using a nude mouse (courtesy of Fairway Medical Technologies).

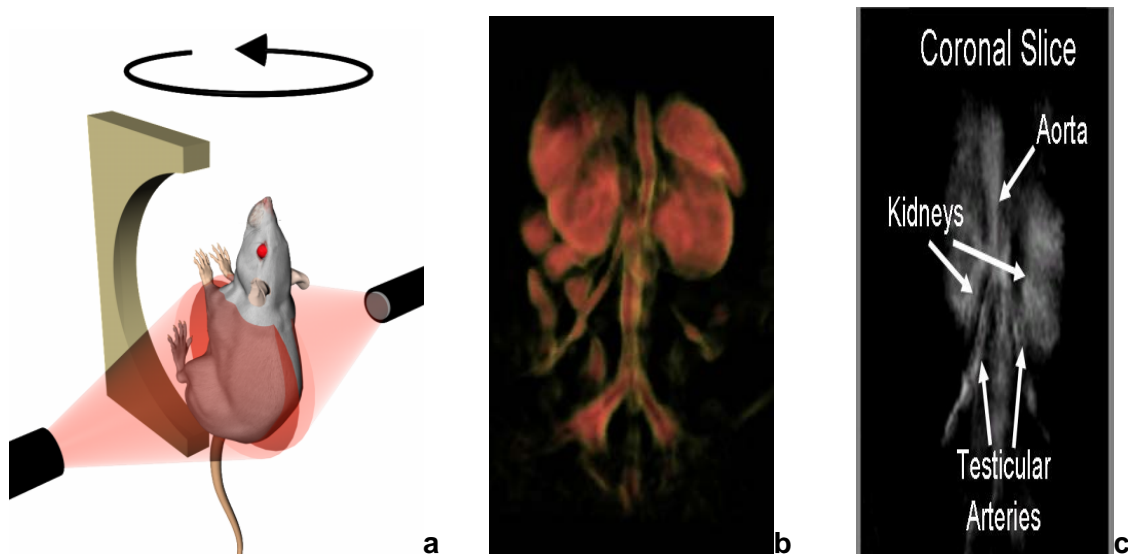


Figure 47: Schematics of OAT rotational system using arc-shaped array of ultrasonic transducers (a), 3D image of a live mouse showing internal organs, an artery running from mouse head through the body and bifurcated to its legs (b), 2D coronal slices through 3D optoacoustic volume (c). Courtesy of Fairway Medical Technologies.

In a typical experiment that is presented in figure 47, a nude mouse was anesthetized using inhalation of isoflurane and was positioned on a rotating stage in a water tank that contained acoustic transducer. Arc-shape array of acoustic transducer was

composed of 64 elements of piezoelectric material with dimensions of 2x2 mm and a bandwidth of 3 ± 1.2 MHz. The mouse was rotated 360 degree while its body was illuminated with a pulsed Alexandrite laser running at 757 nm with an optical fluence of 3.5 mJ/cm^2 . Optoacoustic signal was recorded for 150 steps of rotation to cover 360 degrees. Recorded signal was exported to custom image reconstruction software to generate images. Figure 47b and 47c show typical reconstructed images that show the internal organs of the mouse including. These experiments demonstrate the feasibility of using optoacoustic imaging for non-invasive imaging of small animals.

4.10 SUMMARY

The rationale for using gold nanorods but not gold nanospheres for in vivo OAT was discussed. The protocols for making gold nanorods with optimized chemico-physical properties were presented. Gold nanorods were functionalized using different method and a novel method for the covalent conjugation of monoclonal antibodies to GNRs was developed. The feasibility of imaging gold nanorods in vivo using OAT with a pulsed infrared light source and an array of optoacoustic transducers have been demonstrated here.

Chapter 5: Determine the Biocompatibility, Stability, Biodistribution, and Selective Tumor Targeting of Fabricated Gold Nanoparticles

In this chapter, a series of experiments to improve the biocompatibility of fabricated gold nanoparticles are presented. As mentioned previously, PEGylation has been used as a means to hide injected nanoparticles from the body's RES. Laser safety issues, to the extent that they are related to OAT, are also discussed in this chapter.

5.1 FUNCTIONALIZING GOLD NANOPARTICLES TO ENHANCE THEIR BIOCOMPATIBILITY

Although several types of injectable nanoparticles are in clinical trials for different applications, little is known about the details of interaction between the body and injected nanoparticles. The interactions include clearance, biodistribution, selective accumulation of injected particles in the body, and short- and long-term effects of injected particles on the body. The body's reaction is highly dependent on the type and size of injected nanoparticle; thus, it is required to determine these interactions individually for each type of gold nanoparticle. A series of experiments were designed and conducted to address some of the most important elements of these interactions.

To determine the toxicity of fabricated GNRs *in vitro*, three cell lines, SK-BR3 and BT-474 (human breast cancer cell lines) and Hep-G2 (human hepatocellular carcinoma cell line), were cultured on 24-well culture plates overnight and were incubated with 0.2 nM of different types of GNRs. GNRs in the form of CTAB-coated, PEG-coated, and (Herceptin+PEG)-coated were used in this experiment. After 24 hours of incubation at 37°C and 10% CO₂, the number of viable and dead cells was determined using trypan-blue staining method. Figure 48 depicts the results of this experiment in

which the toxicity of CTAB-coated GNRs were reflected by an increase in the percentile of dead cells. In contrast, PEG- and (HER+PEG)-coated GNRs show little or no toxicity as compared with the control group, which was not incubated with any types of GNRs. These results confirm previously reported data on toxicity of CTAB-coated GNRs and confirm that our fabricated particles are well-tolerated by cells.

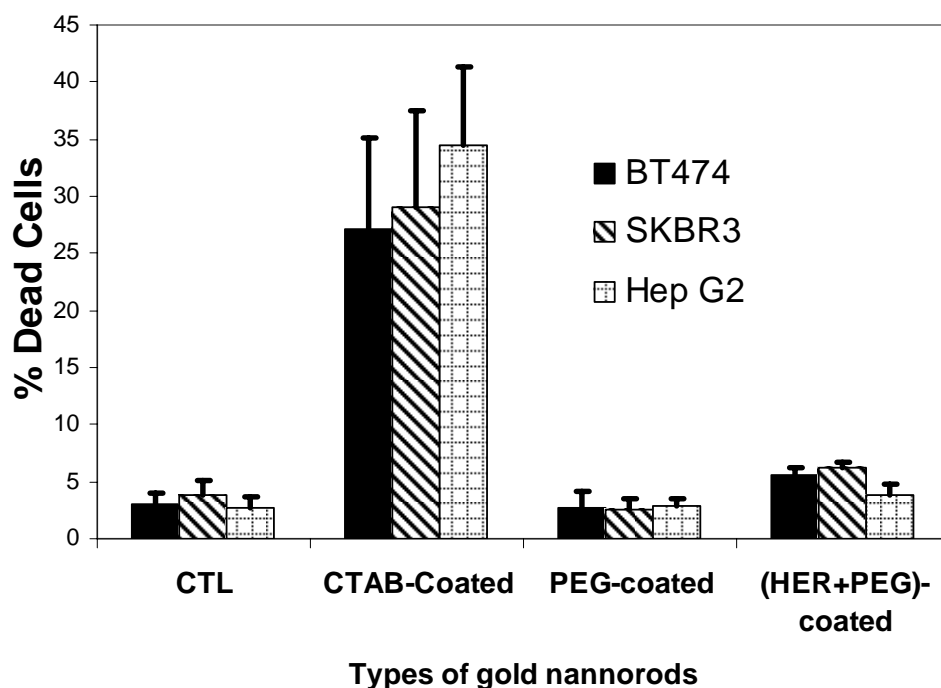


Figure 48: Toxicity assessment of different types of GNRs on three cell lines. Cells were incubated with gold nanoparticles for 24 hours in vitro and the number of dead cells were determined using trypan-blue staining method. While CTAB-coated GNRs demonstrated a significant toxicity, PEG- and (HER+PEG)-coated GNRs appear to be well-tolerated by cells. CTRL group cells were treated with PBS. Bars indicate the standard deviation of the data.

5.2 SELECTIVE TARGETING OF FUNCTIONALIZED GNRs TO CANCER CELLS *IN VITRO*

Next, we wanted to check if Her-PEG GNRs selectively bind to HER2/neu receptor on the surface of breast cancer cells *in vitro*. To do this, four human cell lines were selected: 1) lung fibroblasts, 2) MCF-7, 3) SK-BR3, and 4) BT-474. The latter three cell lines are human breast cancer cells; however, MCF-7 and lung fibroblasts do not over-express HER2/neu (128), while SK-BR3 and BT-474 cell lines do. The cells were cultured on glass cover-slips in 12-well culture plates. Unattached cells were rinsed with Roswell Park Memorial Institute culture media (RPMI). Then, 1.6 mL of fresh culture media that was mixed with 0.4 mL of PEG GNRs or Her-PEG GNRs was added to each well. Culture plates were incubated at room temperature for 45 minutes to allow nanoparticles to interact with HER2/neu receptors. Then, unattached particles were removed by rinsing the plates using PBS twice. All samples were stained using silver enhancement staining kit (Artisan Grocott's Methenamine Silver Kit; catalog # AR176; Dako; Carpinteria, CA) as recommended by the manufacturer, and the slides were examined using an Olympus Model IX70 microscope equipped with 40X and 100X objective lenses and a Spot RT Slider digital camera (Diagnostics Instruments Inc, Sterling Heights, MI).

Figure 49 demonstrates a typical image set that we acquired in this experiment, in which GNRs are visualized as dark spots around SK-BR3 (C) and BT-474 cells (D) that over-express HER2/neu receptors, but not around MCF-7 (A) or fibroblast (B) cells. The latter two cells do not express detectable HER2/neu and thus did not interact with

functionalized GNRs. The number of dark spots in each acquired image was determined manually by employing cell counter plugins that is available for Image J software. Image J software and its plug-ins were downloaded from the website of National Institute of Health (129).

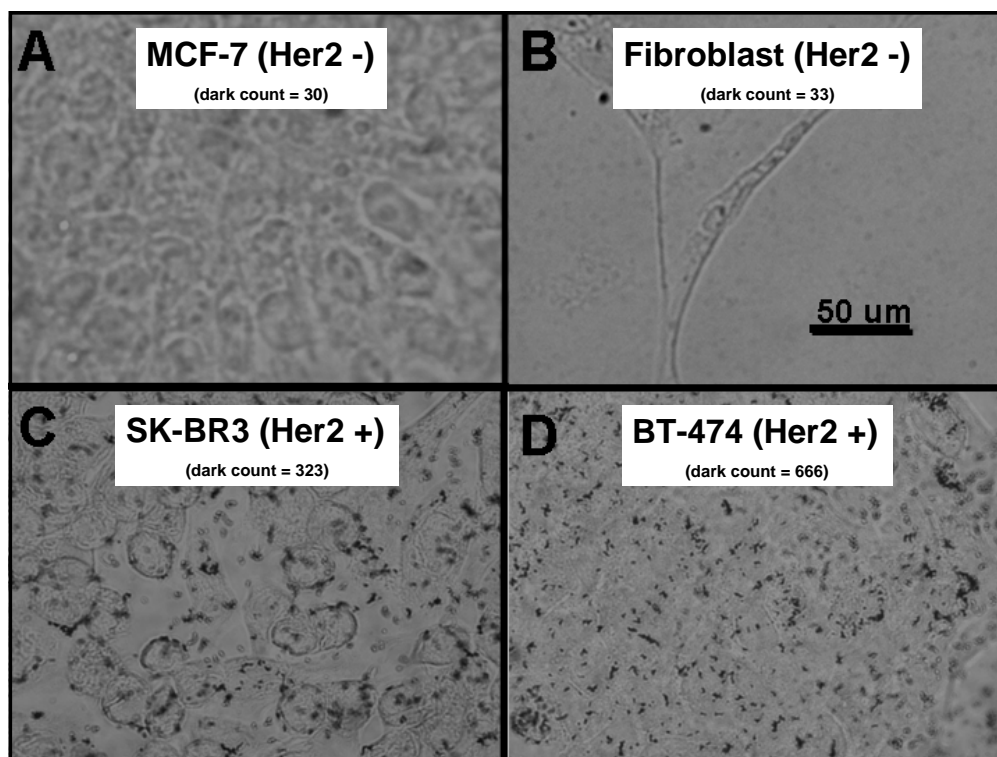


Figure 49: Silver-enhanced images of four cell lines incubated with Her-PEG GNRs *in vitro*. MCF-7 (A) and fibroblasts (B) do not express Her2/neu and thus do not interact with GNRs. GNRs appear as dark spots around SK-BR3 (C) and BT-474 (D), cells that overexpress Her2/neu receptor.

In the next experiment, we wanted to prove that the specific binding of functionalized GNRs are due to the presence of Herceptin. To do this, we incubated SK-BR3 cells with both PEG GNRs and Her-PEG GNRs in 24-well culture plates as

described previously, and stained the slides using silver-staining method. The slides were examined under bright field microscopy as described previously to identify GNRs. Figure 50 demonstrates the results of this experiment. Minimal non-specific binding of PEG GNRs to SK-BR3 cells are noted as a few dark spots around SK-BR3 cells in figure 50A; however, many dark spots are seen when Her-PEG GNRs were incubated with SK-BR3 cells, as depicted in figure 50B. This proves that the selective binding of functionalized GNRs to Her2/neu receptor is remarkably higher than the non-specific binding.

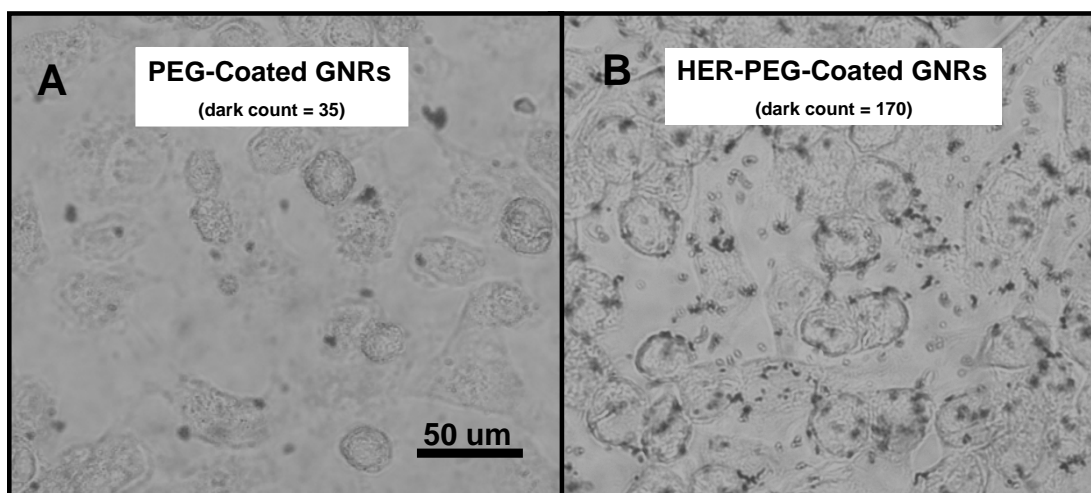


Figure 50: Bright field microscopic images of SK-BR3 cells that were incubated with PEG GNRs (A) or Her-PEG GNRs (B) *in vitro*. GNRs are visualized as dark spots after being stained with silver-enhancing method. Specific binding of HER-PEG-coated GNRs to SK-BR3 is demonstrated by a higher number of dark spots in the right image as compared to when PEG-coated GNRs were used (left).

5.3 DETERMINING THE STABILITY OF FUNCTIONALIZED GNRs WITHIN THE BLOOD MICROENVIRONMENT

As the ultimate goal of this dissertation is to make functionalized GNRs that can be injected intravenously into subjects, we sought to use the next experiment to determine if the microenvironment of blood can interfere with the stability of fabricated gold nanoparticles. This is an important issue because blood is a very complex tissue and many of its compounds could interfere with the proper functioning of injected nanoparticles (122;123). It is worth determining the stability of injected particles *in vivo*; however, such an experiment is technically a challenge. Instead, data are available to show that the composition of blood such as the pH and the concentration of critical ions such as potassium, sodium, and chloride do not change significantly if blood is preserved at the proper environment *ex-vivo* (130;131). Details of the protocols needed to preserve blood *ex-vivo* can be found in blood bank literature.

This means that an alternate method to test the stability of GNRs would be to run an *ex-vivo* experiment using preserved blood. Thus, an experiment was conducted to assess if Her-PEG GNRs remain stable and functional when incubated with blood *ex-vivo*. Samples of blood were drawn from mice, and heparin was added at a final concentration of 10 units/mL to prevent coagulation. To each mL of heparinized mouse blood was added 100 μ L of either CTAB-, PEG, or Her-PEG-coated GNRs. The samples were mixed vigorously and incubated at room temperature for four hours. Then, samples were transferred to 1.5 mL eppendorf tubes and centrifuged at 2000 RPM for 15 minutes to precipitate red blood cells (RBCs). Supernatant solution, which contained GNRs but

no RBCs, was collected and transferred to 1 cm cuvette. The light absorption of these samples was determined using a Cary50 spectrophotometer (Varian Instruments, Walnut Creek, CA). Figure 51 depicts the light-absorption spectra of these three samples.

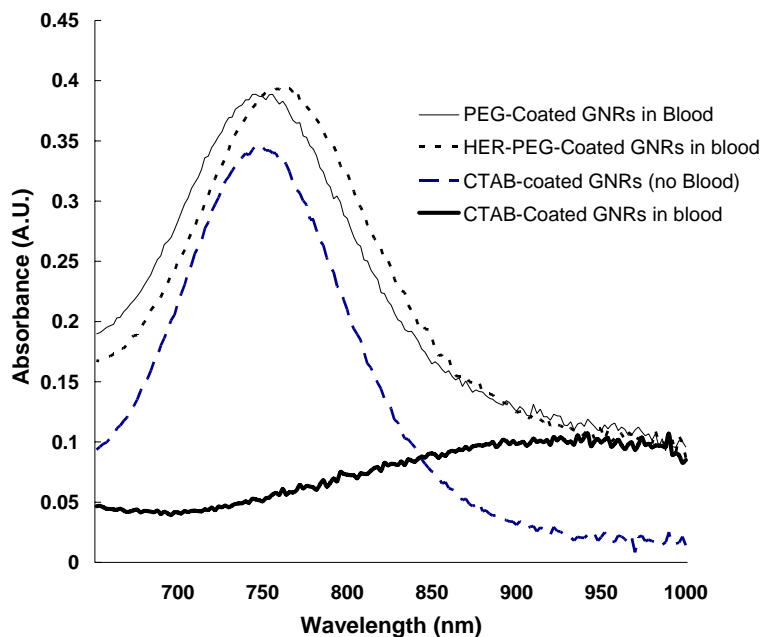


Figure 51: Absorption spectra of mouse serum after mouse blood has been incubated with three types of GNRs for three hours *ex-vivo*. The peak absorption around 760 nm disappeared for CTAB-coated GNRs, which indicates their aggregation. Preserved peak absorption at 760 nm for functionalized particles suggests the stability of these particles within the blood microenvironment.

As predicted, CTAB-coated GNRs aggregated when mixed with blood due to the high concentration of ions, and thus their peak absorption that was initially located at 760 nm disappeared. On the other hand, our functionalized GNRs that included PEG and Her-PEG GNRs did not aggregate when mixed with mouse blood, and thus their peak absorption around 760 nm remained intact. This is a very exciting result, as it confirms

that our functionalized gold nanoparticles remain stable within blood microenvironment *ex-vivo*. Based on the assumption that the composition of the blood remains relatively stable in this setting, which is supported by literature, we expect our functionalized nanoparticles to remain stable when they are injected intravenously into live subjects.

5.4 DETERMINE THE FUNCTIONALITY OF GNRs WITHIN THE BLOOD MICROENVIRONMENT

After confirming the stability of functionalized GNRs within the blood microenvironment, we wanted to see if the particles remain functional when they are mixed with blood. Mixing gold nanoparticles with blood *ex-vivo* simulates the condition that these nanoparticles will face upon intravenous injection. To test the functionality of gold nanoparticles, Her-PEG GNRs were incubated with mouse blood as described previously for four hours and then the mixture was added to BT-474 and fibroblast cells that were previously cultured on glass cover slips. After 45 minutes of incubation at 37°C, plates were rinsed using PBS to wash out unattached GNRs. These samples were stained using silver-enhancement kit as described previously. Figure 52 demonstrates the results of this experiment. In this figure, dark spots on BT-474 cells represent targeted GNRs, while only a few dots are visualized on fibroblasts. This finding confirms the selective targeting of functionalized GNRs to Her2/neu over-expressing cell line BT-474 even after these nanoparticles have been incubated with blood.

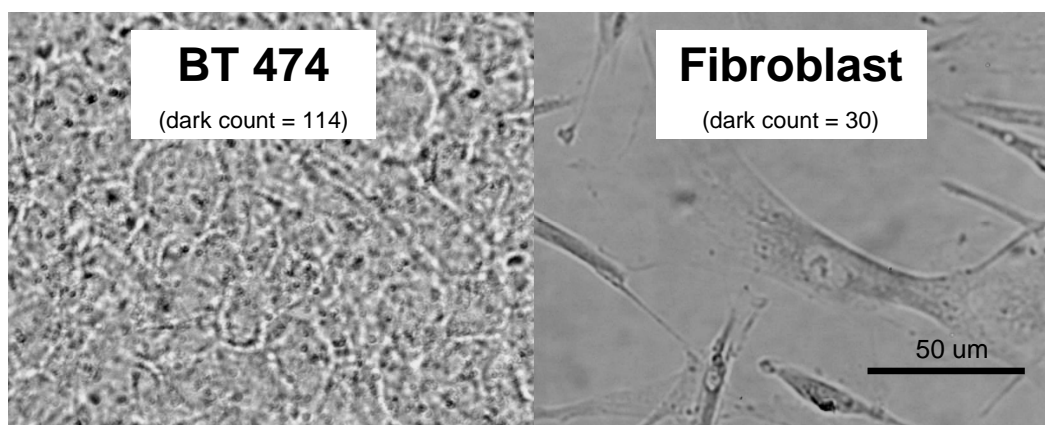


Figure 52: Bright field microscopy images of silver-stained BT-474 and fibroblast cells treated with Her-PEG GNRs. Nanoparticles were premixed with mouse blood for four hours to simulate intravenous injection. Dark spots reveal GNRs.

5.5 DETERMINING THE BIODISTRIBUTION OF FUNCTIONALIZED GNRs UPON INTRAVENOUS INJECTION INTO MICE

The final group of experiments was designed to evaluate the biodistribution of Her-PEG GNRs and determine if they accumulate within tumors that over-express HER2/neu receptor in animal models. Animal protocols were reviewed and authorized by the institutional animal care and use committee (IACUC) at the University of Texas Medical Branch. A group of 4 to 5 week old female Hsd:athymic Nude-Foxn1^{nu}/Foxn1⁺ mice were obtained from Harlan National (www.harlan.com). Typically, 2×10^6 BT-474 cells were implanted subcutaneously in the flank area of nude mice to grow tumor. To enhance tumor growth, a pellet of 0.72 mg17-beta estradiol (60-day release, Innovative Research of America, Sarasota, FL) was also implanted under the skin in the shoulder area of these mice one day prior to the tumor-cell injection. After 3 to 6 weeks, a total of twelve nude mice developed tumors with diameter in the range of 2 to 6 mm. Of these, six animals were injected intravenously with 100 μ L of Her-PEG GNRs through their tail

vein. 100 μ L of PEG GNRs was injected intravenously into the tail vein of a total of five animals. One mouse was enrolled as control, and thus 100 μ L of PBS was injected to its tail vein. After 24 hours, mice were sacrificed and samples of tumor, spleen, and kidney were obtained and preserved in formalin 4% to be fixed; the samples were then cut in slices using microtome and stained using silver-stain method as described previously to visualize GNRs under bright field microscopy as well as via conventional hematoxylin and eosin staining method (H&E). Figure 53 shows a typical set of the result of this experiment in which PEG GNRs were injected intravenously into tumor-bearing mice and the samples were stained using silver-enhanced method. In this figure, dark spots are visualized within different organs such as brain, kidney, and tumor; however, the darker appearance of slides obtained from tumor suggests that gold nanoparticles had a better chance to accumulate within tumor as compared to other tissues. This finding is in agreement with the literature, where non-specific accumulation of nanoparticles within tumors have been shown as a result of their leaky microvasculature (4).

Figure 54 depict another group of images that were captured during biodistribution experiments. These series of images also demonstrate the accumulation of HER-PEG GNRs within different organs; however, the accumulation within tumor is more prominent based on the darker appearance of the slides upon silver-enhanced staining. Note that the two bottom images in figure 54 demonstrate tissue slices that were obtained from mice injected with PBS and were used as negative control for this experiment.

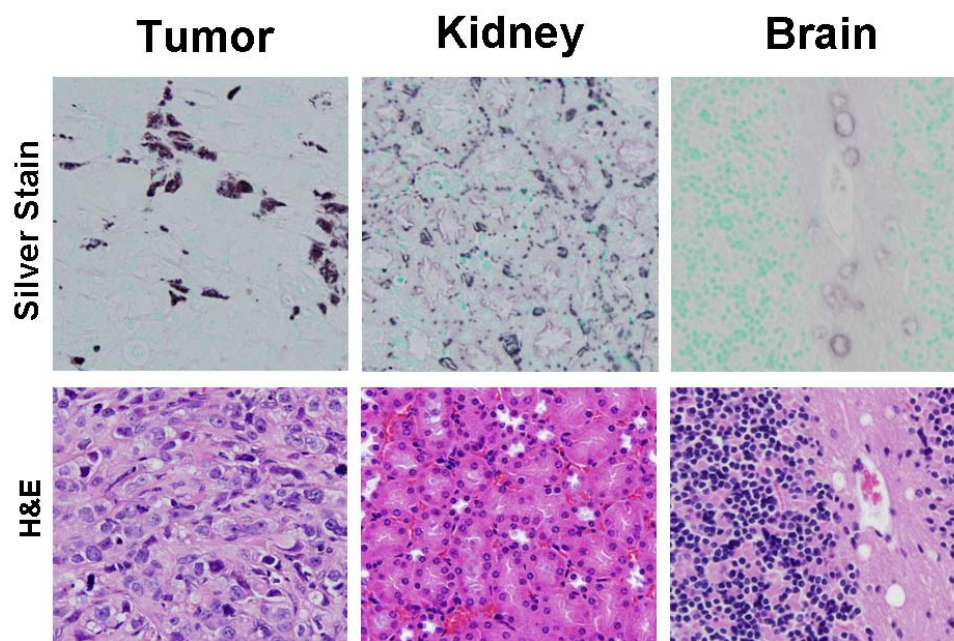


Figure 53: Silver staining (top row) and H&E staining (bottom row) of mouse tissue slices following intravenous injection of GNRs. 100 μ L of PEG GNRs at a concentration of 7.5×10^{10} GNRs/mL was injected through tail vein. Dark spots in the top row demonstrate the accumulation of gold nanoparticles within different tissue especially within tumor.

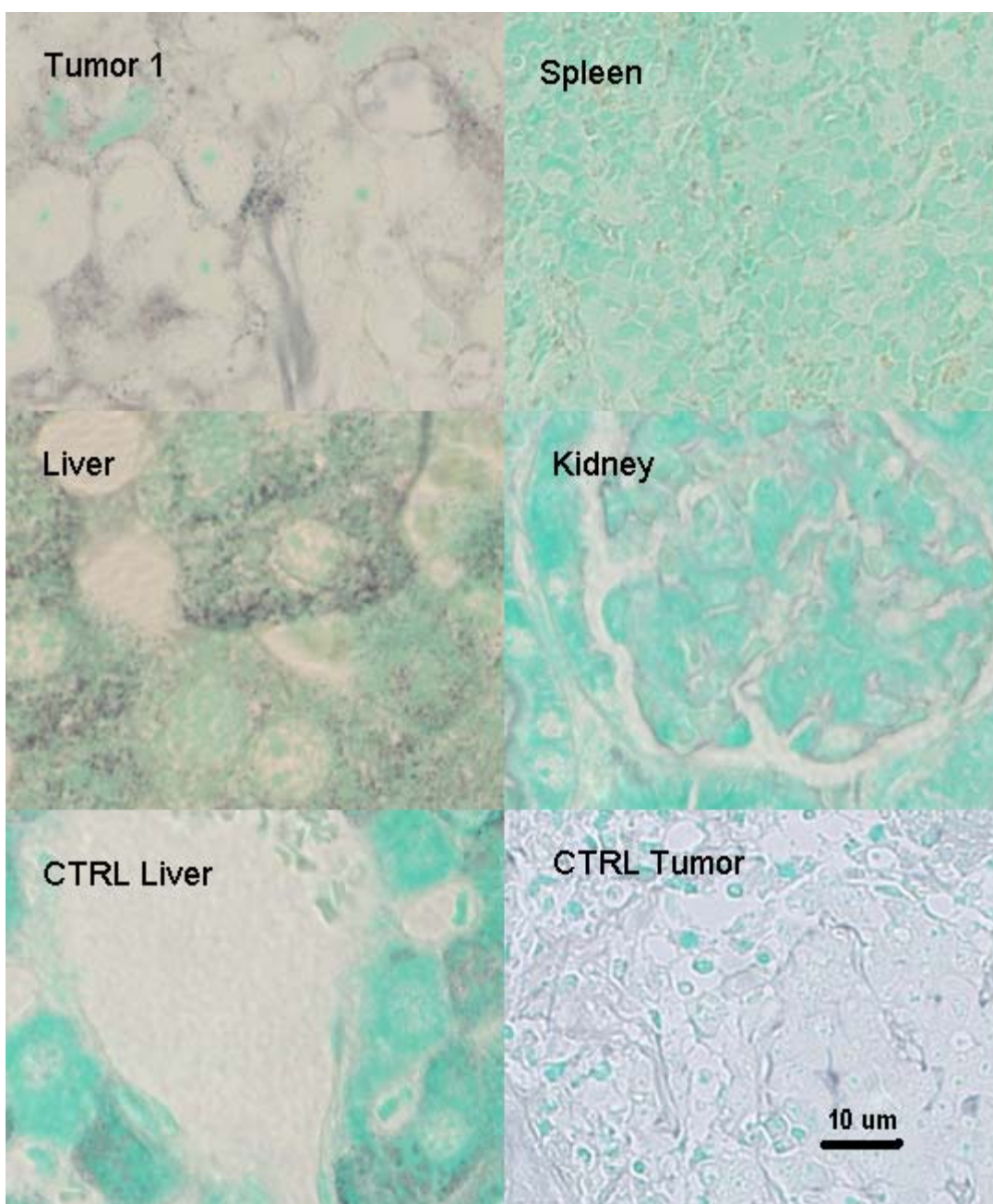


Figure 54: Bright field microscopic images of silver-enhanced staining of mouse tissue following intravenous injection of HER-PEG GNRs. Dark spots reveal GNRs. Two bottom images are obtained from mice injected with PBS as control.

5.6 LASER SAFETY IN THE PRESENCE OF GOLD NANOPARTICLES

In OAT, a laser pulse is used to irradiate the sample during imaging. An important aspect to consider when a laser device is used in medical imaging is the safety of the laser irradiation. Maximum Permissible Exposure (MPE) is defined as the maximum level of laser irradiation that under normal condition a person is allowed to be exposed to. MPE is usually calculated as 10% of the dose that is required to cause tissue damage in 50% of the subjects. Chances of tissue damage increase when the laser irradiation exceeds MPE limits. MPE is dependent on the type of tissue (e.g., skin, retina) and the wavelength of the laser, and whether the laser is used in a continuous or pulsed mode. MPE levels for skin laser irradiation can be found at American National Standards Institute (ANSI) Standard Z136.1 (132). For a pulse laser with a 10 ns pulse duration that emits light at visible range of the spectrum, MPE is defined to be 20 mJ/cm^2 . As the light absorption of tissue is less for near-infrared lasers, the MPE increases to 100 mJ/cm^2 at 1050 nm.

Optoacoustic experiments presented here were performed at an energy level bellow MPE. However, it should be noted that ANSI defines MPE in the absence of gold nanoparticles. The presence of gold nanoparticles within tissue, which significantly increases local light absorption of tissue, may lower the threshold of damage. An experiment was performed *in vitro* to assess if the presence of gold nanoparticles within tissue may cause cellular damage upon laser irradiation at levels that are used for OAT. Lactate dehydrogenase assay (LDH) was used in this experiment to assess the level of damage of cancer cells 24 hours post irradiation with laser pulses. BT-474 cancer cell lines were trypsinized and resuspended in Dulbecco's Modified Eagle Media (DMEM) supplemented with 10% serum. Then, 5×10^4 cells were transferred into each well of a 24-well culture plate and incubated at 37°C . After 24 hours, culture media was replaced with fresh media.

An Alexandrite laser running at 760 nm with pulse duration of 100 nanoseconds was used to generate a Gaussian laser beam with a diameter of 10 mm to illuminate a single well of culture plate at a time. The cells in culture plate were then divided into five groups and irradiated with laser pulses as listed in figure 55. Then, culture plate was incubated at 37°C for 24 hours as recommended by the manufacturer of LDH assay kit to release LDH from damaged cells. Cytotoxicity of laser irradiation was then determined by measuring the level of free LDH in culture media using Cytotoxicity Colorimetric Assay Kit (BioAssay Systems, Hayward, CA).

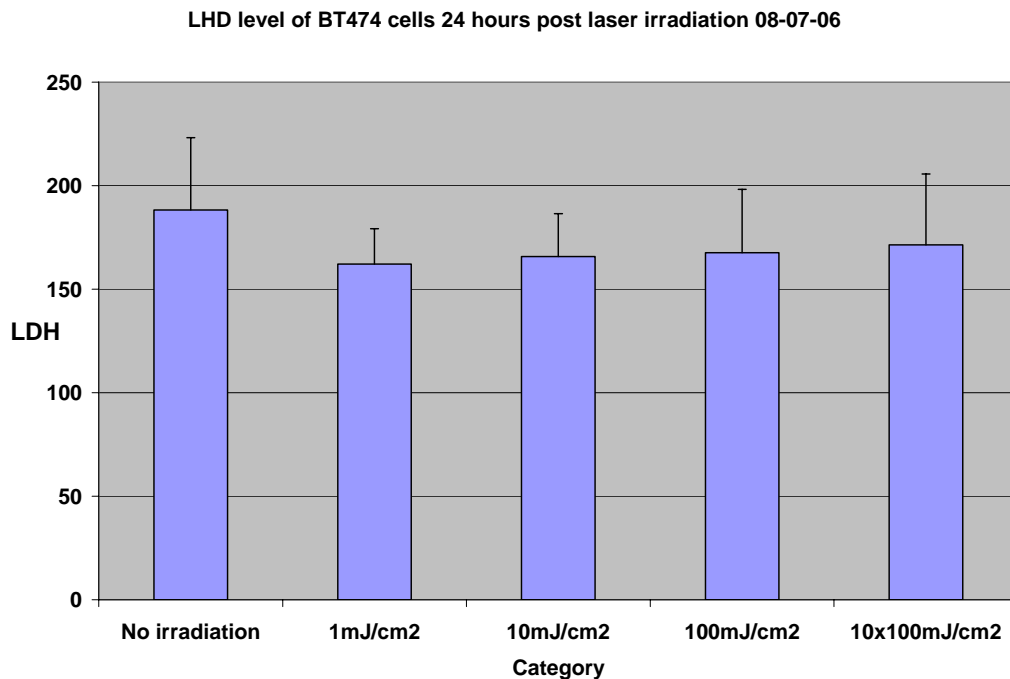


Figure 55: Level of released LDH by damaged BT-474 cells upon laser irradiation. No significance release of LDH (cytotoxicity) was detected. Each group contained four samples. Bars represent standard deviation.

Measuring LDH level in culture media post exposure to cytotoxic stimuli is a widely used assay to evaluate cellular damage. Damaged cells release their intracellular

LDH to the media while intact cells contain their LDH. As depicted in figure 55, no significant difference was detected among treatment groups. This means that laser irradiation in pulse mode with an intensity as high as 100 mJ/ cm^2 did not damage cells *in vitro*.

Next, we wanted to address laser safety issue in the presence of gold nanoparticles *in vivo*. To do this, an experiment was conducted using live mice, PEGylated gold nanoparticles, and an Alexandrite laser running at 757 nm. PEGylated gold nanoparticles were injected subcutaneously into the skin of mice and the skin was irradiated using an Alexandrite laser at 757 nm at different doses. The animals were observed for a predetermined time period up to 24 hours and were then sacrificed; samples of irradiated skin were obtained, fixed, and stained using H&E staining to reveal the extent of thermal damage. Figure 56 depicts an example of these series of experiments in which mouse skin was injected with 50 μL of PEGylated gold nanoparticles and irradiated with 10 pulses each at a fluence equal to 100 mJ/cm^2 . In this particular case, laser irradiation induced heat damage, but the extent of damage, which was assessed visually by determining the deformity of collagen bundles in H&E stained slides, was not affected by the presence of gold nanoparticles. The results of other experiments in this series showed that laser irradiation with a range of fluence that is normally used for OAT does not induce heat damage even in the presence of gold nanoparticles.

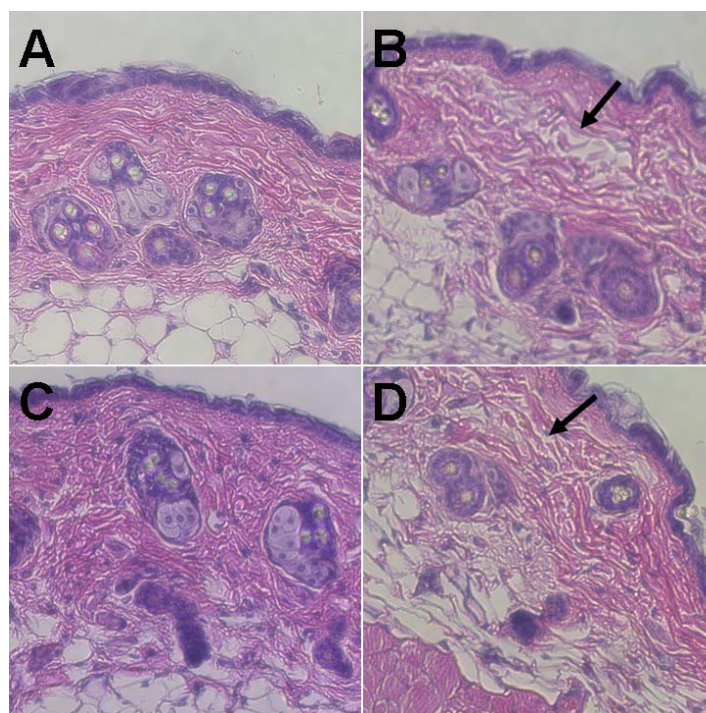


Figure 56: H&E staining of mouse skin eight hours post laser irradiation in the presence of GNRs. A 50 μL solution of PEGylated GNRs was injected subcutaneously into the skin using insulin needles, and the skin was then irradiated with 10 laser pulses at a fluence of $10 \times 100 \text{ mJ/cm}^2$. A= Normal skin (no irradiation), B= Irradiation alone, C= GNRs alone (no irradiation), D= GNRs and irradiation. Arrow shows the site of heat damage. GNRs did not affect the extent of tissue damage.

5.7 POTENTIAL LIMITATIONS OF GOLD NANOPARTICLES AS A CONTRAST AGENT

Like many other tools in biology, gold nanoparticles are not without problems. For instance, they are inert and remain in the body for a long time. Although supportive evidences exist in the literature to claim that these materials are well tolerated by body, there is no randomized study at this time to evaluate the long-term safety of gold nanoparticles in human.

Still another possible disadvantage is that they remain at the target site for a relatively long period of time and these remaining nanoparticles may interfere with repeating experiments. A possible solution would be to make gold nanorods in a way that they degrade gradually into smaller pieces so that the body can excrete them into urine.

5.8 SUMMARY

The toxicity of gold nanoparticles was studied in this chapter. The stability and functionality of engineered nanoparticles were examined *in vitro* and *in vivo* following intravenous injection into small animals. Also, the safety of tissue laser irradiation in the presence of gold nanoparticles was verified in mice following subcutaneous injection of gold nanoparticles.

Chapter 6: Comparing the Results of OAT against Those of Conventional Imaging Techniques

In the following chapter, the advantages and disadvantages of currently available modalities for breast imaging will be compared to that of OAT

6.1 COMPARING OAT WITH OTHER AVAILABLE NON-INVASIVE, NON-IONIZING IMAGING METHODS

It is usually useful to compare/contrast OAT with other available imaging techniques. In this section, we will compare/contrast OAT with three non-invasive and non-ionizing imaging modalities that are available for the imaging of breast: diffuse optical tomography (pure optical-based), ultrasonography (acoustic-based), and magnetic resonance imaging (MRI).

6.2 OAT VERSUS DIFFUSE OPTICAL TOMOGRAPHY

Like DOT, OAT uses the differential light absorption and scattering of tissues to generate an image. In both techniques one would need to deliver adequate near-infrared photons to the lesion that is located deep within tissue. To do this, a pulsed laser that provides high peak intensity (to maximize signal) with a low average power (to avoid heat damage) is used. Up to this point, both methods are similar. However, the situation would be different afterward: while DOT is dependent on the photons that come back to the surface, OAT needs generated acoustic waves to reach the surface. Breast tissue strongly attenuates photons on their pathway from lesion to the detector on the surface of skin, while ultrasound travels within tissue with much less attenuation. Due to minimal attenuation of ultrasound within breast tissue, generated ultrasound waves can be detected even after traveling 5 to 6 cm within tissue. In other words, the main advantage of OAT

over DOT is its depth of imaging; this advantage is due to the fact that OAT uses acoustic waves, instead of photons, to locate the source of signal.

6.3 OAT VERSUS CONVENTIONAL ULTRASONOGRAPHY

Ultrasonography is a non-invasive non-ionizing imaging method that is relatively low cost and can be repeated for a patient almost as many times as needed. Fine-needle biopsy with ultrasound guidance is a standard approach for suspicious lesions that are found in mammogram. Like OAT, conventional ultrasonography uses ultrasound to locate its target and thus both techniques possess a sub-millimeter spatial resolution at a depth of several centimeters within tissue.

However, a major disadvantage of conventional ultrasonography in breast imaging is the fact that it does not provide a good contrast between benign and malignant lesions. Abnormal angiogenesis within a tumor, which increases the light absorption of a tumor as a result of increased blood content (133), generates an inherent contrast agent for OAT. This is important because it will allow one to visualize tumors with abnormal angiogenesis using OAT without any need for using an exogenous contrast agent (134). Thus, OAT uses inherent optical contrasts that exist between benign and disease lesions as a result of enhanced angiogenesis, hypoxia, necrosis, and the accumulation of waste pigments within malignant lesions. In other words, the higher specificity of OAT to detect malignant lesions makes OAT superior to pure ultrasonography.

6.4 OAT VERSUS MRI

MRI is a very competitive imaging technique in medicine. It is non-invasive and provides high-resolution images even in the absence of exogenous contrast agent. The contrast within an MRI image could be enhanced using a variety of contrast agents including ferrimagnetic nanoparticles. It would be beneficial to compare the sensitivity of optoacoustic method for the detection of GNRs to the sensitivity of MRI for the detection of ferrimagnetic nanoparticles. Figure 39 shows that the minimum detectable concentration of GNRs with an average dimensions of 50x15 nm for optoacoustic method is 7.5×10^8 nanorods per mL (1.25 pM). To calculate the mass of elemental gold that is present in this solution, one would need to calculate the total volume of nanoparticles in the solution and multiply the result by the specific weight of gold (i.e. 19.3 grams/mL). This calculation yields 0.13 μg elemental gold per mL of GNRs solution. A search in the literature shows that Pardoe et al. (2003) used similar gelatin phantoms in their experiment and reported that the minimum concentration of ferrimagnetic nanoparticles detectable using MRI as 10 μg Fe per mL (135).

A comparison between the mass of elemental gold in the gold nanoparticle solution and the mass of Fe in the ferromagnetic nanoparticle solution shows that the sensitivity of optoacoustic method to detect gold nanoparticles is 75 times more than the sensitivity MRI to detect ferrimagnetic nanoparticles. It should be noted that the sensitivity of MRI would remain the same *in vivo*, while the sensitivity of OAT would be minimally affected by the background light absorption within tissue. For the *in vivo*

microenvironment, figure 39 shows that 25 μL of GNRs at a concentration of 1.25 pM ($\sim 0.13 \mu\text{g Au per mL}$) was detectable when injected into the skin of nude mouse. Considering the fact that OAT is in its embryonic stages of development while MRI systems have been improved over many years, the sensitivity experiments on OAT appears to be promising.

Chapter 7: Summary and Conclusion

Optoacoustic imaging is a novel imaging modality that promises non-invasive imaging of tissue based on the differential light absorption of diseased versus normal tissue. OAT is currently under clinical evaluation especially for the imaging of human breast(136;137); however, the sensitivity and specificity of this imaging technique can be improved by using exogenous contrast agents.

Diagnostic applications of nanoparticles are currently limited by the lack of available techniques to track nanoparticles at a low concentration deep within tissue. The ability to detect GNRs at a very low concentration deep within a tissue using optoacoustic methods, along with the fact that GNRs can be attached to vehicles such as monoclonal antibodies to target cancer cells, promises the development of new diagnostic modalities that employ optoacoustic methods and targeted GNRs as molecular-specific contrast agents for the early detection of cancer.

In this dissertation:

- 1) GNRs were engineered with the desired optical properties that are optimized for *in vivo* optoacoustic detection.
- 2) GNRs were modified chemically to enhance their biocompatibility and stability within blood microenvironment.
- 3) Molecular targeting of GNRs was achieved by engineering hetero-functional GNRs that possess covalently-attached monoclonal antibodies that recognize tumor markers on the surface of breast cancer cells.
- 4) Several *in vitro* and *in vivo* experiments were conducted to show the feasibility of imaging gold nanoparticles with a high sensitivity; i.e.

detecting a target with a concentration of 2×10^9 GNRs per mL and a size of a few nm in diameter.

The future directions of this research include:

- Improving the hardware that is required to detect optoacoustic signals with the highest possible signal to noise ratio *in vivo* as well as choosing alternate targeting mechanisms to accumulate even more nanoparticles within tumors.
- Translating data that has been acquired in small animals to human subjects.
- Because GNRs can be detected using multiple imaging modalities, OAT should be validated by imaging human subjects who have undergone conventional imaging such as CT scan, ultrasound, and MRI.
- The use of GNRs as a contrast agent for diagnostic applications could be combined with delivering a variety of therapeutic agents to cancer cells simultaneously.

In summary, functionalizing gold nanoparticles to accumulate within tumor enhances the diagnostic applications of optoacoustic imaging, which is a rapidly growing imaging modality especially in the field of breast imaging. In addition, unique optical and chemical properties of gold nanorods enable scientists to employ them in other diagnostic (ex. X-ray or CT scan) or therapeutic (ex. Photo-ablation) applications once they are specifically targeted to cancer cell.

Appendix A

GNRS PROTOCOL

Prepare Ice-cold water, 30°C bath, stirring machine, and 15 mL tubes.

- 1- Prepare 0.1 M solution of CTAB: dissolve 3.65 grams of CTAB (Sigma, Ultrapure 99%) in 100 mL DI water. You will need to stir it for 30 minutes to fully dissolve CTAB. Pass it through 0.22 μm filter using a syringe to remove undissolved component. Keep it at 30°C to prevent crystal formation.
- 2- Prepare stock solution of 0.01 M gold salt (Aldrich 254169-5G) in DI water. MW of this product is 337 and thus 0.01 M is equal to 3.37 mg/mL. You will need a total of 4 mL to make 60 mL of nanorods.
- 3- Prepare ascorbic acid 0.1 M (Sigma A7506). This is equal to 17 mg/mL. You need to make about 1 mL; it must be prepared fresh.
- 4- Prepare stock of 0.01 M sodium borohydrate (Aldrich 452882) in ice-cold DI water. This is equal to 0.38 mg/mL. Uncap the bottle, as it may release some gas. You will need a total of 2 mL for 60 mL nanorods.
- 5- Prepare stock solution of 0.01 M silver nitrate (Sigma 209139-25G). This is equal to 1.7 mg/mL. You will need less than 1 mL of this stock to for 60 mL of nanorods.
- 6- Prepare seed solution in a 15 mL tubes by adding 7.5 mL CTAB 0.1 M, 250 μL Gold Stock 0.01 M, 0.6 mL Sodium Hydroborate at 30°C:
The color of this solution will darken when you add gold to CTAB. Add sodium borohydrate at once and invert tube 10 times to fully mix it; remove the cap after mixing to release gas. Keep seed solutions at 30°C to prevent crystal formation. This solution will contain $3 \times 10^{-4} \text{M}$ of Au.
- 7- Prepare three 15 mL tubes for nanorods growth by adding the following components from left to right:

Table 1. Produced Gold Nanorod Dimensions and Yield, with Corresponding Initial Concentrations of Reactants^a

product		reaction conditions				figure number
dimension ^b (length × width)	yield ^b	[Au ³⁺], M	[Ag ⁺], M	[AA], M	[Au] _{seed} , M	
87 (±17) × 42 (±10)	97 (±3)	4.0 × 10 ⁻⁴	6.0 × 10 ⁻⁵	6.4 × 10 ⁻⁴	1.25 × 10 ⁻⁷	2a
64 (±12) × 24 (±6)	97 (±3)	4.0 × 10 ⁻⁴	6.0 × 10 ⁻⁵	6.4 × 10 ⁻⁴	2.5 × 10 ⁻⁷	2b
62 (±10) × 23 (±3)	93 (±5)	4.0 × 10 ⁻⁴	6.0 × 10 ⁻⁵	6.4 × 10 ⁻⁴	5.0 × 10 ⁻⁷	2c
50 (±5) × 15 (±3)	90 (±5)	4.0 × 10 ⁻⁴	6.0 × 10 ⁻⁵	6.4 × 10 ⁻⁴	1.25 × 10 ⁻⁶	2d
475 (±24) × 15 (±2)	55 (±12)	4.0 × 10 ⁻⁴	6.0 × 10 ⁻⁵	6.4 × 10 ⁻⁴	5.0 × 10 ⁻⁷	2e
80 (±15) × 40 (±10)	97 (±3)	6.0 × 10 ⁻⁴	6.0 × 10 ⁻⁵	9.6 × 10 ⁻⁴	5.0 × 10 ⁻⁷	6a
54 (±10) × 14 (±3)	90 (±5)	3.0 × 10 ⁻⁴	6.0 × 10 ⁻⁵	2.4 × 10 ⁻⁴	5.0 × 10 ⁻⁷	6b
22 (±3) × 6 (±2)	88 (±5)	1.0 × 10 ⁻⁴	6.0 × 10 ⁻⁵	1.6 × 10 ⁻⁴	5.0 × 10 ⁻⁷	6c
90 (±11) × 15 (±2)	57 (±14)	4.0 × 10 ⁻⁴		3.0 × 10 ⁻³	5.0 × 10 ⁻⁷	7a
75 (±8) × 10 (±2)	55 (±14)	4.0 × 10 ⁻⁴		3.0 × 10 ⁻³	1.5 × 10 ⁻⁶	7b
50 (±6) × 10 (±2)	55 (±17)	4.0 × 10 ⁻⁴		3.0 × 10 ⁻³	2.5 × 10 ⁻⁶	7c

^a Reactants were added in the order indicated, from left to right. All reactions were run in 5 mL of aqueous 9.5 × 10⁻² M CTAB solutions at room temperature. ^b A total of 600 particles from three identical batches (200 particles from each) were counted to calculate the rod yield, and 150 nanorods (50 nanorods from each identical batch) were considered to calculate the average rod dimension. Rod yield is given by (number of rods)/(total number of particles) × 100%. The error bars in the dimensions correspond to one standard deviation in each case.

Table 1: Final molar concentrations of reactants needed to produce gold nanorods with desired dimensions. Taken from Murphy et al. (92)

Size of NPs	CTAB	Gold Salt	Silver	Ascorbic Acid	Seeds
	0.1M	0.01M	0.01M	0.1M	
87x42	4.7 mL	200 μL	30 μL	32 μL	2 μL
64x24	4.7 mL	200 μL	30 μL	32 μL	4 μL
62x23	4.7 mL	200 μL	30 μL	32 μL	8 μL
50x15	4.7 mL	200 μL	30 μL	32 μL	21 μL
54x14	4.7 mL	150 μL	30 μL	12 μL	8 μL
22x6	4.7 mL	50 μL	30 μL	8 μL	8 μL

Table 2: Calculated volume of the stock solution of materials needed to make gold nanorods. Volumes are calculated to achieve the concentrations that are mentioned in table 1.

- 8- The solution will become colorless after adding ascorbic acid. At this stage, wait for about 10 minutes for the reaction to fully proceed and then add seeds.
- 9- The color of tubes will darken in about 10 minutes. Do not disturb tube for one hour.

Appendix B

PRODUCING FLUORESCENTLY LABELED AND HERCEPTIN-CONJUGATED GNRS USING PAA

- 1) 2 mL CTAB-stabilized GNRS were centrifuged at 8000 RPM for 30 minutes and resuspended in 1 mL dH₂O.
- 2) NP solution was centrifuged again and resuspended in 500 uL of dH₂O.
- 3) A stock solution of 1uLmL PAA (Sigma, MW 15000) in 1 mM NaCl was prepared.
- 4) 500 uL of stock solution of PAA was added to 500 uL of NP gradually under vigorous shaking. The solution was incubated at room temperature for 15 minutes.
- 5) Centrifuge at 8000 RPM for 5 minutes and resuspend in 1 mM NaCl.
- 6) Repeat centrifugation and resuspend in 0.01 M MES buffer at pH=5.0 to produce PAA-coated nanoparticle solution
- 7) Mix 1 mg purified Herceptin with 500 uL of PAA-coated NP solution
- 8) Dissolve 1 mg EDC in 100 uL dH₂O and immediately add it to the mixture of NP and Herceptin made in previous step
- 9) Incubate at room temperature for 2 hours
- 10) Centrifuge at 5000 RPM for 5 minutes and resuspend in 0.05 M bicarbonate buffer
- 11) Dissolve 0.1 mg Alexa Fluor 568 succinimidyl ester in 5 uL DMF and add it gradually to nanoparticle solution
- 12) Incubate at room temperature for one hour
- 13) Centrifuge at 5000 RPM for 5 minutes and resuspend in 1 mL PBS
- 14) Centrifuge again and resuspend in 100 uL PBS

Bibliography

- (1) NCI. Cancer Stat Fact Sheets. Cancer of the Breast 2008.
- (2) Bartella L, Smith CS, Dershaw DD, Liberman L. Imaging breast cancer. *Radiologic Clinics of North America* 2007; 45(1):45-67.
- (3) Nystrom L, Andersson I, Bjurstam N, Frisell J, Nordenskjold B, Rutqvist LE. Long-term effects of mammography screening: updated overview of the Swedish randomised trials. *Lancet* 2002; 359(9310):909-919.
- (4) Brannon-Peppas L, Blanchette JO. Nanoparticle and targeted systems for cancer therapy. *Advanced Drug Delivery Reviews* 2004; 56(11):1649-1659.
- (5) Broome DR. Nephrogenic systemic fibrosis associated with gadolinium based contrast agents: a summary of the medical literature reporting. *European Journal of Radiology* 2008; 66(2):230-234.
- (6) Thomsen HS. Is NSF only the tip of the "gadolinium toxicity" iceberg? *Journal of Magnetic Resonance Imaging* 2008; 28(2):284-286.
- (7) Harmon RC, Duffy SP, Terneus MV, Ball JG, Valentovic MA. Characterization of a novel model for investigation of radiocontrast nephrotoxicity. *Nephrology, Dialysis, Transplantation* 2008.
- (8) Bassett LW, Kimmesmith C, Sutherland LK, Gold RH, Sarti D, King W. Automated and Hand-Held Breast Us - Effect on Patient-Management. *Radiology* 1987; 165(1):103-108.
- (9) Schueller G, Schueller-Weidekamm C, Helbich TH. Accuracy of ultrasound-guided, large-core needle breast biopsy. *European Radiology* 2008; 18(9):1761-1773.
- (10) Sauer G, Deissler H, Strunz K, Helms G, Rimmel E, Koretz K et al. Ultrasound-guided large-core needle biopsies of breast lesions: analysis of 962 cases to determine the number of samples for reliable tumour classification. *British Journal of Cancer* 2005; 92(2):231-235.
- (11) Balleyguier C, Opolon P, Mathieu MC, Athanasiou A, Garbay JR, Delalogue S et al. New potential and applications of contrast-enhanced ultrasound of the breast: Own investigations and review of the literature. *European Journal of Radiology* 2008; Epub ahead of print.

- (12) Ricci P, Cantisani V, Ballezio L, Pagliara E, Sallusti E, Drudi FM et al. Benign and malignant breast lesions: Efficacy of real time contrast-enhanced ultrasound vs. magnetic resonance imaging. *Ultraschall in der Medizin* 2007; 28(1):57-62.
- (13) Jung EM, Jungius KP, Rupp N, Gallegos M, Ritter G, Lenhart M et al. Contrast enhanced harmonic ultrasound for differentiating breast tumors - First results. *Clinical Hemorheology and Microcirculation* 2005; 33(2):109-120.
- (14) Maeda H, Fang J, Inutsuka T, Kitamoto Y. Vascular permeability enhancement in solid tumor: various factors, mechanisms involved and its implications. *International Immunopharmacology* 2003; 3(3):319-328.
- (15) Hauff P, Reinhardt M, Foster S. Ultrasound basics. *Handbook of Experimental Pharmacology* 2008;(185 Pt 1):91-107.
- (16) Berg WA, Gutierrez L, NessAiver MS, Carter WB, Bhargavan M, Lewis RS et al. Diagnostic accuracy of mammography, clinical examination, US, and MR imaging in preoperative assessment of breast cancer. *Radiology* 2004; 233(3):830-849.
- (17) Hawrysz DJ, Sevick-Muraca EM. Developments toward diagnostic breast cancer imaging using near-infrared optical measurements and fluorescent contrast agents. *Neoplasia* 2000; 2(5):388-417.
- (18) Kepshire DS, Davis SC, Dehghani H, Paulsen KD, Pogue BW. Subsurface diffuse optical tomography can localize absorber and fluorescent objects but recovered image sensitivity is nonlinear with depth. *Applied Optics* 2007; 46(10):1669-1678.
- (19) Frangioni JV. New technologies for human cancer imaging. *Journal of clinical Oncology* 2008; 26(24):4012-4021.
- (20) Leveque-Fort S. Three-dimensional acousto-optic imaging in biological tissues with parallel signal processing. *Applied Optics* 2001; 40(7):1029-1036.
- (21) Fischgrabe J, Wulfing P. Targeted therapies in breast cancer: established drugs and recent developments. *Current Clinical Pharmacology* 2008; 3(2):85-98.
- (22) Garanger E, Boturyn D, Dumy P. Tumor targeting with RGD peptide ligands- design of new molecular conjugates for imaging and therapy of cancers. *Anticancer Agents in Medicinal Chemistry* 2007; 7(5):552-558.
- (23) Laakkonen P, Zhang L, Ruoslahti E. Peptide targeting of tumor lymph vessels. *Annals of the New York Accademy of Sciences* 2008; 1131:37-43.

- (24) Abd-Elgaliel WR, Gallazzi F, Garrison JC, Rold TL, Sieckman GL, Figueroa SD et al. Design, synthesis, and biological evaluation of an antagonist-bombesin analogue as targeting vector. *Bioconjugate Chemistry* 2008; 19(10):2040-2048.
- (25) Carter P, Smith L, Ryan M. Identification and validation of cell surface antigens for antibody targeting in oncology. *Endocrine-Related Cancer* 2004; 11(4):659-687.
- (26) Bernard-Marty C, Lebrun F, Awada A, Piccart MJ. Monoclonal antibody-based targeted therapy in breast cancer: Current status and future directions. *Drugs* 2006; 66(12):1577-1591.
- (27) Hoff ER, Tubbs RR, Myles JL, Procop GW. HER2/neu amplification in breast cancer - Stratification by tumor type and grade. *American Journal of Clinical Pathology* 2002; 117(6):916-921.
- (28) Plosker GL, Keam SJ. Trastuzumab - A review of its use in the management of HER2-positive metastatic and early-stage breast cancer. *Drugs* 2006; 66(4):449-475.
- (29) Wang SC, Zhang L, Hortobagyi GN, Hung MC. Targeting HER2: recent developments and future directions for breast cancer patients. *Seminars in Oncology* 2001; 28(6 Suppl 18):21-29.
- (30) Park JW, Kirpotin DB, Hong K, Shalaby R, Shao Y, Nielsen UB et al. Tumor targeting using anti-her2 immunoliposomes. *Journal of Controlled Release* 2001; 74(1-3):95-113.
- (31) Mitchell MS, Press MF. The role of immunohistochemistry and fluorescence in situ hybridization for HER-2/neu in assessing the prognosis of breast cancer. *Seminars in Oncology* 1999; 26(4):108-116.
- (32) Artemov D, Mori N, Okollie B, Bhujwala ZM. MR molecular imaging of the Her-2/neu receptor in breast cancer cells using targeted iron oxide nanoparticles. *Magnetic Resonance in Medicine* 2003; 49(3):403-408.
- (33) Fujimura M, Katsumata N, Tsuda H, Uchi N, Miyazaki S, Hidaka T et al. HER2 is frequently over-expressed in ovarian clear cell adenocarcinoma: Possible novel treatment modality using recombinant monoclonal antibody against HER2, trastuzumab. *Japanese Journal of Cancer Research* 2002; 93(11):1250-1257.
- (34) Lin A, Rugo HS. The role of trastuzumab in early stage breast cancer: current data and treatment recommendations. *Current Treatment Options in Oncology* 2007; 8(1):47-60.

- (35) Stal O, Borg A, Ferno M, Kallstrom AC, Malmstrom P, Nordenskjold B. ErbB2 status and the benefit from two or five years of adjuvant tamoxifen in postmenopausal early stage breast cancer. *Annals of Oncology* 2000; 11(12):1545-1550.
- (36) Yezhelyev MV, Gao X, Xing Y, Al Hajj A, Nie S, O'Regan RM. Emerging use of nanoparticles in diagnosis and treatment of breast cancer. *The Lancet Oncology* 2006; 7(8):657-667.
- (37) Ferrari M. Cancer nanotechnology: Opportunities and challenges. *Nature Reviews Cancer* 2005; 5(3):161-171.
- (38) Nasongkla N, Bey E, Ren JM, Ai H, Khemtong C, Guthi JS et al. Multifunctional polymeric micelles as cancer-targeted, MRI-ultrasensitive drug delivery systems. *Nano Letters* 2006; 6(11):2427-2430.
- (39) Roy I, Ohulchanskyy TY, Pudavar HE, Bergey EJ, Oseroff AR, Morgan J et al. Ceramic-based nanoparticles entrapping water-insoluble photosensitizing anticancer drugs: A novel drug-carrier system for photodynamic therapy. *Journal of the American Chemical Society* 2003; 125(26):7860-7865.
- (40) Vinogradov SV, Zeman AD, Batrakova EV, Kabanov AV. Polyplex Nanogel formulations for drug delivery of cytotoxic nucleoside analogs. *Journal of Controlled Release* 2005; 107(1):143-157.
- (41) Gao X, Cui Y, Levenson RM, Chung LWK, Nie S. In vivo cancer targeting and imaging with semiconductor quantum dots. *Nature Biotechnology* 2004; 22(8):969-976.
- (42) Cuenca AG, Jiang HB, Hochwald SN, Delano M, Cance WG, Grobmyer SR. Emerging implications of nanotechnology on cancer diagnostics and therapeutics. *Cancer* 2006; 107(3):459-466.
- (43) Iyer AK, Khaled G, Fang J, Maeda H. Exploiting the enhanced permeability and retention effect for tumor targeting. *Drug Discovery Today* 2006; 11(17-18):812-818.
- (44) Steinhauser I, Spankuch B, Strebhardt K, Langer K. Trastuzumab-modified nanoparticles: Optimisation of preparation and uptake in cancer cells. *Biomaterials* 2006; 27(28):4975-4983.
- (45) Owens DE, Peppas NA. Opsonization, biodistribution, and pharmacokinetics of polymeric nanoparticles. *International Journal of Pharmaceutics* 2006; 307(1):93-102.

- (46) Olivier JC, Huertas R, Lee HJ, Calon F, Pardridge WM. Synthesis of pegylated immunonanoparticles. *Pharmaceutical Research* 2002; 19(8):1137-1143.
- (47) Oyewumi MO, Yokel RA, Jay M, Coakley T, Mumper RJ. Comparison of cell uptake, biodistribution and tumor retention of folate-coated and PEG-coated gadolinium nanoparticles in tumor-bearing mice. *Journal of Controlled Release* 2004; 95(3):613-626.
- (48) Mori T. Cancer-specific ligands identified from screening of peptide-display libraries. *Current Pharmaceutical Design* 2004; 10(19):2335-2343.
- (49) Farokhzad OC, Cheng JJ, Teply BA, Sherifi I, Jon S, Kantoff PW et al. Targeted nanoparticle-aptamer bioconjugates for cancer chemotherapy in vivo. *Proceedings of the National Academy of Sciences of the United States of America* 2006; 103(16):6315-6320.
- (50) Schmid T. Photoacoustic spectroscopy for process analysis. *Analytical and Bioanalytical Chemistry* 2006; 384(5):1071-1086.
- (51) Oraevsky A, Karabutov A. Optoacoustic Tomography. In: Vo-Dinh T, editor. *Biomedical Photonics Handbook*. CRC Press, Boca Raton, FL, 2003: 34.1-34.34.
- (52) Kruger RA, Liu PY, Fang YR, Appledorn CR. Photoacoustic Ultrasound (Paus) - Reconstruction Tomography. *Medical Physics* 1995; 22(10):1605-1609.
- (53) Kostli KP, Frenz M, Bebie H, Weber HP. Temporal backward projection of optoacoustic pressure transients using Fourier transform methods. *Physics in Medicine and Biology* 2001; 46(7):1863-1872.
- (54) Kostli KP, Frauchiger D, Niederhauser JJ, Paltauf G, Weber HP, Frenz M. Optoacoustic imaging using a three-dimensional reconstruction algorithm. *Ieee Journal of Selected Topics in Quantum Electronics* 2001; 7(6):918-923.
- (55) Paltauf G, Viator JA, Prah SA, Jacques SL. Iterative reconstruction algorithm for optoacoustic imaging. *Journal of the Acoustical Society of America* 2002; 112(4):1536-1544.
- (56) Paltauf G, SchmidtKloiber H, Guss H. Light distribution measurements in absorbing materials by optical detection of laser-induced stress waves. *Applied Physics Letters* 1996; 69(11):1526-1528.
- (57) Petrova IY, Esenaliev RO, Petrov YY, Brecht HPE, Svensen CH, Olsson J et al. Optoacoustic monitoring of blood hemoglobin concentration: a pilot clinical study. *Optics Letters* 2005; 30(13):1677-1679.

- (58) Kandulla J, Elsner H, Birngruber R, Brinkmann R. Noninvasive optoacoustic online retinal temperature determination during continuous-wave laser irradiation. *Journal of Biomedical Optics* 2006; 11(4).
- (59) Song KH, Stoica G, Wang LHV. In vivo three-dimensional photoacoustic tomography of a whole mouse head. *Optics Letters* 2006; 31(16):2453-2455.
- (60) Niederhauser JJ, Jaeger M, Lemor R, Weber P, Frenz M. Combined ultrasound and optoacoustic system for real-time high-contrast vascular imaging in vivo. *Ieee Transactions on Medical Imaging* 2005; 24(4):436-440.
- (61) Cerussi AE, Berger AJ, Bevilacqua F, Shah N, Jakubowski D, Butler J et al. Sources of absorption and scattering contrast for near-infrared optical mammography. *Academic Radiology* 2001; 8(3):211-218.
- (62) Weissleder R. A clearer vision for in vivo imaging. *Nature Biotechnology* 2001; 19(4):316-317.
- (63) Copland JA, Eghtedari M, Popov VL, Kotov N, Mamedova N, Motamedi M et al. Bioconjugated gold nanoparticles as a molecular based contrast agent: Implications for imaging of deep tumors using optoacoustic tomography. *Molecular Imaging and Biology* 2004; 6(5):341-349.
- (64) Ermilov SA, Stein A, Conjustea A, Gharieb RR, Lacewell R, Miller T et al. Detection and noninvasive diagnostics of breast cancer with two-color laser optoacoustic imaging system. *Proceedings of the Society of Photo-Optical Instrumentation Engineers* 2007; 6437: 6437031-6437037.:6437031-6437037.
- (65) Ermilov SA, Khamapirad T, Gharieb RR, Conjusteau A, Leonard MH, Lacewell R et al. Laser Optoacoustic Imaging System for Detection of Breast Cancer: Technical Parameters and Clinical Feasibility. *Journal of Biomedical Optics* 2009; In Press.
- (66) Kaidoh T, Yasugi T, Uehara Y. The microvasculature of the 7,12-dimethylbenz(a)anthracene (DMBA)-induced rat mammary tumour. I. Vascular patterns as visualized by scanning electron microscopy of corrosion casts. *Virchows Archive A, Pathology, Pathologische Anatomie* 1991; 418(2):111-117.
- (67) Kolkman RG, Mulder MJ, Glade CP, Steenbergen W, van Leeuwen TG. Photoacoustic imaging of port-wine stains. *Lasers in Surgery and Medicine* 2008; 40(3):178-182.
- (68) Viator JA, Komadina J, Svaasand LO, Aguilar G, Choi B, Stuart NJ. A comparative study of photoacoustic and reflectance methods for determination

- of epidermal melanin content. *Journal of Investigative Dermatology* 2004; 122(6):1432-1439.
- (69) Petrova IY, Esenaliev RO, Petrov YY, Brecht HP, Svensen CH, Olsson J et al. Optoacoustic monitoring of blood hemoglobin concentration: a pilot clinical study. *Optics Letters* 2005; 30(13):1677-1679.
- (70) Niederhauser JJ, Jaeger M, Lemor R, Weber P, Frenz M. Combined ultrasound and optoacoustic system for real-time high-contrast vascular imaging in vivo. *Ieee Transactions on Medical Imaging* 2005; 24(4):436-440.
- (71) Ku G, Wang LHV. Deeply penetrating photoacoustic tomography in biological tissues enhanced with an optical contrast agent. *Optics Letters* 2005; 30(5):507-509.
- (72) Kim G, Huang SW, Day KC, O'Donnell M, Agayan RR, Day MA et al. Indocyanine-green-embedded PEBBLEs as a contrast agent for photoacoustic imaging. *Journal of Biomedical Optics* 2007; 12(4).
- (73) El Sayed MA. Some interesting observed properties of metals confined in time and space of different shapes. *Abstracts of Papers of the American Chemical Society* 2000; 220:U236.
- (74) Oraevsky AA, Oraevsky AN. On a plasmon resonance in ellipsoidal nanoparticles. *Quantum Electronics* 2002; 32(1):79-82.
- (75) Hu M, Chen JY, Li ZY, Au L, Hartland GV, Li XD et al. Gold nanostructures: engineering their plasmonic properties for biomedical applications. *Chemical Society Reviews* 2006; 35(11):1084-1094.
- (76) Link S, El Sayed MA. Size and temperature dependence of the plasmon absorption of colloidal gold nanoparticles. *Journal of Physical Chemistry B* 1999; 103(21):4212-4217.
- (77) Roth J. The silver anniversary of gold: 25 years of the colloidal gold marker system for immunocytochemistry and histochemistry. *Histochemistry and Cell Biology* 1996; 106(1):1-8.
- (78) Holgate CS, Jackson P, Cowen PN, Bird CC. Immunogold-Silver Staining - New Method of Immunostaining with Enhanced Sensitivity. *Journal of Pathology* 1983; 139(4):492.
- (79) Wang W, Singh S, Zeng DL, King K, Nema S. Antibody structure, instability, and formulation. *Journal of Pharmaceutical Sciences* 2007; 96(1):1-26.

- (80) Katz E, Willner I. Integrated nanoparticle-biomolecule hybrid systems: Synthesis, properties, and applications. *Angewandte Chemie-International Edition* 2004; 43(45):6042-6108.
- (81) Duncan RJS, Weston PD, Wrigglesworth R. A New Reagent Which May be Used to Introduce Sulfhydryl-Groups Into Proteins, and Its Use in the Preparation of Conjugates for Immunoassay. *Analytical Biochemistry* 1983; 132(1):68-73.
- (82) Hermanson GT. Avidin-Biotin Systems. In: Hermanson GT, editor. *Bioconjugate Techniques*. Academic Press, Burlington, MA, 1996: 570-592.
- (83) Eghtedari M, Oraevsky A, Copland JA, Kotov NA, Conjusteau A, Motamedi M. High sensitivity of *in vivo* detection of gold nanorods using a laser optoacoustic imaging system. *Nano Letters* 2007; 7(7):1914-1918.
- (84) Eghtedari M, Liopo AV, Copland JA, Oraevsky AA, Motamedi M. Engineering of hetero-functional gold nanorods for the *in-vivo* molecular targeting of breast cancer cells. *Nano Letters* 2008; in press.
- (85) Wilson BC. Appendix to chapter 8: summary of optical properties. In: Welch AJ, Van Gemert MJC, editors. *Optical-thermal response of laser-irradiated tissue*. Plenum, 1995: 275-303.
- (86) Jain PK, Lee KS, El Sayed IH, El Sayed MA. Calculated absorption and scattering properties of gold nanoparticles of different size, shape, and composition: Applications in biological imaging and biomedicine. *Journal of Physical Chemistry B* 2006; 110(14):7238-7248.
- (87) Mobley J, Vo-Dinh T. Optical properties of tissue. In: Vo-Dinh T, editor. *Biomedical Photonics Handbook*. CRC Press, 2003: 38-75.
- (88) Chen JY, Wiley B, Li ZY, Campbell D, Saeki F, Cang H et al. Gold nanocages: Engineering their structure for biomedical applications. *Advanced Materials* 2005; 17(18):2255-2261.
- (89) Hirsch LR, Gobin AM, Lowery AR, Tam F, Drezek RA, Halas NJ et al. Metal nanoshells. *Annals of Biomedical Engineering* 2006; 34(1):15-22.
- (90) Gao JX, Bender CM, Murphy CJ. Dependence of the gold nanorod aspect ratio on the nature of the directing surfactant in aqueous solution. *Langmuir* 2003; 19(21):9065-9070.
- (91) Gole A, Murphy CJ. Seed-mediated synthesis of gold nanorods: Role of the size and nature of the seed. *Chemistry of Materials* 2004; 16(19):3633-3640.

- (92) Sau TK, Murphy CJ. Seeded high yield synthesis of short Au nanorods in aqueous solution. *Langmuir* 2004; 20(15):6414-6420.
- (93) Huang XH, El Sayed IH, Qian W, El Sayed MA. Cancer cell imaging and photothermal therapy in the near-infrared region by using gold nanorods. *Journal of the American Chemical Society* 2006; 128(6):2115-2120.
- (94) Murphy CJ, San TK, Gole AM, Orendorff CJ, Gao JX, Gou L et al. Anisotropic metal nanoparticles: Synthesis, assembly, and optical applications. *Journal of Physical Chemistry B* 2005; 109(29):13857-13870.
- (95) Sosinsky GE, Giepmans BN, Deerinck TJ, Gaietta GM, Ellisman MH. Markers for correlated light and electron microscopy. *Methods in Cell Biology* 2007; 79:575-591.
- (96) Nagesha D, Laevsky GS, Lampton P, Banyal R, Warner C, DiMarzio C et al. In vitro imaging of embryonic stem cells using multiphoton luminescence of gold nanoparticles. *International Journal of Nanomedicine* 2007; 2(4):813-819.
- (97) Adler DC, Huang SW, Huber R, Fujimoto JG. Photothermal detection of gold nanoparticles using phase-sensitive optical coherence tomography. *Optics Express* 2008; 16(7):4376-4393.
- (98) Kneipp K, Kneipp H, Kneipp J. Surface-enhanced Raman scattering in local optical fields of silver and gold nanoaggregates-from single-molecule Raman spectroscopy to ultrasensitive probing in live cells. *Accounts of Chemical Research* 2006; 39(7):443-450.
- (99) Hainfeld JF, Slatkin DN, Focella TM, Smilowitz HM. Gold nanoparticles: a new X-ray contrast agent. *British Journal of Radiology* 2006; 79(939):248-253.
- (100) Cai QY, Kim SH, Choi KS, Kim SY, Byun SJ, Kim KW et al. Colloidal gold nanoparticles as a blood-pool contrast agent for X-ray computed tomography in mice. *Investigative Radiology* 2007; 42(12):797-806.
- (101) Wang H, Huff TB, Zweifel DA, He W, Low PS, Wei A et al. In vitro and in vivo two-photon luminescence imaging of single gold nanorods. *Proceedings of the National Academy of Sciences of the United States of America* 2005; 102(44):15752-15756.
- (102) Durr NJ, Larson T, Smith DK, Korgel BA, Sokolov K, Ben Yakar A. Two-photon luminescence imaging of cancer cells using molecularly targeted gold nanorods. *Nano Letters* 2007; 7(4):941-945.

- (103) El Sayed IH, Huang XH, El Sayed MA. Selective laser photo-thermal therapy of epithelial carcinoma using anti-EGFR antibody conjugated gold nanoparticles. *Cancer Letters* 2006; 239(1):129-135.
- (104) Niidome T, Yamagata M, Okamoto Y, Akiyama Y, Takahashi H, Kawano T et al. PEG-modified gold nanorods with a stealth character for in vivo applications. *Journal of Controlled Release* 2006; 114(3):343-347.
- (105) Gole A, Murphy CJ. Biotin-streptavidin-induced aggregation of gold nanorods: Tuning rod-rod orientation. *Langmuir* 2005; 21(23):10756-10762.
- (106) Connor EE, Mwamuka J, Gole A, Murphy CJ, Wyatt MD. Gold nanoparticles are taken up by human cells but do not cause acute cytotoxicity. *Small* 2005; 1(3):325-327.
- (107) De Maria M, De Simone G, Laconi A, Mercadante G, Pavone P, Rossi P. Gold storage in the liver: appearance on CT scans. *Radiology* 1986; 159(2):355-356.
- (108) Wang ZL, Mohamed MB, Link S, El Sayed MA. Crystallographic facets and shapes of gold nanorods of different aspect ratios. *Surface Science* 1999; 440(1-2):L809-L814.
- (109) Wang ZL, Gao RP, Nikoobakht B, El Sayed MA. Surface reconstruction of the unstable {110} surface in gold nanorods. *Journal of Physical Chemistry B* 2000; 104(23):5417-5420.
- (110) Chang JY, Wu HM, Chen H, Ling YC, Tan WH. Oriented assembly of Au nanorods using biorecognition system. *Chemical Communications* 2005;(8):1092-1094.
- (111) Caswell KK, Wilson JN, Bunz UHF, Murphy CJ. Preferential end-to-end assembly of gold nanorods by biotin-streptavidin connectors. *Journal of the American Chemical Society* 2003; 125(46):13914-13915.
- (112) Keul HA, Moller M, Bockstaller MR. Structural Evolution of Gold Nanorods during Controlled Secondary Growth. *Langmuir* 2007; 23(20):10307-15.
- (113) Hirsch LR, Stafford RJ, Bankson JA, Sershen SR, Rivera B, Price RE et al. Nanoshell-mediated near-infrared thermal therapy of tumors under magnetic resonance guidance. *Proceedings of the National Academy of Sciences of the United States of America* 2003; 100(23):13549-13554.
- (114) Gole A, Murphy CJ. Polyelectrolyte-coated gold nanorods: Synthesis, characterization and immobilization. *Chemistry of Materials* 2005; 17(6):1325-1330.

- (115) Dreher MR, Liu WG, Michelich CR, Dewhirst MW, Yuan F, Chilkoti A. Tumor vascular permeability, accumulation, and penetration of macromolecular drug carriers. *Journal of the National Cancer Institute* 2006; 98(5):335-344.
- (116) Levick JR, Smaje LH. An Analysis of the Permeability of A Fenestra. *Microvascular Research* 1987; 33(2):233-256.
- (117) Davis SS, Illum L. Polymeric Microspheres As Drug Carriers. *Biomaterials* 1988; 9(1):111-115.
- (118) Storm G, Belliot SO, Daemen T, Lasic DD. Surface Modification of Nanoparticles to Oppose Uptake by the Mononuclear Phagocyte System. *Advanced Drug Delivery Reviews* 1995; 17(1):31-48.
- (119) Liu YL, Shipton MK, Ryan J, Kaufman ED, Franzen S, Feldheim DL. Synthesis, stability, and cellular internalization of gold nanoparticles containing mixed peptide-poly(ethylene glycol) monolayers. *Analytical Chemistry* 2007; 79(6):2221-2229.
- (120) Gittins DI, Caruso F. Tailoring the polyelectrolyte coating of metal nanoparticles. *Journal of Physical Chemistry B* 2001; 105(29):6846-6852.
- (121) Mayya KS, Schoeler B, Caruso F. Preparation and organization of nanoscale polyelectrolyte-coated gold nanoparticles. *Advanced Functional Materials* 2003; 13(3):183-188.
- (122) El Sayed IH, Huang X, El Sayed MA. Surface plasmon resonance scattering and absorption of anti-EGFR antibody conjugated gold nanoparticles in cancer diagnostics: applications in oral cancer. *Nano Letters* 2005; 5(5):829-834.
- (123) Rouhana LL, Jaber JA, Schlenoff JB. Aggregation-resistant water-soluble gold nanoparticles. *Langmuir* 2007; 23(26):12799-12801.
- (124) Zamboni WC. Concept and clinical evaluation of carrier-mediated anticancer agents. *Oncologist* 2008; 13(3):248-260.
- (125) Paciotti GF, Myer L, Weinreich D, Goia D, Pavel N, McLaughlin RE et al. Colloidal gold: A novel nanoparticle vector for tumor directed drug delivery. *Drug Delivery* 2004; 11(3):169-183.
- (126) Yu C, Irudayaraj J. Quantitative evaluation of sensitivity and selectivity of multiplex nanoSPR biosensor assays. *Biophysical Journal* 2007; 93(10):3684-3692.

- (127) Kulin S, Kishore R, Hubbard JB, Helmerson K. Real-time measurement of spontaneous antigen-antibody dissociation. *Biophysical Journal* 2002; 83(4):1965-1973.
- (128) Le XF, Arachchige-Don AS, Mao W, Horne MC, Bast RC, Jr. Roles of human epidermal growth factor receptor 2, c-jun NH2-terminal kinase, phosphoinositide 3-kinase, and p70 S6 kinase pathways in regulation of cyclin G2 expression in human breast cancer cells. *Molecular Cancer Therapy* 2007; 6(11):2843-2857.
- (129) Rasband W. Cell Counter Plugins, Image J software. National Institute of Health 2008; <http://rsb.info.nih.gov/ij/> (version 1.40, December 2008).
- (130) Gokce G, Citil M, Gunes V, Atalan G. Effect of time delay and storage temperature on blood gas and acid-base values of bovine venous blood. *Research in Veterinary Science* 2004; 76(2):121-127.
- (131) Fura A, Harper TW, Zhang H, Fung L, Shyu WC. Shift in pH of biological fluids during storage and processing: effect on bioanalysis. *Journal of Pharmaceutical and Biomedical Analysis* 2003; 32(3):513-522.
- (132) ANSI. Safe use of Lasers, no. Z136.1. New York, NY, USA: American National Standards Institute, 1993.
- (133) de Castro G, Puglisi F, de Azambuja E, El Saghir NS, Awada A. Angiogenesis and cancer: A cross-talk between basic science and clinical trials (the "do ut des" paradigm). *Critical Reviews in Oncology Hematology* 2006; 59(1):40-50.
- (134) Manohar S, Kharine A, van Hespem JCG, Steenbergen W, van Leeuwen TG. The Twente Photoacoustic Mammoscope: system overview and performance. *Physics in Medicine and Biology* 2005; 50(11):2543-2557.
- (135) Pardoe H, Chua-anusorn W, St Pierre TG, Dobson J. Detection limits for ferrimagnetic particle concentrations using magnetic resonance imaging based proton transverse relaxation rate measurements. *Physics in Medicine and Biology* 2003; 48(6):N89-N95.
- (136) Oraevsky AA. Chapter 30: Gold and silver nanoparticles as contrast agents for optoacoustic imaging. In: Wang L, editor. *Photoacoustic imaging and spectroscopy*. New York: Taylor and Francis Group, 2008: In Press.
- (137) Ermilov SA, Khamapirad T, Ghariieb RR, Conjustea A, Leonard MH, Lacewell R et al. Laser Optoacoustic Imaging System for Detection of Breast Cancer: Technical Parameters and Clinical Feasibility. *Journal of Biomedical Optics* 2008; 9(4):in the press.

VITA

Mohammad Eghtedari and his twin sister were born and raised in Shiraz, Iran. Early in childhood, making electronic circuits became his major hobby. Mohammad attended one of the top high schools in his town and then was accepted at Shiraz University of Medical Sciences to obtain his M.D. degree. By the time he graduated from medical school in 1997, he knew that he wanted to do multidisciplinary research in biomedical sciences for the rest of his life. This brought him to UTMB in 2002 to start a PhD in biomedical sciences under the supervision of Prof. M. Motamedi. It was in Galveston where he met and got married to Seamae who was a UTMB Pediatrics resident at that time. Mohammad is now the father of two lovely kids: Hannah and Ryan. To strengthen his academic profile, Mohammad passed his USMLE exams while in attendance at UTMB. Then, he applied and got accepted at the University of California in San Diego (UCSD) to start a five-year research track radiology residency. This specific residency program is for those who want to become an academic radiologist to lead research in Radiology. At the present, Mohammad is in San Diego and is working on his research at UCSD on acousto-optic imaging of fluorescently labeled targets.

Education

M.D., 9/1990 - 11/1997, Shiraz University of Medical Science, Shiraz, Iran
Ph.D. Candidate, 5/2002 to present, In progress, University of Texas Medical Branch,
Galveston, Texas
Internship, 7/2007-6/2008, The Methodist Hospital, Department of Surgery, Houston,
Texas
Residency, 7/2008 to present, University of California, San Diego, Department of
Radiology, San Diego, CA

Publications

- **Eghedari M**, Liopo AV, Copland JA, Oraevsky AA, Motamedi M, Nano Letter, Engineering of hetero-functional gold nanorods for the in-vivo molecular targeting of breast cancer cells, 2008, in press
- **Eghedari M**, Oraevsky A, Copland JA, Kotov NA, Conjusteau A, Motamedi M., Nano Letter, High sensitivity of in vivo detection of gold nanorods using a laser optoacoustic imaging system 2007, Volume: 7(7), Pages: 1914-8.
- Liu Y, Wang S, Krouse J, Kotov NA, **Eghedari M**, Vargas G, Motamedi M. , Journal of Biomedical Materials Research , Rapid Aqueous Photo-polymerization Route to Polymer and Polymer-composite Hydrogel 3D Inverted Colloidal Crystal Scaffolds 2007, Volume: 83(1), Pages: 1-9
- Y. Zhang , S. Wang , **M. Eghedari** , M. Motamedi , N. A. Kotov , Advanced Functional Materials , Inverted-Colloidal-Crystal Hydrogel Matrices as Three-Dimensional Cell Scaffolds 4/2005 , Volume: 15(5) , Pages: 725 – 731
- Copland JA, **Eghedari M**, Popov VL, Kotov N, Mamedova N, Motamedi M, Oraevsky AA , Molecular Imaging and Biology , Bioconjugated Gold Nanoparticles as a Molecular Based Contrast Agent: Implications for Imaging of Deep Tumors Using Optoacoustic Tomography 9/2004 , Volume: 6(5) , Pages: 341-9
- Kotov NA, Liu Y, Wang S, Cumming C, **Eghedari M**, Vargas G, Motamedi M, Nichols J, Cortiella J. , Langmuir , Inverted Colloidal Crystals as Three-Dimensional Cell Scaffolds 9/2004 , Volume: 20(19) , Pages: 7887-92

Abstracts

Conjusteau A, Ermilov SA, Lapotko D, Liao H, Hafner J, **Eghedari M**, Motamedi M, Kotov N, Oraevsky AA , Proc SPIE , Metallic Nanoparticles as Optoacoustic Contrast Agents for Medical Imaging 2/2006 , Volume: 6086

Eghedari M, Copland JA, Kotov NA, Popov VL, Oraevsky AA , Optical Diagnostic Imaging from Bench to Bedside. NIH, Bethesda, MD , Development of a Nanoparticle-Based Contrast Agent for Optoacoustic Tomography of Breast Cancer

9/2004 , Volume: Poster Presentation

Eghedari M, Motamedi M, Popov V, Kotov N, Oraevsky AA , Proc SPIE 2004 ,
Optoacoustic Imaging of Gold Nanoparticles Targeted to Breast Cancer Cells 7/2004 ,
Volume: 5320 , Pages: 21-28

Eghedari M, Copland JA, Kotov NA, Popov VL, Oraevsky AA, Motamedi M ,
American Society for Laser Medicine and Surgery, Dallas, TX , Optoacoustic Imaging
of Nanoparticle-Labeled Breast Cancer Cells; a Molecular-Based Approach for the
Imaging of Deep Tumors 3/2004 , Volume: Oral Presentation

Eghedari M, Copland JA, Motamedi M, Popov V, Kotov NA, and Oraevsky AA ,
SPIE Photonic West, Biomedical Optics Symposium 2004, San Jose, CA ,
Optoacoustic Imaging of Gold Nanoparticles Targeted to Breast Cancer Cells 1/2004 ,
Volume: Oral Presentation

Eghedari M, Copland JA, Popov VL, Kotov NA, Motamedi M, Oraevsky AA , Proc
SPIE , Bioconjugated Gold Nanoparticles as a Contrast Agent for Detection of Small
Tumors 7/2003 , Volume: 4960

Eghedari M, Copland JA, Motamedi M, Popov V, Kotov NA, and Oraevsky AA ,
Houston Society for Engineering in Medicine and Biology, Houston, TX , Targeted
Delivery of Herceptin-Conjugated Gold Nanoparticles to Human Cancer Cells:
Implication for Development of Contrast Agent for Optoacoustic Imaging 4/2003 ,
Volume: Oral Presentation